Fermi National Accelerator Laboratory

TM-1641

The Design of a Large Aperture High Field Dipole

Fady Harfoush, Mike Harrison, Jim Kerby, Karl Koepke, Paul Mantsch, Tom Nicol, Alan Riddiford, and Jay Theilacker
Fermi National Accelerator Laboratory
P.O. Box 500
Batavia, Illinois 60510

December 1989

Operated by Universities Research Association Inc. under contract with the United States Department of Energy

Fermi National Accelerator Laboratory

THE DESIGN OF A LARGE APERTURE HIGH FIELD DIPOLE

by

Fady Harfoush, Mike Harrison, Jim Kerby
Karl Koepke, Paul Mantsch, Tom Nicol
Alan Riddiford and Jay Theilacker

Batavia, ILLINOIS

December, 1989

Contents

1 Introduction 1

2 Magnetic Properties 9
- 2.1 Cable Characteristics 9
  - 2.1.1 Expected Performance 12
- 2.2 Coil Cross-section 14
  - 2.2.1 Introduction 14
  - 2.2.2 Optimization Procedure Using Wedges 15
  - 2.2.3 Offset Coils and dB/B profiles 16
  - 2.2.4 Forces on each conductor; tangential cumulative forces 19
  - 2.2.5 Operating margin and performance of various designs . 20
- 2.3 Coil Placement Errors 24
- 2.4 Time Varying Field Effects 32
  - 2.4.1 Cyclic Heat Load 33
  - 2.4.2 Eddy Current Forces 41
- 2.5 Quench Protection 42
  - 2.5.1 Quench Protection System 42
  - 2.5.2 Cable Quench Temperature 44
  - 2.5.3 Heater Considerations 45
- 2.6 Yoke Design 52
  - 2.6.1 Iron Effects 52
  - 2.6.2 Saturation Effects 58
  - 2.6.3 The Sextupole due to Saturation 59
  - 2.6.4 Effects of Inner and Outer Diameters 63
  - 2.6.5 Elliptical Cross-Sections 70
  - 2.6.6 Effect of Iron Ellipticity on Conductor Placement . . . 73
  - 2.6.7 Effects of Keys and Holes 73

2.6.8 Centered or Offset Coils 74
2.6.9 Suggested Design 74

3 Mechanical Properties **80**
3.1 Beam Tube Design 80
3.1.1 Thermal Considerations 81
3.1.2 Structural Considerations 86
3.2 Collar Design 88
3.2.1 Effect of Collar Width 88
3.2.2 Keying Mechanisms 89
3.3 Yoke Design 91
3.4 Cold Mass Suspension System 108
3.4.1 Introduction 108
3.4.2 Support Post Design and Analysis 109
3.4.3 Structural Analysis 109
3.4.4 Anchor System 118
3.5 Cryostat Design 119

4 Cryogenic Properties **131**
4.1 Tevatron Cryogenic System 131
4.2 Fixed Target Operation 133
4.3 Collider Operation 137

References **149**

List of Tables

2.1 Conductor Specification 12
2.2 Operating Margins 12
2.3 Field error for the design D743 vs. offset. Reference radius=0.917" or 2/3 rds of the aperture 17
2.4 Horizontal field errors and harmonic coefficients for D743 . . . 18
2.5 Design parameters for 2.75" aperture dipoles. Conductor # 2 at 4.2 K. 6/27/89 21
2.6 Study of the effect of the offset. Ref. radius = 1". Poles equal and higher to 34 are in 10^{-7} units. 22
2.7 Study of the variation of field over conductors 24
2.8 Tevatron Dipole Field Coefficients. Average of 870 magnets at 4000A. Coefficient units 10^{-4} at 1.0 in 32
2.9 Energy Loss Per Cycle For R-Series Test Magnets. Test Conditions: 32 in. magnet length, no iron, therefore 8.0 G/A ,all data with 4000 A peak cycle 40
2.10 Cyclic Energy Loss Summary 40
2.11 Dipole magnet parameters 79
2.12 Iron yoke dimensions 79

3.1 Thermal Design Considerations 82
3.2 Tevatron-style Energy Balance results 83
3.3 New Flow Loop Energy Balance Results (Stainless Steel) . . . 84
3.4 New Flow Loop Energy Balance Results (Stainless Steel with 0.003" Kapton) 85
3.5 Beam Tube Assembly Cross Section Flow Areas 87
3.6 SSC Dipole Structural and Thermal Load Summary 109
3.7 Comparison of Two Structurally Optimized Support Posts . . 118
3.8 Summary of Structural Analysis Results 126

3.9 Summary of Shrink Fit Analysis 129

4.1 Tevatron Refrigeration System Capacities 131
4.2 1.8K Collider Heat Loads and Capacities 134

List of Figures

1.1 High Field Dipole Magnets Schematic Cross Section 8

2.1 Expected cable characteristics 13
2.2 Cross section of one quadrant of a dipole 25
2.3 D743 conductor placement 26
2.4 Comparing the saver dipole and the proposed offset dipole D721 27
2.5 D743 forces on each conductor 28
2.6 Azimuthal Conductor Motion 31
2.7 Steel B(H) Curve 35
2.8 Energy loss/cycle vs excitation current 37
2.9 Energy loss/cycle vs ramp rate 38
2.10 Cable temperature vs cable Miits 46
2.11 Conductor placement for the proposed offset dipole D743 . . . 48
2.12 Heater induced magnet current decay 50
2.13 Heater induced quench Miits 51
2.14 Heater induced current decay 53
2.15 Heater induced inductive voltage 54
2.16 Heater induced quench Miits 55
2.17 Current element within a circular iron boundary 57
2.18 Equivalence of a Saturated Iron and a Surface Coil 61
2.19 Field lines in a dipole magnet 62
2.20 Sextupole variations for different inner radii of the yoke at two different excitations, J=4.44kA/turn and J=6.10kA/turn. Here, $R_{coil}^{inner} = 1.5''$, $R_{coil}^{outer} = 2.3''$, $R_{iron}^{outer} = 8.66''$, Inner turns/Outer turns = 39/33 64
2.21 Change in sextupole vs dipole field at three different inner radii 65
2.22 Amplification factor for different inner radius of the yoke . . . 66

2.23 Sextupole change vs iron outer radius at two different excitations, J=4.36kA/turn and J=5.76kA/turn. Here, $R_{iron}^{inner} = 3.54"$ 67
2.24 Amplification factor for different outer radii of the iron 68
2.25 Fringe fields versus iron outer radius 69
2.26 Effects of an inner flat top pole of height H on sextupole. Here, $R_{iron}^{inner} = 4$ in and $R_{iron}^{outer} = 8.66$ in 71
2.27 Effects of an outer flat top pole on sextupole. Here, $R_{iron}^{inner} = 3.789"$, $R_{iron}^{outer} = 9.055$in, outer H = 6.505 in 72
2.28 Effects of keyed inserts on sextupole at two different locations. Here, $R_{iron}^{inner} = 4$ in, $R_{iron}^{outer} = 8.66$ in 75
2.29 Effect of an offset coil on sextupole. Here, $R_{coil}^{inner} = 3.5in$, $R_{coil}^{outer} = 6in$, $R_{iron}^{inner} = 3.789in$, $R_{iron}^{outer} = 9.05$in, and offset=-0.414 in . . 76
2.30 Yoke laminations 77
2.31 Sextupole change for a) the suggested elliptical yoke design b) similar design but with circular iron and c) the final elliptical design with a flat cut top pole 78

3.1 Beam Tube Design 91
3.2 Four magnet group 92
3.3 Helium Coil Flow Temperature Rise 93
3.4 Beam tube Assembly 94
3.5 Single Phase and Two Phase Flows 95
3.6 Coil Helium Flow Temperature Rise 96
3.7 Coil Helium Flow Temperature Rise 97
3.8 Beam Tube / Two Phase Passage 98
3.9 High field Dipole 99
3.10 Aluminium Hoop Collar Model 100
3.11 Collar deflection 101
3.12 Dipole Collars 102
3.13 Front Collars 103
3.14 Back Collars 104
3.15 Stress Plot W/2.25 Keys 105
3.16 Stress Plot W/4 Keys 106
3.17 Suspension System Components 122
3.18 Support Post Cross Section 123
3.19 Structural Load and Direction Notation 124
3.20 Structural Analysis Notation 125

3.21 Thermal Analysis Notation 127
3.22 Shrink Fit Joint Notation 128
3.23 Phase III Dipole cross Section 130

4.1 Tevatron Satellite Refrigerator with Cold Compressor 142
4.2 Satellite Performance 3.5 - 4.5K 143
4.3 Satellite Performance 1.5 - 3.5K 144
4.4 Fixed Target Mode Flow Schematic 145
4.5 Two-Phase Passage Configuration 146
4.6 Collider Mode Flow Schematic 147
4.7 Satellite Refrigerator Configuration for 1.8K Accelerator Option 148

Chapter 1

Introduction

The impetus for this design report originated in the Snowmass 88 meeting where the subject of higher energies within the constraints of the existing Tevatron tunnel enclosure was investigated. It was determined that beam transport to the fixed target experimental areas was possible up to an energy of $\sim$ 1.5 Tev. Collider operation was feasible at somewhat higher energies (1.8 Tev), primarily limited by the ability to design a single turn beam abort system within the constraints of the straight section length. A new accelerator in the existing tunnel would, of necessity, have a similar though not identical lattice and straight section layout to the present Tevatron. Thus when issues arose in the magnet design requiring input from the accelerator standpoint we have assumed a Tevatron like machine. The possibility of using these high field magnets as elements in the existing Tevatron to create new 'warm space', for another Interaction Region for example, also emphasizes compatibility with the present machine.

The goal of the high field magnet design program is therefore to produce a superconducting magnet consistent with these overall goals; i.e. capable of supporting fixed target operation (ramping, resonant extraction) at a field of 6.6T, and colliding beam physics at 8.0T corresponding to energies of 1.5 Tev and 1.8 Tev respectively. We have chosen to concentrate on a magnet design which could be built immediately and thus have not considered superconducting materials beyond the standard Nb-Ti used in existing magnets (Tevatron, HERA, SSC). This in turn implies that in order to achieve peak fields of the level required (8.0T), the magnet temperature must be maintained at $\sim 2.0^o$ K; the 6.6T operation will take place at 4.2^o K. The ac heat load on the cryogenic system, due to hysteretic losses in the superconductor and the iron associated with the continuous ramping of fixed target operation precludes the lower temperature in this mode.

In a similar manner to the existing Tevatron, the most stringent requirements on magnetic field quality at high fields come from the the large amplitude orbits associated with resonant extraction. In this process the beam must be able to sustain particle amplitudes out to 25- 27mm for half the circumference of the machine without any significant phase space distortion due to higher order field harmonics in the magnets. The beam must be able to circulate for many turns at amplitudes of $\sim$ 20mm. In view of the essential similarity of the beam dynamics with the existing Tevatron, the design criteria for the magnetic field quality has been chosen to be as least

as good as that given by the measured magnetic multipoles of the existing Tevatron magnets. The magnetic field quality at low excitation is defined by the large amplitude orbits associated with the proposed beam separation scheme for collider operation. In order to avoid the luminosity limitation arising from the beam-beam interaction, electrostatic deflectors are used to create non-intersecting closed orbits for the protons and antiprotons at the injection energy. The amplitude of these helical orbits ($\pm$7.5mm) together with the relatively large beam size at the low energy require a 'good field' region of ;$\pm$20mm to permit adequate beam separation ($> 5\sigma$). The low field behavior of the magnets is complicated by the persistent current phenomena that produce systematic sextupole and decapole harmonics. It has been demonstrated in accelerator studies that the present Tevatron dipoles can sustain these large amplitude orbits, so again the existing machine provides guidance as to the necessary field quality. The orbit separation at collision energies ($\pm$5mm) provides less demanding field quality criteria than resonant extraction.

The design of a superconducting magnet originates with the characteristics of the superconducting cable. There are three important variables: temperature(T), magnetic field(B), and current density (J). For temperatures lower than the critical temperature, there is a region of current density and magnetic field for which the superconductor exhibits zero resistance. The problem in magnet design is to ensure than no point in the magnet coil

has combinations of J,B, and T that lie outside of the superconducting region. Other major design issues involve the coil geometry to provide the field shape, the size and shape of the iron yoke, containment of the mechanical stresses resulting from the Lorentz forces on the coils, the cold mass assembly and supports, and the incorporation of suitable cryogenic properties into the magnet

The overall magnet design adopted is a cold iron approach similar to the HERA/SSC magnets although the higher peak fields and large bore size have resulted in more attention being given to the problems of coil forces and yoke saturation. Low temperature operation within the enviroment of a cold iron mass have resulted in significant changes to the cryogenic design. The cable design chosen for this magnet development is a hybrid of the two types of superconductor used at Fermilab: the Tevatron cable with a strand diameter of 0.681mm, and the low β quadrupole cable with 36 strands. The copper to superconductor ratio is chosen to be 1.5:1 to facilitate quench protection. The magnet design is estimated to have a $\sim$ 10% operating margin. The choice of filament size in the cable is important in minimizing the persistent currents with their time dependance. Assuming full field penetration of the superconductor, the inherent magnetisation at low excitation varies linearly with the filament diameter. The existing Tevatron magnets use a 9μ filament that results in a sextupole harmonic of 4 units at injection energy, or 120 units of chromaticity. A filament diameter of 6μ has been specified

for the new cable. This will reduce the systematic sextupole at low field from the Tevatron levels, but would not remove the effect from operational significance.

Two recent developments in coil design techniques, wedges and offset placements, permit the construction of coils that generate better field quality than that achieved in the Tevatron magnets. Conversely, smaller diameter coils can be used to generate the same field quality. Both of these techniques modify the current distribution in the cosine- theta style coils to more closely resemble the perfect current density distribution. The ability to design the perfect coil is limited by the cable size that introduces 'granularity' into the process. The proposed coil cross-section utilizes both of these features and results in a coil diameter of 69mm that produces a significantly larger good field region than the Tevatron coil which uses a 76mm diameter. Horizontally bending accelerators result in dispersive effects in the lattice which tend to emphasize aperture requirements in the horizontal plane over the vertical one. Resonant extraction in the horizontal plane also places more stringent demands on field quality in this direction. Consequently we have chosen a coil geometry which maximizes the horizontal aperture over the vertical one by a ratio of 1.2.

The geometry of the iron yoke is determined by the saturation effects of the iron for fields in excess of 6T. The closer the iron yoke is to the collared coil assembly, the larger the enhancement of the dipole field and

the magnet is more efficient. However, if the yoke is too close to the coils, then the saturation effects become significant, resulting in a large systematic sextupole moment. A minimum collar thickness is necessary to support the large preload forces during the collaring process which also limits the distance between the coil and the yoke. Lateral support members, cryogenic penetrations, and collar key inserts are needed in the yoke which also influence the field shape.

The collar design is dominated by the very large preload (20Kpsi) needed to stabilise the coil against the motion caused by the Lorentz forces at the highest fields levels, which are estimated at 16Kpsi at an excitation of 9T. Aluminum collars are needed to maintain this preload during cooldown, but stresses approaching the yield point of the material can only be avoided by multiple wedges.

Minimizing the 2°K helium inventory, hence cooldown time and refrigeration power, results in a $1\phi - 2\phi$ heat exchanging scheme incorporated into the beam tube assembly. A total of 6 cryogenic circuits are needed for both modes of operation. The cryostat design is based on the SSC development with some mechanical modifications. The outer magnet shell is made of magnetic steel to minimize flux leakage from the body of the magnet.

A schematic cross-section is given in Fig. 1.1. The rest of this report provides details of this design together with the considerations resulting in this approach.

Issues not considered in any depth in this report are the magnet interface regions, tooling considerations, and the details of the coil geometry and mechanical properties at the magnet ends. This latter aspect of a magnet design generally relies on an iterative approach at the prototyping stage to achieve the final layout. We have also made no special attempts to deal with the problems of the time dependant change in the lower order systematic multipoles at low fields arising from the slow decay of the persistent currents, other than suggesting the use of the smallest filament diameters possible. Passive correction schemes (shorted turns), and bore tube correction windings have been suggested for the SSC magnets as methods of applying local corrections to the field harmonics. The Tevatron lattice however, is much less sensitive to these effects than the SSC and we have tacitly assumed a lumped correction scheme similar to the existing system as a guideline to tolerable systematic multipoles.

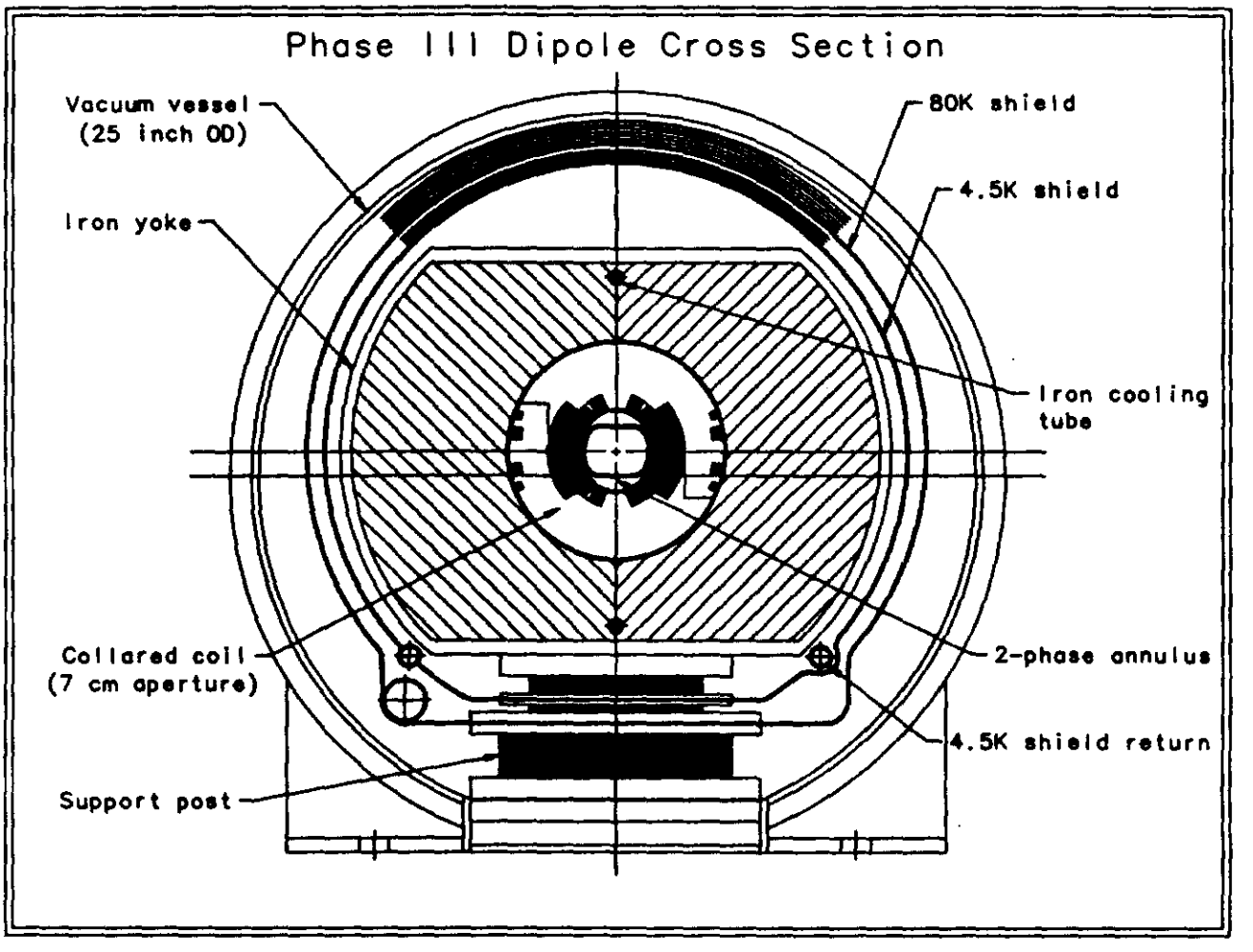

Figure 1.1: High Field Dipole Magnets Schematic Cross Section

Chapter 2

Magnetic Properties

2.1 Cable Characteristics

The performance of the magnet depends on the coil/iron geometry and the current. In the cosine theta dipole using Rutherford-type cable the dimension specification of the cable is, therefore, a key feature of the magnet design. The critical current density in the conductor will determine the maximum field. Other design considerations include optimization of mechanical and cryogenic stability, insulation integrity, power supply restrictions and cost of materials.

The primary objective in selecting the conductor for this magnet was to insure that the magnet have a performance margin of about ten percent over the nominal operating current. The geometrical and current specification for the proposed cable are shown in Table 2.1.

High fields in accelerator magnets require high-current density. Motivated largely by the needs of the SSC, the advance in current density in NbTi con-

ductor has been dramatic in the past few years. While superconductor current densities in Tevatron cables were near 1800 A/mm^2(4.2 K, 5 T), recent advances have resulted in current densities that now approach 3000 A/mm^2. Recent experience with the Fermilab low β quadrupole program suggests that 2800 A/mm^2 is a reasonable specification for cable current density in production quantity. Based on the HERA experience, expected variation in cable performance in production is about 2%. A copper-to-superconductor ratio of 1.5 to 1 was selected to maximize the overall current density without compromising coil stability. Studies presently underway with the SSC magnet R&D program may conclude that a copper-to-superconductor ratio of 1.3 does not degrade stability. Should that be the case the conductor, richer in superconductor, can be considered to increase the operating margin.

A filament size of 6 microns was chosen. This selection reflects the smallest filament diameter that can now be confidently obtained in wire made in industry. Although the SSC magnet development program includes an effort to produce conductor with 2.5 micron filaments, production quantities of this wire have not yet been produced.

The coil requires a substantial quantity of superconductor. To minimize the current per turn but yet have adequate width, a cable with a large number of strands, i.e., high aspect ratio, was selected. The strand diameter was chosen to give the necessary cable width. A 36 strand cable of Tevatron size strands (0.0268 inches) gives a coil of sufficient size to produce an adequate

aperture margin. There is now considerable experience with 36 strand cables. Cables with 36 strands of 0.0208 inches are being made for the Tevatron Low β Quadrupole program. Taylor's group at LBL has also successfully made cables with 36 strands of 0.0255 inch diameter.

The dimensions of the cable were selected so that a stable geometry could be produced with no cabling damage to the conductor at the narrow end. The compaction of this cable is similar to that in the Tevatron and the SSC. The higher compaction of the cable used in the low β quadrupole appears to result in unusually high degradation from cabling.

The ultimate performance of such a coil is determined by the current density and by the ability of the coil to withstand the high forces to which it is subjected in order to be mechanically stable under power. The integrity of the insulation under high pressure becomes crucial. The pressure in this magnet at 6.6 T is 25% higher than in the Tevatron at 4.4 T and 2.4 times the Tevatron at 8.8 T (17 kpsi). These are higher pressures than any previous cosine theta magnet has sustained in fabrication and operation. The insulation based on the traditional Tevatron system will be: a Kapton wrap followed by a barber pole wrap of epoxy impregnated glass tape. A development program is underway to determine the details of an insulation system that will meet the difficult pressure requirements and will also be resistant to creep.

Strand diameter (inches)	0.0268 +0.0002 -0.0000
Number of strands	36
Copper to superconductor ratio	1.5:1
Strand twist pitch (twists per inch)	2
Filament diameter (microns)	6
Filament spacing/diameter	< 0.2
Number of filaments	~ 5000
Critical current density (A/mm^2 at 4.2 K, 5 T)	≥ 2800
Cable keystone (degrees)	1.03
Cable thickness, inner edge (inches)	0.0439
Cable thickness, outer edge (inches)	0.0525

Table 2.1: Conductor Specification

Operating Temperature	Design Operating Field	Field at Critical Current	Operating Margin
4.2 K	6.6 T	7.18 T	9%
1.8 K	8.8 T	9.90 T	12%

Table 2.2: Operating Margins

2.1.1 Expected Performance

The magnet load line along with the expected characteristics of the cable are shown in Figure 2.1. The central fields at critical current and the corresponding operating margins are shown in Table 2.2.

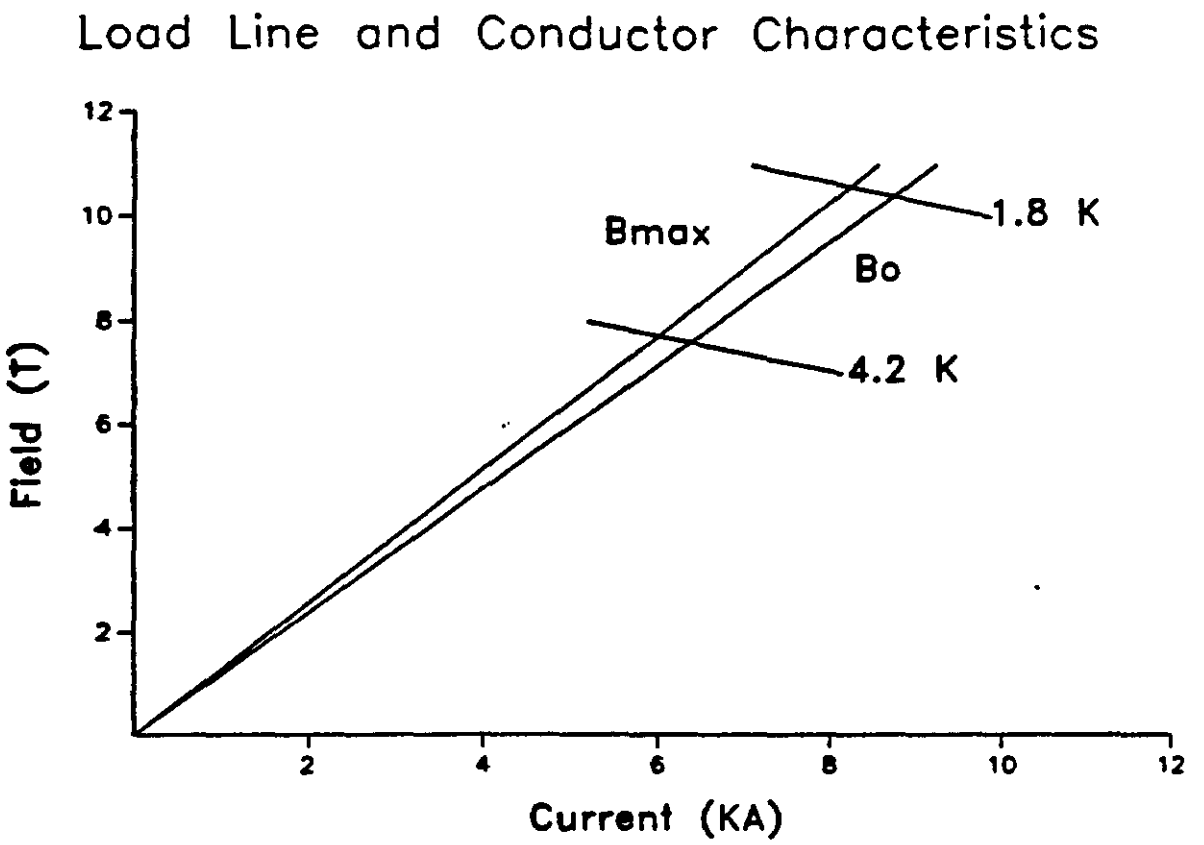

Figure 2.1: Expected cable characteristics

2.2 Coil Cross-section

2.2.1 Introduction

The Tevatron dipole was designed without using wedges. The conductors were assumed to be flexible enough to take on the keystone angle needed to make the long faces of each conductor lie on lines going through the axis of symmetry of the beam tube.

Two changes have been made in more recent designs. The keystone angle has been made smaller so as not to crush the strands so much at the inner edges of the conductors. That meant that as conductors were being stacked up against a circular mandrel, the long faces became more and more non-radial. So wedges were introduced to reduce the non-radial angles.

The harmonic coefficients can also be improved by the wedges if they are properly positioned. The following sections discuss how the wedges were positioned to optimize the harmonic coefficients and the non-radial angles. The other change since the Saver is the introduction of offset coil designs. It was discovered that for some groupings of conductors, introducing an offset (r_o in Figure 2.2) improves the profile of the field error dB/B. The idea has been studied by T. Collins [1], and more recently by Ishibashi [5]. They studied the simplified problem of one constant current density area per group of conductors (neglecting the insulation wrapped around each of the conductors).

A computer code has been written to check POISSON results and to reproduce results published by Collins. A separate report [13] is being written

to show the derivation of the code and to show several tables listing the results of changing the magnitude of the offset.

2.2.2 Optimization Procedure Using Wedges

Figure 2.2 shows a typical cross-section of one quadrant of a dipole. The other three quadrants are made to be symmetric across the x-axis and/or y-axis. Given an offset r_o and a semi-aperture "a", the mandrel upon which conductors are stacked is defined. A wedge is not needed in the outer layer for the coil inner diameter given. The keystone angle is large enough to keep the conductors roughly radial. However, the inner layer of conductors needs at least one wedge to keep conductors roughly radial. It has been found that two wedges permit solutions with smaller harmonic coefficients. Furthermore, each of the wedges allows a solution to be found which zeros out one of the coefficients. So the method discussed here uses two wedges and zeros out the sextupole and decapole harmonic coefficients. More wedges provide more degrees of freedom to reduce the coefficients further.

Pick a set of numbers for the conductors per group. Then pick Y values (Y_A & Y_B) for the lowest points of the conductors just above each of the two wedges large enough to avoid knife edges at the thin edge of each wedge (say .015").

Then the data is read by a program which iterates the two angles θ_A and θ_B until the sextupole and decapole harmonic coefficients vanish. Angle θ_A is changed (using Newton's method) until the sextupole coefficient vanishes.

Next θ_B is changed and θ_A optimized again. Newton's method is used to calculate the next value of θ_B each cycle. The code prints out a table listing the contribution of each conductor to each of the first five allowed harmonics. The table is useful when trying to decide how many conductors to place in each group.

Figure 2.3 shows the conductor placement for the most recent design D743. The iron has been assumed to have an infinite permeability μ, and to have a circular inner surface.

2.2.3 Offset Coils and dB/B profiles

Table 2.3 shows the effect of varying the offset. The offset is another degree of freedom (like a wedge) which can be used to reduce field errors. The method used here calculated the field error (from a uniform dipole $B_x = 0$, $B_y =$ constant) on a circle whose diameter is two thirds of the aperture of the coil. The field error was calculated at each degree from zero to 90 degrees. The maximum value has been listed on the table. Solutions for offsets near zero do not exist for the set of numbers of conductors per group shown in the table. The computer code finds the field by calculating the line integral around each of the 66 conductors, so this table gives more realistic results than the similar tables reported in [13] where insulation was neglected within each group.

As the offset is increased, the field error at (.917",.000") increases but the maximum error (at any angle) reaches a minimum around the offset of

Offset (cm)	dB/B (0 deg) 10E-4 Units	(dB/B)max 10E-4 Units	at (deg)
0.4000	0.120	1.784	90
0.4100	0.530	1.610	90
0.4140	0.692	1.596	81
0.4144	0.708	1.599	80
0.4150	0.732	1.606	79
0.4200	0.933	1.719	69
0.4300	1.338	2.075	65

Table 2.3: Field error for the design D743 vs. offset. Reference radius=0.917" or 2/3 rds of the aperture

0.4140 cm. The offset 0.4144 cm makes the field error along the x-axis peak at one unit near 1.05". D743 (using an offset of .4144 cm) happens to achieve nearly the best field error for all angles at the same time as maximizing the "good field" region on the x-axis. D743 keeps the field error below one unit out to 1.18" or 85 % of the aperture. This horizontal good field region is relevant to an accelerator where horizontal resonant extraction is needed.

Figure 2.4 compares the field error profile of D721 with the Saver dipole profiles as published in the design report. The profile for D743 (inner iron radius = 3.789") is very close to the D721 profile (inner iron radius = 4") and is therefore not shown in Fig. 2.4. The D743 profile peaks a little to the right of D721 and is slightly higher than D721 further to the right, so the D743 profile is slightly better than that of D721.

Table 2.4 shows the harmonic coefficients and the field error on the x-axis.

1 0.0 Tools D743 (-SNOW2E) 06/12/09 09:20:35

NSEGS = 06 SEGMENTS; DIPOLE SYMMETRY

RIRON =	0.0240	CM	
RIRON =	3.7900	INCHES	
RREF =	2.6400	CM	
RREF =	1.0000	INCHES	
ROFF =	0.4144	CM	
ROFF =	0.1631	INCHES	
CURRENT =	5.0000	KAMPS/TURN	
SEGMENT AREA =	0.0214	SQINS	
CDENSE =	273.0084	KAMPS/SQIN	
FACTOR =	10.7020	KGAUSS*INCH	
SEGMENT AREA =	0.0214	SQINS	
CDENSE =	273.0084	KAMPS/SQIN	
FACTOR =	10.7020	KGAUSS*RREF	

POLE	BOTH	AIR	IRON	RATIO
1	00.302004100	03.290152300	13.003511777	10000.000
3	0.000000011	-0.034032146	0.034032157	0.000
5	-0.000000001	0.000710032	-0.000710033	0.000
7	0.002701010	0.002770000	-0.000014200	0.416
9	0.010707090	0.010700050	0.000000237	1.022
11	0.004444101	0.004444155	0.000000000	0.700
13	-0.014459951	-0.014459960	0.000000000	-2.179
15	0.002012924	0.002012924	0.000000000	0.424
17	-0.000154740	-0.000154740	0.000000000	-0.023
19	0.000067710	0.000067710	0.000000000	0.000
21	0.000101402	0.000101402	0.000000000	0.020
23	-0.000000209	-0.000000209	0.000000000	-0.015
25	-0.000042355	-0.000042355	0.000000000	-0.000
27	-0.000001302	-0.000001302	0.000000000	0.000
29	0.000002500	0.000002500	0.000000000	0.000
31	0.000000042	0.000000042	0.000000000	0.000
33	0.000000020	0.000000020	0.000000000	0.000
35	-0.000000099	-0.000000099	0.000000000	0.000

	RREF units	cm	BOTH	AIR	IRON	RATIO	DIFF
X =	0.000	0.000	00.302004100	03.290152300	13.003511777	10000.000	0.000
X =	0.050	0.127	00.302004166	03.290067814	13.003500052	10000.000	0.000
X =	0.100	0.254	00.302004169	03.290012143	13.003052020	10000.000	0.000
X =	0.150	0.381	00.302004200	03.290307004	13.004277196	10000.000	0.000
X =	0.200	0.500	00.302004871	03.297792450	13.004871013	10000.000	0.000
X =	0.250	0.635	00.302004009	03.297020021	13.005035070	10000.000	0.000
X =	0.300	0.762	00.302004000	03.290000002	13.004500044	10000.000	0.000
X =	0.350	0.889	00.302071740	03.296001034	13.007000015	10000.001	0.001
X =	0.400	1.016	00.302002707	03.297744000	13.000900402	10000.003	0.003
X =	0.450	1.143	00.302705020	03.292332102	13.070070720	10000.006	0.000
X =	0.500	1.270	00.302756553	03.290776036	13.071074710	10000.013	0.013
X =	0.550	1.397	00.302032007	03.290001091	13.072740400	10000.025	0.025
X =	0.600	1.524	00.302072039	03.287300000	13.075000033	10000.046	0.046
X =	0.650	1.651	00.303292404	03.286441345	13.077701119	10000.001	0.001
X =	0.700	1.778	00.303550500	03.283540113	13.000012400	10000.135	0.135
X =	0.750	1.905	00.304000303	03.281001220	13.002426156	10000.214	0.214
X =	0.800	2.032	00.304021211	03.270020000	13.004904545	10000.325	0.325
X =	0.850	2.159	00.305701727	03.270001050	13.007710000	10000.470	0.470
X =	0.900	2.286	00.300000000	03.270300000	13.000000232	10000.644	0.644
X =	0.950	2.413	00.300156505	03.274525072	13.000300012	10000.820	0.820
X =	1.000	2.540	00.309140000	03.272330155	13.000011054	10000.977	0.977
X =	1.050	2.667	00.309330170	03.290100510	13.100140000	10001.000	1.000
X =	1.100	2.794	00.307715001	03.204100400	13.103014022	10000.761	0.761
X =	1.150	2.921	00.302543337	03.265312102	13.107231155	9999.002	-0.010
X =	1.200	3.048	00.350090135	03.230002501	13.110007554	9998.220	-1.774

Table 2.4: Horizontal field errors and harmonic coefficients for D743

The iron contribution to the dipole coefficient is also shown. Note that the sextupole and decapole coefficients are made zero by bucking the iron component against the air component.

All these calculations assume the iron to be of infinite μ and to have a circular inner surface so that image currents could be used. (The iron can be easily replaced by image currents when the inner surface is circular and if the μ is infinite.)

2.2.4 Forces on each conductor; tangential cumulative forces

Figure 2.5 shows the average force on each conductor at a bore field of 6.6T. The components of the field were calculated at the midpoint of each face and then averaged. So the average position is the centroid of the conductor and the average field (when crossed into by the current) should be a good approximation to the average force on the conductor.

The forces are indicated in the figure by thin lines. The magnitude of the line coming from the centroid of the top (inner layer) conductor corresponds to a force of 212 pounds/inch. Adding up the tangential components of these forces gives 4,249 pounds/inch at the parting plane for the inner layer, and 2,091 pounds/inch at the parting plane for the outer layer. Dividing by the conductor width 0.477" gives 8,907 psi at the parting plane for the inner layer and 4,385 psi for the outer layer.

2.2.5 Operating margin and performance of various designs

Table 2.5 summarizes the performance of various designs. The first two (D627 and D628) were designed to provide 6.6 Tesla at the Saver current of 4,435 amps/turn. Cable used in the low β quad was assumed for these two samples (.0208" strand diameter). Since the operating margin was so low, a wider cable was defined for D720 (.0260" strand diameter) and refined slightly for D743 (.0268" strand diameter).

The inner iron radius (Riron) was adjusted in D627 & D628 to achieve the desired transfer function. The 4.0" Riron was chosen for D721 to improve the saturation profile of the sextupole coefficient. In D743, the Riron value was fixed by the designers of the collar.

The loadline for the first two designs was taken to be the measurement of low β quad conductor # 2 at 4.2 K degrees. For D721 & D743 five percent was added to the results of Morgan & Sampson.

Table 2.6 shows the effect of an offset for a particular two layer coil defined by radii 1.3815 cm, 1.8700 cm, 2.3585 cm and angles varied to make the sextupole and decapole harmonic coefficients zero. The current density was made 330 amps/mm^2 for the inner layer and 400 amps/mm^2 for the outer layer.

Two general trends can be seen. While the field error at zero degrees grows, the field error for all angles decreases to a minimum and then slowly

	Low β Quad cable		25 % larger cable	
	D627	D628	D721	D743
Imax, maximum current (amps)	4,506	4,503	5,952	6,347
Bmax, high field at Imax (Tesla)	7.3409	7.3430	7.7536	7.7006
B(Imax), central field (Tesla)	6.7728	6.7673	7.2188	7.1877
Bmax/B(Imax)	8.39 %	8.51 %	7.41 %	7.14 %
B(Imax)/6.666 Tesla, operating margin	1.60 %	1.52 %	8.3 %	7.8 %
I, Operating current (amps)	4,435	4,435	5,496	5,886
B(I) (Tesla) infinite mu	6.6659	6.6660	6.6660	6.6660
hline B(I) with 1 % ampfactor (Tesla)	6.6000	6.6000	6.6000	6.6000
Transfer function (Tesla/(Kamps))	1.488	1.488	1.201	1.132
Number of turns	82	85	72	66
Riron (inches)	3.510	3.676	4.000	3.789
Offset (inches)	0.059	0.168	0.157	0.163
10,000*(DB/B)max	1.136	1.202	0.987	1.006
Radius at max (DB/B)	1.10"	1.10"	1.00"	1.05"
Harmonic coefficients at 1" (10E-4 units)				
2	10,000	10,000	10,000	10,000
6	0.00	0.00	0.00	0.00
10	0.00	0.00	0.00	0.00
14	-3.72	-3.69	1.41	0.42
18	6.30	6.68	-0.48	1.62
22	0.40	-0.47	2.25	0.70
26	-2.45	-1.56	-2.50	-2.18
30	0.70	0.11	0.22	0.42
34	-0.62	-0.36	0.10	-0.02
38	0.15	0.11	-0.02	0.01
42	0.06	0.03	0.02	0.03
46	-0.02	-0.001	-0.003	-0.015
50	0.01	0.003	-0.008	-0.006

Table 2.5: Design parameters for 2.75" aperture dipoles. Conductor # 2 at 4.2 K. 6/27/89

Offset(mm)	dB/B at 0°	$(dB/B)_{max}$	at degrees	14-pole	18-	22-	26-	30-
0	0.90	28.0	90	9.10	-12.0	5.3	-1.40	0.230
1	0.75	21.5	90	5.80	-9.9	4.4	-1.20	0.240
2	2.02	16.0	90	3.10	-7.9	3.7	-1.10	0.230
3	3.02	11.5	90	0.97	-6.3	3.0	-0.88	0.210
4	3.83	7.7	90	-0.75	-5.0	2.5	-0.74	0.180
5	4.45	5.4	57	-2.10	-3.9	2.1	-0.61	0.150
6	4.94	5.5	44	-3.30	-3.0	1.7	-0.50	0.130
7	5.31	5.8	42	-4.20	-2.2	1.4	-0.41	0.110
8	5.60	6.1	42	-4.90	-1.6	1.2	-0.34	0.085

34-	38-	42-	46-	50-	54-	58-	62-
64	-87.0	51.00	-20.00	5.40	-0.007	-1.100	0.830
12	-49.0	-	-	-	-	-	-
-16	-25.0	20.00	-8.80	-	-	-	-
-29	-11.0	11.00	-6.10	2.40	-0.640	-	-
-34	-2.3	6.20	-3.70	1.60	-0.540	0.140	-
-34	2.3	3.00	-2.20	0.99	-0.370	0.110	-0.023
-31	4.4	1.10	-1.20	0.59	-0.240	0.079	-0.021
-27	5.2	0.47	-0.57	0.33	-0.140	0.052	-0.016
-23	5.2	-0.49	-0.22	0.17	-0.082	0.032	-0.011

Table 2.6: Study of the effect of the offset. Ref. radius = 1". Poles equal and higher to 34 are in 10^{-7} units.

increases (with increasing offset). The lower part of the table shows that the magnitudes of the coefficients decrease (with increasing offset). It is believed that the long timescale behavior of particles is influenced by the strength of the higher harmonic coefficients. Notice that for zero offset the signs are alternating: 64, -87, 51, -20, etc., while for an offset of 5 mm, the magnitudes are much reduced, making the field much smoother. The offset shape better approximates the perfect dipole crescent shape, where the higher harmonic coefficients are all zero.

Table 2.7 shows the variation of field over conductors. The average field is listed in (R, theta) components in the second and third columns. Conductor numbers start at 1 on the parting plane for the inner layer, go to 36 at the pole, and start the outer layer at the parting plane with 37 and finish at 66. Face 1 is the bottom; 2 right; 3 top; 4 left (toward the axis of the magnet). The field difference is listed in the next two columns. The field of the left(4) face of conductor 1 is (66.3 kGauss, 90.5 deg), the vector sum of the average field and the difference field.

The conductors listed are the extremes of difference field values as the comments indicate. The largest difference magnitude (of the four mid-faces of one conductor) is on the left face except for conductors near the pole, where the largest magnitude is on the right face. Notice on Figure 2.5 that the field (on the parting plane) crosses zero just to the left of the centroid of the outer layer. So the average field in conductor 37 is almost zero (left

Cond. #	Avg. Field	Degrees	Diff. Field	Degrees	Face	Comments
	(KGauss)		(KGauss)			
1	42.0	90.1	24.2	90.5	4	Parting plane (inner layer)
3	42.2	88.2	24.4	93.5	4	Local max
15	46.3	80.7	21.5	113.1	4	Local min
25	54.5	70.5	23.5	137.6	4	Local max
34	59.0	76.9	18.8	144.6	4	Last 4 (left face)
36	63.5	78.0	16.0	-48.7	2	Pole-most (inner layer)
37	0.9	-68.1	21.0	90.5	4	Parting plane (outer layer)
54	23.3	23.2	22.3	107.0	4	Local max
61	34.8	30.4	18.0	113.0	4	Last 4 (left face)
66	47.4	36.3	13.7	-82.3	2	Outer layer complete

Table 2.7: Study of the variation of field over conductors

mid-face 21.0 kG 90.5 deg.; right mid-face 19.8 kG, -89.0 deg.).

2.3 Coil Placement Errors

The HFD design contains only even normal multipoles because the magnet conductors are positioned with up-down, left-right symmetry. Any conductor position error destroys this symmetry and can generate a complete set of unwanted normal and skew multipoles. Random field errors due to conductor placement are caused primarily by the dimensional tolerances of the conductor, the coil insulation and coil shims. Systematic field errors due to conductor placement are associated with the coil molds, coil collars and press, and conductor motion under the influence of transport current and magnetic field. The field multipoles associated with the sum of the above error sources

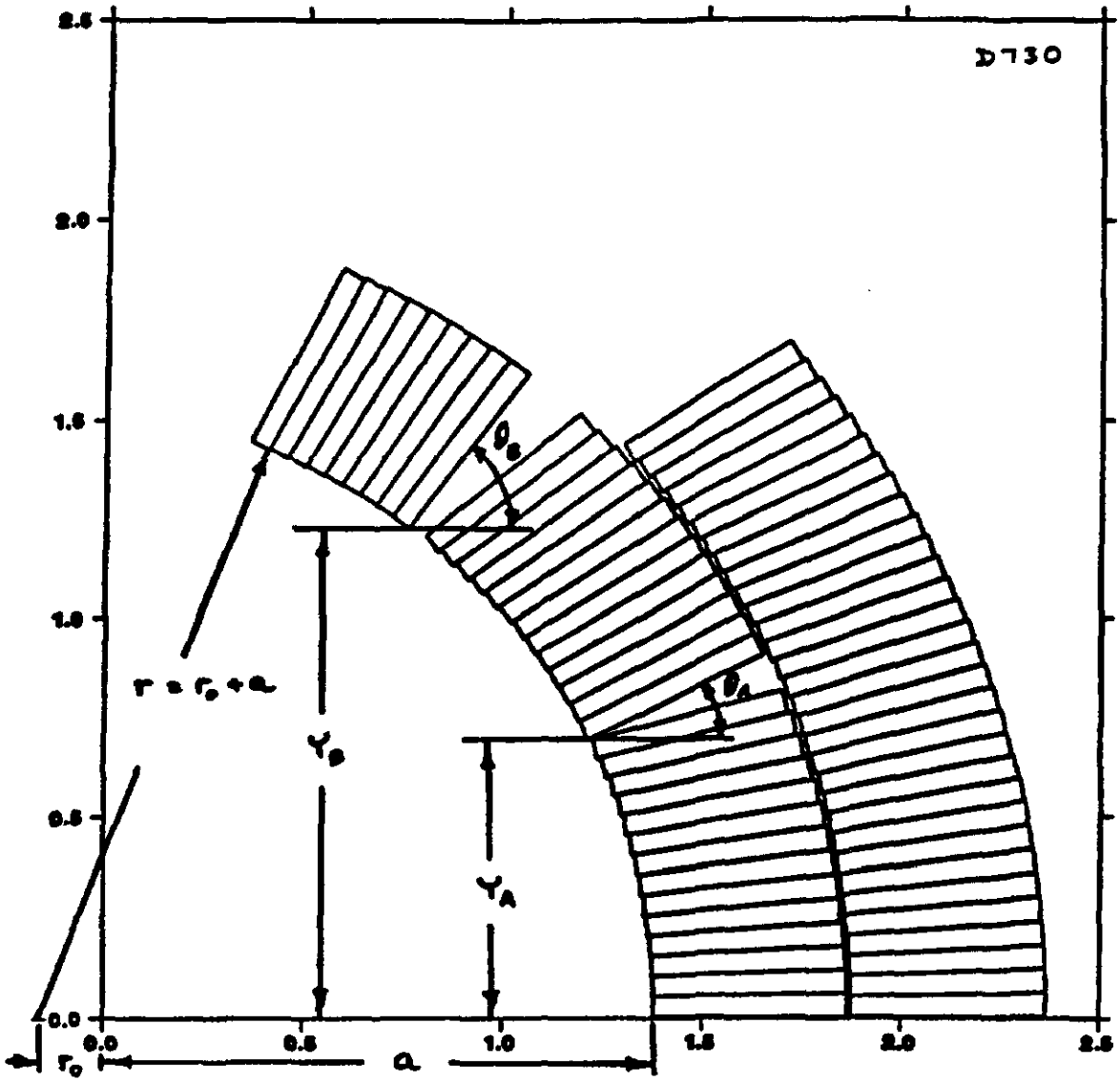

Figure 2.2: Cross section of one quadrant of a dipole

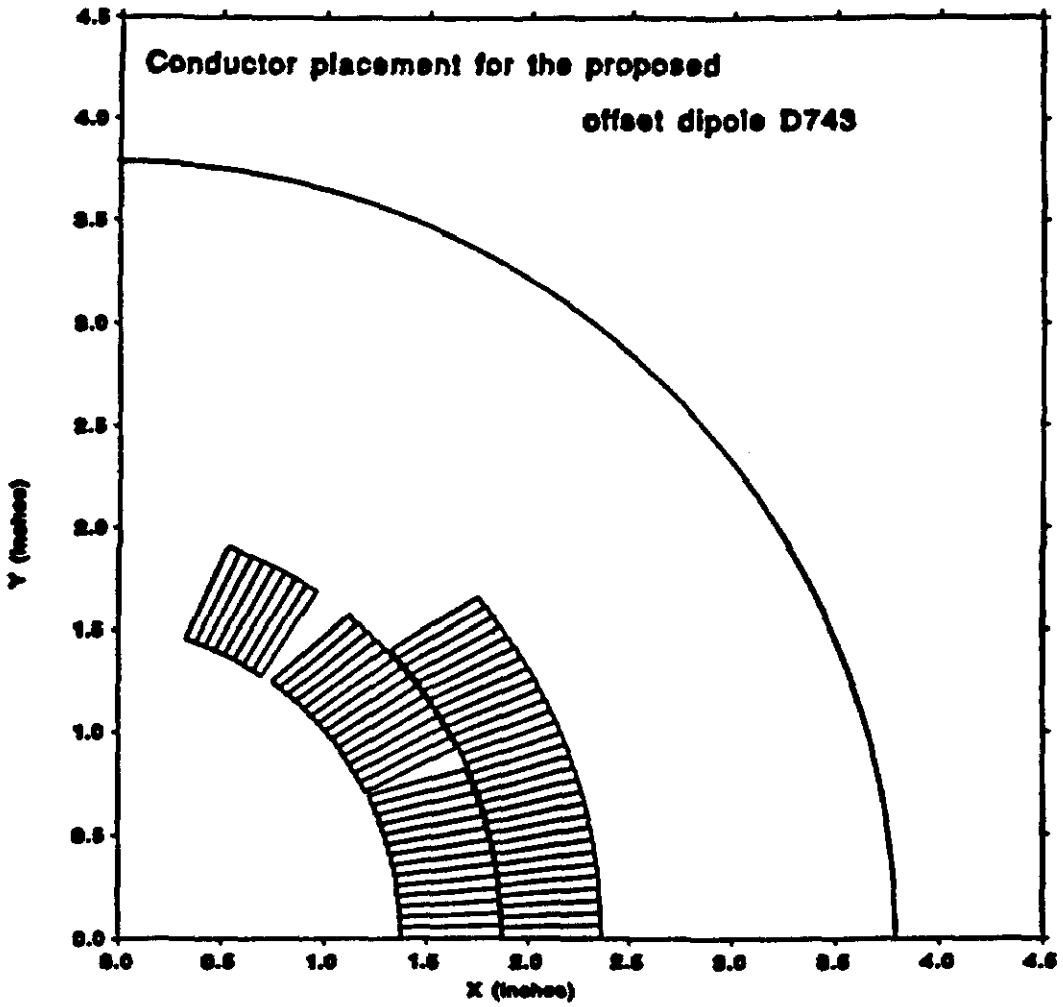

Figure 2.3: D743 conductor placement

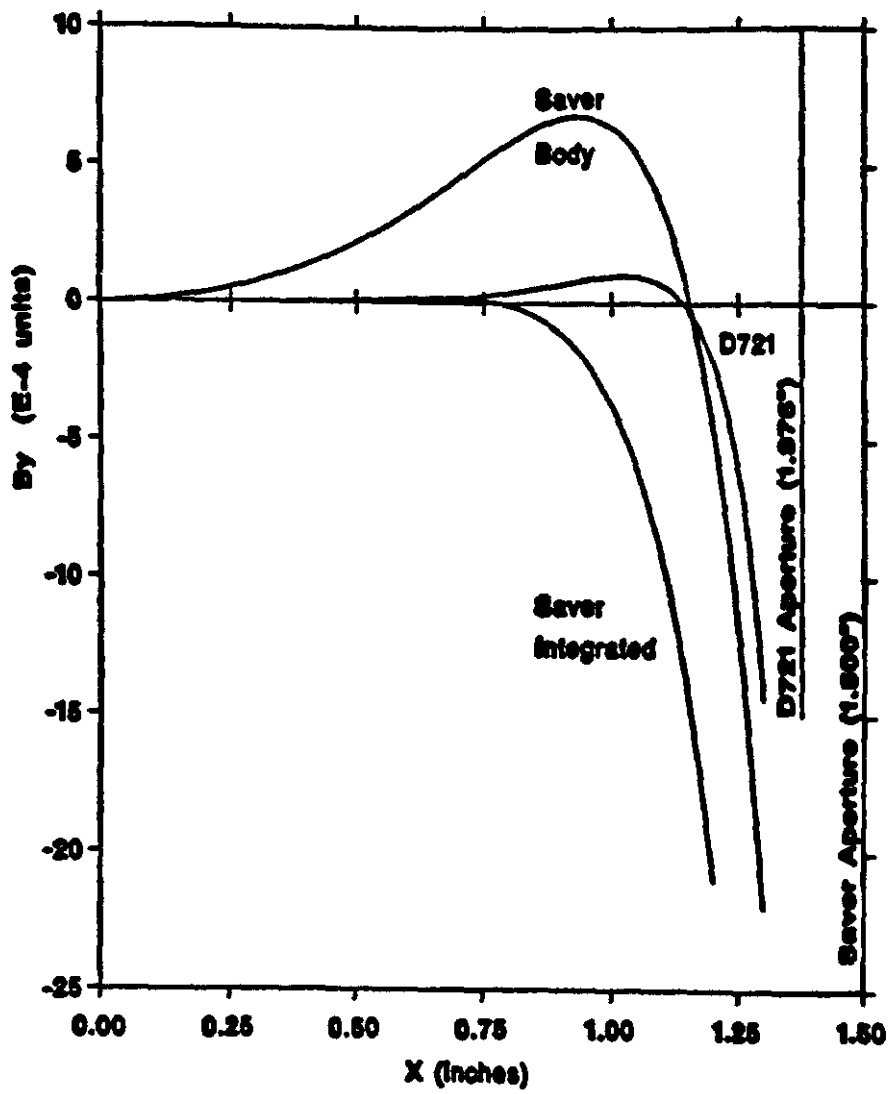

Figure 2.4: Comparing the saver dipole and the proposed offset dipole D721

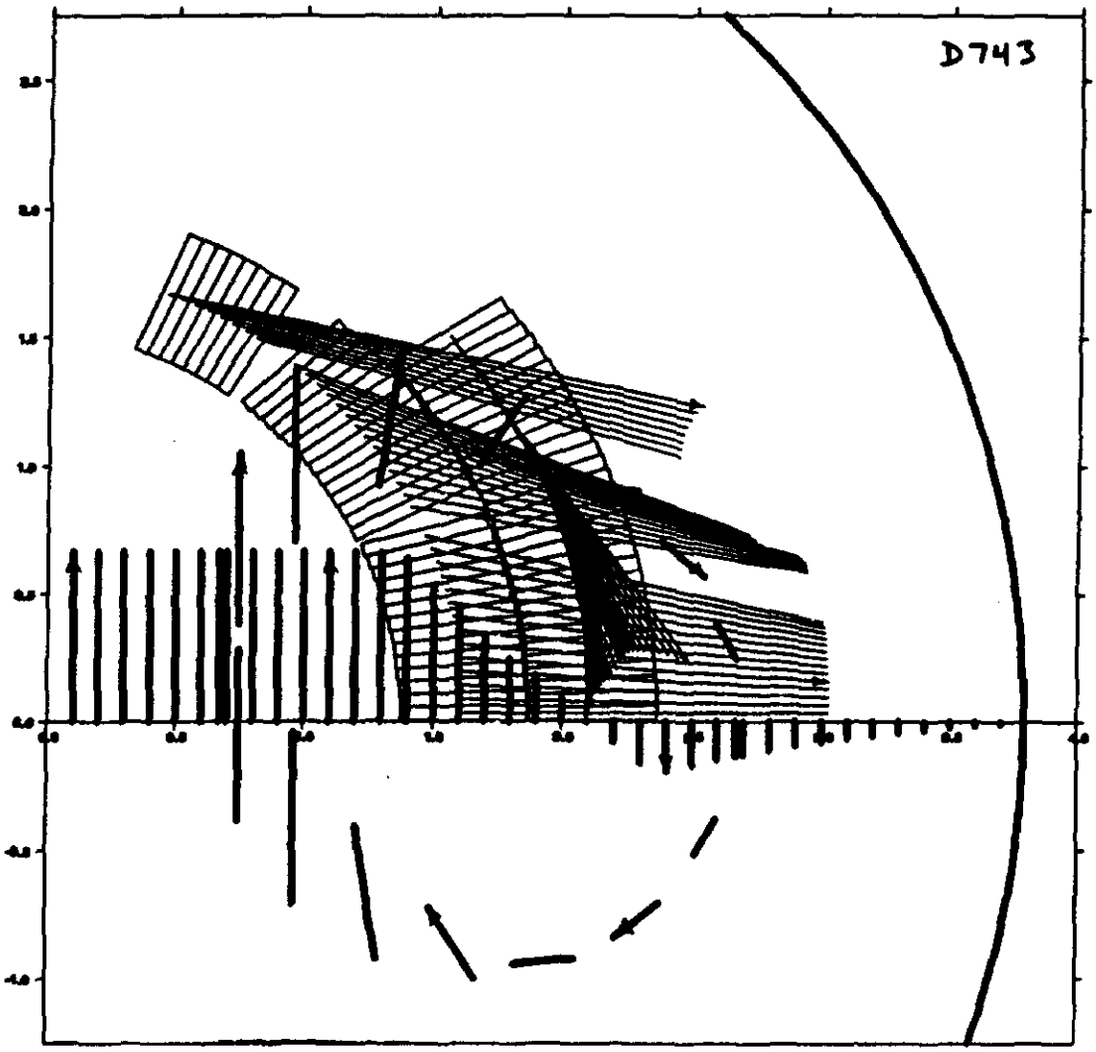

Figure 2.5: D743 forces on each conductor

need to be small or correctable with separate correction magnets.

An analysis that relates coil dimension errors to their field multipoles has been done for the Tevatron dipoles [15]. The conclusions of that analysis can be applied directly to the HFD design as the magnets are dimensionally similar. The analysis concluded: multipoles higher than decapole are not significantly effected by typical construction errors. The inner coil key surfaces and the inner coil median plane must be within 1.0 mil and 0.5 mil respectively to limit the quadrupole through decapole multipole errors to 2 units or less; the corresponding outer coil tolerances are a factor of 2 larger. The radii of the inner and outer coil need to be within 1.0 mil to limit the dipole error to 10^{-3}.

These tolerances are easily satisfied by the tooling and coil containment collars. They are assembled out of fine-blanked laminations which are stamped to a nominal tolerance of 0.1 mil, and after stacking into complete assemblies, are accurate to 0.5 mil. Large systematic errors of the tooling and collars, insofar as they do not cancel magnetically in the finished magnets, should be detectable through field measurements of prototype magnets and corrected prior to series production.

Cost limits the dimensional tolerances of series produced bare conductor, electrical insulation and coil shims to 0.3 mil, 0.5 mil, and 1.0 mil respectively. These tolerances are cummulative in the azimuthal direction of the coils and result in variable coil molding pressures, and when removed from the mold,

variable sizes and elastic moduli of the molded coils. When such coils are assembled in collars, the median plane adjusts to accommodate the up-down differences unless the coils are premeasured and matched. An indication of how successful this approach can be is shown in Table 2.8 where the measured multipoles of 870 production Tevatron dipoles [3] are listed.

Conductor motion due to the influence of the magnetic field on the transport current in the conductor can be separated into two approximately independent motions; the conductor motion due to the elastic deformation of the coil containment collar and the azimuthal motion of the coils within the collar. It is assumed that the collar will be essentially rigid. This assumption is valid as long as the collar is supported after cooldown with zero clearance within a massive iron yoke.

The expected azimuthal conductor motion in the collar has been calculated for a HFD at an 8.8 T bore field and is shown in Fig. 2.6. The calculation assumes a coil elastic modulus of 3.0 MPSI and sufficient preload to hold the coils against the collar keys (a minimum of 5040 lb/in. for the inner coil, 2480 lb/in. for the outer coil). The calculated conductor displacements are proportional to the the square of the dipole field and inversely proportional to the elastic coefficient of the coil. Room temperature measurements of the coils at a pressure of 10 KPSI have yielded elastic coefficients of 1.5 MPSI. This is expected to double at LHe temperature and the HFD preload of 20 KPSI.

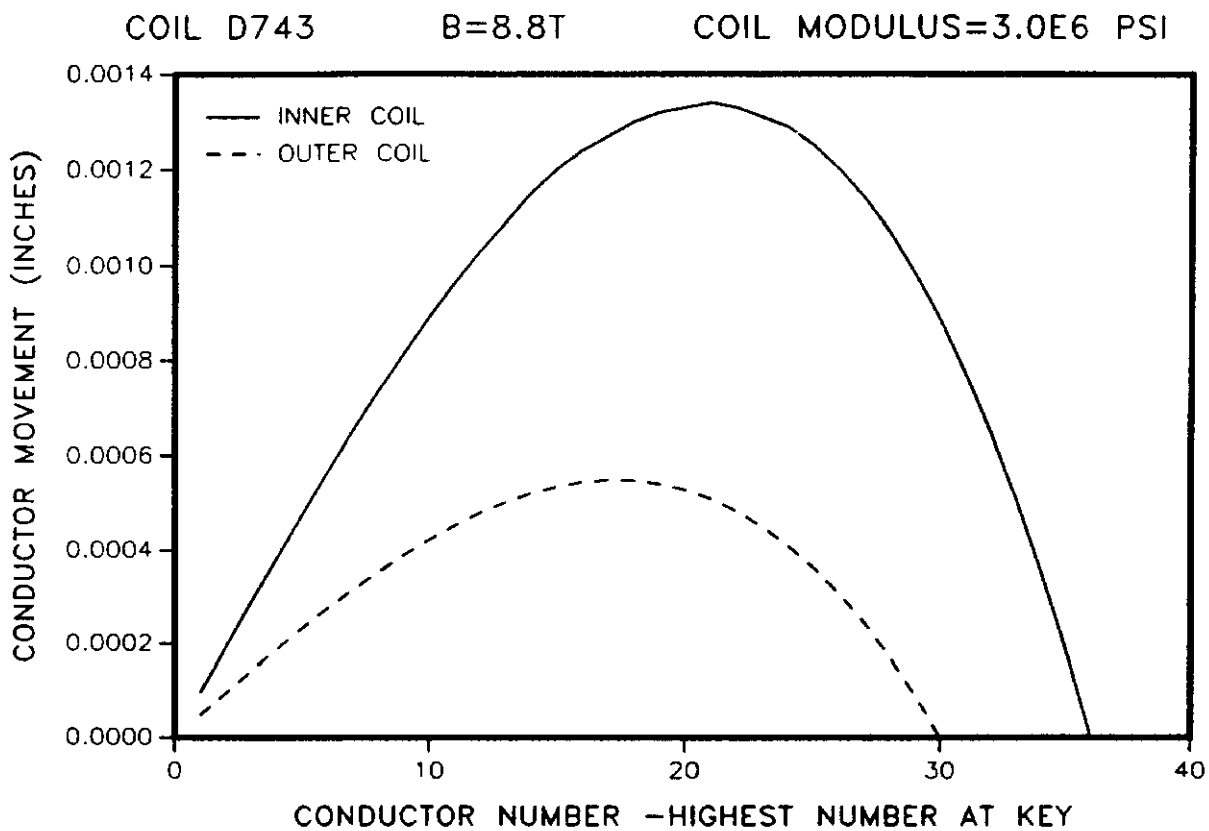

Figure 2.6: Azimuthal Conductor Motion

Pole	b(n)	b(n)		a(n)	
n	Design	Mean	RMS	Mean	RMS
1	0.09	0.48	0.17	0.50	-
2	0.04	0.95	3.12	0.10	1.16
3	-	-0.23	0.77	-0.07	1.46
4	1.04	-0.57	1.32	-0.10	0.46
5	-	-0.07	0.32	-0.07	0.55
6	4.44	5.48	0.54	-0.07	0.29
7	-	0.04	0.17	0.22	0.26
8	-12.09	-12.52	0.33	-0.07	0.41
9	-	0.02	0.23	0.28	0.38
10	3.63	3.70	0.26	0.08	0.25
11	-	-0.01	0.20	-0.24	0.25
12	-0.82	-0.80	0.19	-0.05	0.22

Table 2.8: Tevatron Dipole Field Coefficients. Average of 870 magnets at 4000A. Coefficient units 10^{-4} at 1.0 in

A symmetric azimuthal compaction of the coils towards the magnets median plane primarily effects the sextupole coefficient. The conductor displacements plotted in Fig 2.6 change the sextupole of the HFD by an estimated 2.0 units.

2.4 Time Varying Field Effects

This section will explore the heat load associated with the cyclic field of the magnet, and the eddy current forces on the cryostat during rapid current decay.

The cyclic heat load determines the required refrigerator capacity of a fast

cycling accelerator if the cryostats have been designed to minimize heat leak. The cyclic heat load also effects the operating temperature, and therefore the peak field of the magnets. Also, the magnet cryostats must be compatible with the internal heat sources of the magnets. Otherwise, thermal gradients within the magnet coils might appreciably effect the high field limit of the magnet.

The eddy currents, that under normal operation of the magnet contribute to the heat load of the magnet, can stress the cryostat during the extremely rapid current decay required for coil quench protection. An estimate of these forces is presented for the HFD.

2.4.1 CYCLIC HEAT LOAD

Hysteresis and eddy current heating are present in the iron yoke and superconducting cable. The heat load from the aluminum collar and stainless steel bore tube are due to eddy currents only. The losses due to inelastic mechanical motion in the flexing coil and collars are ignored.

The hysteresis loss due to the open magnetization cycle of the iron yoke is given by the formula:

$$E = \int dV \oint \frac{BdH}{2} \tag{2.1}$$

The energy loss (E) per magnetic cycle is expressed in joules when the magnetic induction (B), the magnetic intensity (H) and the steel volume (V) are in units of tesla, ampere-turn per meter, and cubic meters respectively.

In lieu of an exact integration of the loss integral over the volume of the iron yoke, an upper limit estimate can be obtained with an average magnetic induction $< B >$ in the iron defined by:

$$< B >= \frac{B_o R_1}{R_3 - R_2} \tag{2.2}$$

where B_o is the magnetic induction of the bore; R_1 is the inner radius of the coil; R_2 and R_3 are the inner and outer radii of the yoke respectively. At a HFD bore field of 8.8 T, $< B >$ has a value of 2.3 T.

Fig 2.7 shows the B(H) curve for a sample of coated laminations of magnet steel. The field cycle was specified to measure the steel's coersive force (.576 Oe for 100 Oe). Using the steel characteristics of Fig. 2.7 , equations (2.1) and (2.2), the energy loss per cycle per meter of HFD collar has been estimated at 16.4 J/m for a zero to 8.8 T bore field cycle .

The energy loss (E) per cycle per unit volume in the HFD superconducting coils can be estimated by scaling Tevatron dipole loss data with the empirical relation:

$$E = \frac{c_1 d J_c B_m}{(1+k)} + c_2 \dot{B}_o B_m \tag{2.3}$$

The first term represents the hysteresis of the superconducting cable; the second term the eddy current loss. The term $1 + k$, where k is the copper to superconductor ratio of the cable, assures that the hysteresis loss is evaluated only for the superconductor volume. The eddy current loss is evaluated for the total metallic volume of the coils. B_m and $\dot{B}_o$ are the range and rate of change of the magnet's bore field during the magnet cycle. J_c and d are the

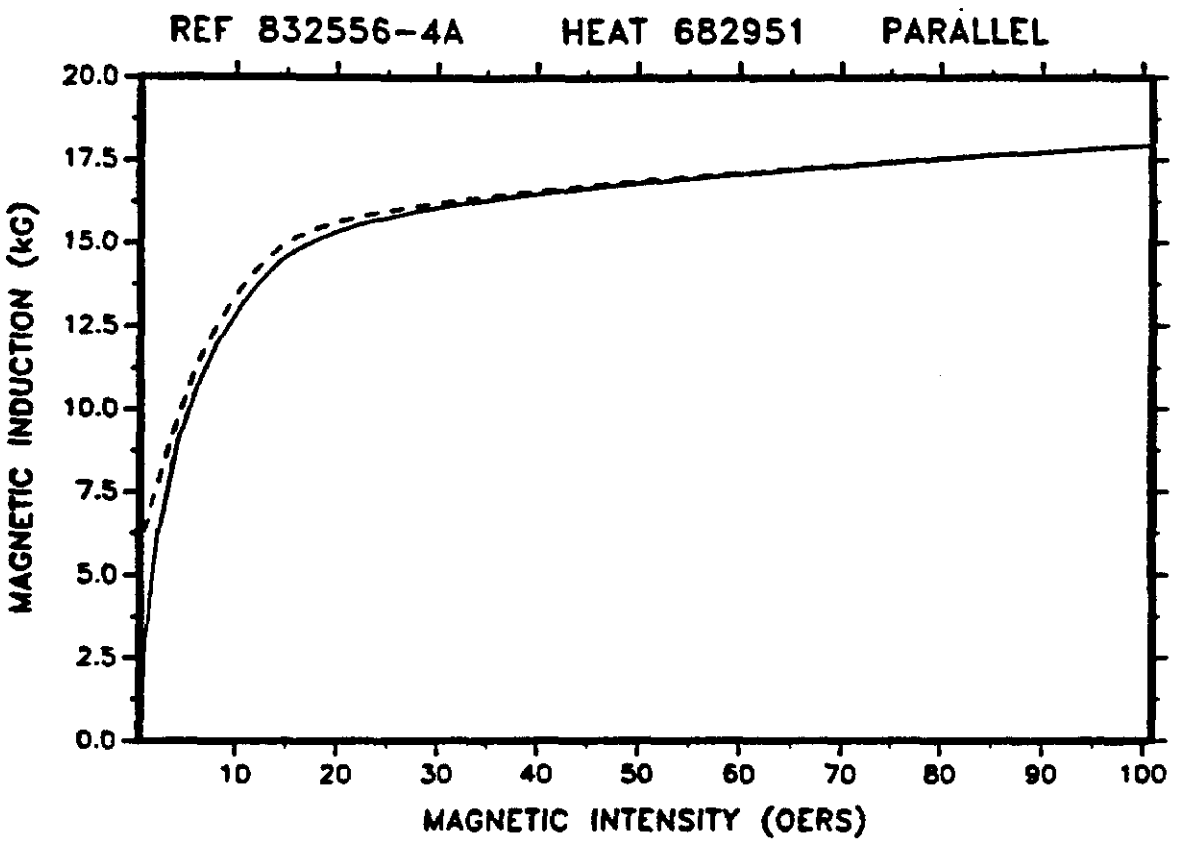

Figure 2.7: Steel B(H) Curve

cable critical current and filament diameter with J_c arbitrarily evaluated at the average bore field of the magnet cycle. The constants c_1 and c_2 can be evaluated using the Tevatron dipole loss data in Figs 2.8, 2.9 and Table 2.9

The Fig. 2.8 data [16] are the average loss per cycle of several Tevatron dipoles. Fig. 2.9 shows the loss per cycle of two specific Tevatron dipoles. The Table 2.9 data [6] are the losses measured for two R-series magnets. These magnets have cross sections identical to the production Tevatron dipoles but are 32 in. long and have been constructed with different cable for testing. The above Tevatron loss data have been scaled to a 4000 A peak, 200 A/s cycle and averaged to yield an average Tevatron dipole coil hysteresis loss of 355 J/cycle and an average Tevatron dipole coil eddy loss of 56 J/cycle. These losses have been used to calculate the Tevatron magnets' watts listed in Table 2.10. These losses and eq. (2.3) have also been used to estimate the HFD coil losses listed in the table.

The eddy current heating power per unit volume (P) in the yoke or collar laminations can be expressed as:

$$P = \frac{\dot{B}^2_{y,c} t^2}{12\rho} \tag{2.4}$$

P is in units of W/m^3, $\dot{B}^2_{y,c}$ is the rate of change of the magnetic induction (T/s) in the yoke or collar, t is the thickness of a lamination (m), and ρ is the resistivity of the lamination material (Ω m) at the operating temperature of the magnet. This loss expression assumes that the laminations are coated to eliminate current flow between laminations.

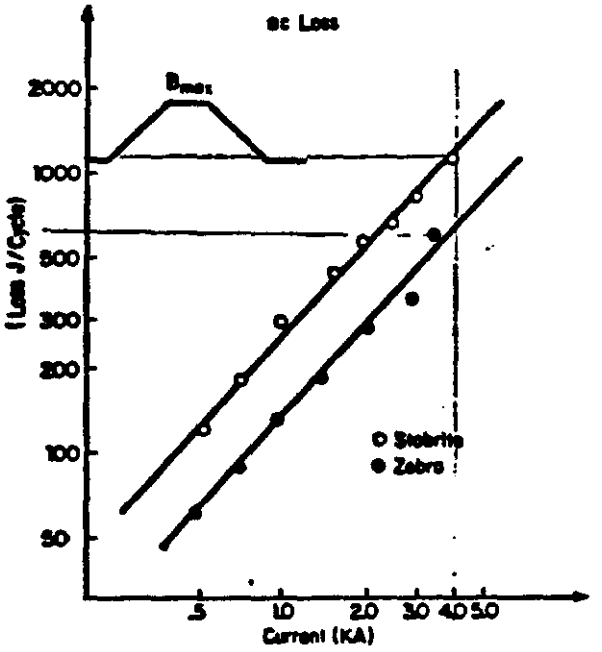

Energy loss/cycle vs. excitation current for several conductors in magnets from the Doubler program.

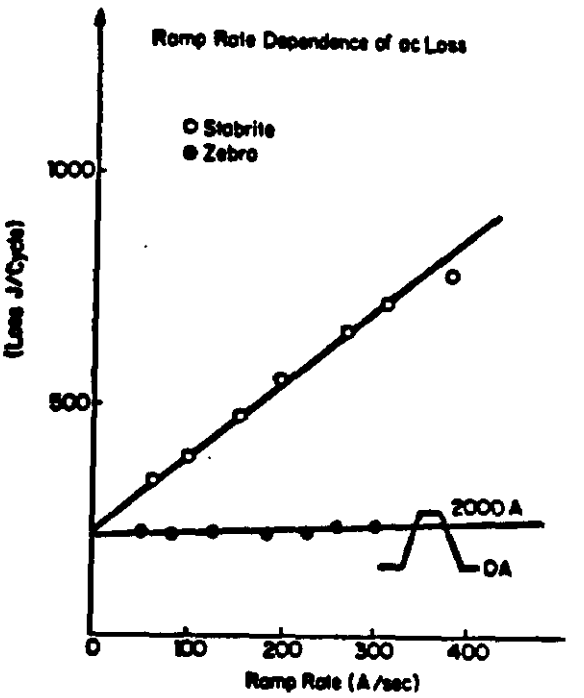

Energy loss/cycle vs. ramp rate for several conductors in magnets from the Doubler program.

Figure 2.8: Energy loss/cycle vs excitation current

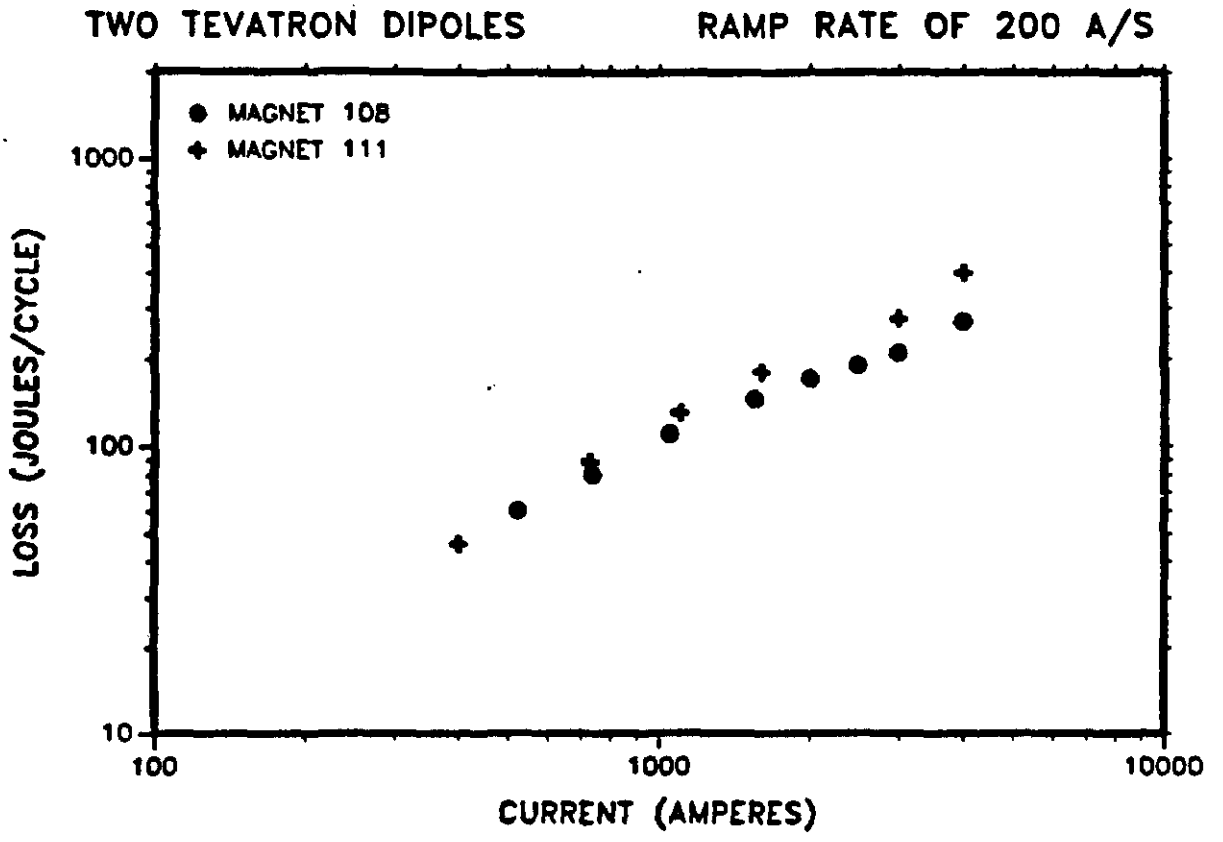

Figure 2.9: Energy loss/cycle vs ramp rate

The eddy current heating power per unit volume (P) of non-laminated cryostat surfaces such as the bore tube can be calculated using the relation:

$$P = \frac{\dot{B}_a^2 x^2}{\rho} \tag{2.5}$$

$\dot{B}_a$ is the rate of change of the average magnetic induction (T/s) enclosed by the cryostat element. The distance x (evaluated in m) is the location of the cryostat element, measured relative to the dipole vertical plane of symmetry.

A summary of the loss calculations are shown in Table 2.10. The eddy current losses in the stainless steel collar and bore tube of the Tevatron dipole are small and are included in the listed coil eddy current loss. The yoke losses of the Tevatron dipole - not deposited in the cryostat as the dipole has warm iron - are not listed. The cycle times of the HFD were arbitrarily adjusted to yield a field rate equal to that of the Tevatron dipole. The dominant loss at these ramp rates is due to the hysteresis loss of the supercondutor followed by the eddy current loss in the cable. The cable hysteresis losses are larger in the HFD than in the Tevatron because of the HFD's larger coil volume, larger field swing and higher cable critical current. The estimated HFD's coil eddy current losses are critically dependent on the strand coating and coil preload and could differ significantly from the listed estimates. The remaining loss contributions are relatively small and in the case of lamination losses, can be reduced further by choosing thinner laminations.

<u>Iron Yoke</u>

Ramp Rate (A/sec)	10 μm filaments Loss/Cycle (J/cycle)	20 μm filaments Loss/Cycle (J/cycle)
12	22.5	50.
24	23.	52.
50	24.6	50.5
100	26.	56.
200	29.	56.3
300	31.	58.
400	37.	61.
Hysteresis Loss	22.5	50.
Eddy Loss	14.5	11.

Table 2.9: Energy Loss Per Cycle For R-Series Test Magnets. Test Conditions: 32 in. magnet length, no iron, therefore 8.0 G/A ,all data with 4000 A peak cycle

Dipole	Tevatron	HFD	HFD
Peak Field (T)	4.0	6.6	8.8
Cycle (s)	20-20-20	33-20-33	44-20-44 (up-flattop-down)
Period (s)	60	86	108
Magnet Length (m)	6.12	6.12	6.12
Yoke Hysteresis (W)	-	1.17	0.93
Eddy	-	0.24	0.25
Collar Eddy (W)	*	0.55	0.55
Coil Hysteresis (W)	5.9	11.7	15.5
Eddy	.93	2.27	2.57
Bore Tube Eddy (W)	*	.10	.10
	6.83 W	16.03 W	19.90 W

Table 2.10: Cyclic Energy Loss Summary

Lamination thickness 0.1 in.

Resistivity @ 4K 4 10-7 Wcm

Aluminum Collar

Lamination thickness 0.1 in.

Resistivity @ 4K 5 10-8 Wcm

Stainless Steel Bore Tube

wall of cylindrical tube 0.1 in.

Resistivity @ 4K 5.5 10-5 Wcm

2.4.2 Eddy Current Forces

During a quench, the magnet current has to be rapidly removed in order to prevent damage to the superconducting cable. For a quenching HFD at 8 kA, the current decay reaches a maximum rate of 39.7 kA/s which corresponds to a 44.7 T/s rate of change of the dipole's bore field. The more delicate cryostat components such as the bore tube or the thermal shield need to be sufficiently strong to withstand the eddy current forces that result from this field change, especially if they are fabricated out of high thermal conductivity metal - and therefore low electrical resistivity - to promote heat transfer.

The force per unit volume (F) in the two-dimensional part of the magnet can be calculated with the formula:

$$F = \frac{\dot{B}_a B x}{\rho} \tag{2.6}$$

where $\dot{B}_a$ is the average rate of change of the magnetic induction (T/s), B is

the magnetic induction (T) at the location of the cryostat element and x is the distance (m) of the element from the dipole's vertical plane of symmetry. The other parameters of this equation have been defined previously. In the case of a dipole bore tube, the eddy current force is outward, perpendicular to the vertical plane of symmmetry, and opposed to the quench related pressure of the expanding helium. A cylindrical bore tube of uniform wall thickness will therefore experience its maximum eddy current pressure at the points where it intersects the magnet's median plane. For an 8 kA quench in the HFD with a stainless steel bore tube of average radius 1.25 in. and wall thickness 0.1 in., this maximum pressure is 6.3 PSI. This pressure is small relative to the helium pressure rise during a quench. A 0.125 in. wall thickness aluminum heat shield, located at a radius of 10 in., experiences a maximum eddy current pressure of 2.7 PSI. The shield supports and the shield structure must be designed to withstand this pressure.

2.5 Quench Protection

2.5.1 Quench Protection System

The quench protection system has to be compatible with the dual operating modes anticipated for this magnet. When the accelerator operates as an injector or fixed target accelerator, the magnets will cycle repeatedly to 6.6 T at a fast ramp rate. When the accelerator operates as a collider, the magnets operate at 8.8 T, albeit at very reduced ramp rate and with as few

as one magnetic cycle per day.

A quench protection system similar to the Tevatron system [2] has been explored as it can be designed to satisfy these operating conditions. The Tevatron uses safety leads located at every other lattice quadrupole to divide the magnet circuit into quench protection cells. These leads, and thyristors at room temperature, bypass the circuit current out of the cell that contains the quenching magnets. Quench heaters are mounted in every dipole to increase the quench resistance. The increased quench resistance reduces the peak temperature at the origin of the spontaneous quench. The heaters also distribute the cell's magnetic energy among the cell's magnets and promote a magnet by magnet inductive/resistive voltage cancellation.

Other types of quench protection systems such as cold diode shunts appear less suitable because of the ramp rate. The dipole is expected to be between 5 m and 15 m long. A modest 100 A/s ramp rate results in a ramp voltage between 5 V and 15 V per dipole which is at best marginal for cold diodes unless several diodes per magnet are connected in series. If a future application for this magnet is found were a fast ramp rate is not required, a cold diode quench protection system can be reconsidered. If cold diodes are not used, it makes sense to use quench heaters even if the magnets can be shown to be selfprotecting. The use of quench heaters permits an arbitrarily wide spacing of the safety leads to reduce the heat leak associated with them.

This report will not attempt to present a detailed power circuit. That

would require a knowledge of the lattice, as the number of heater protected magnets in a quench protection cell is usually determined by the quadrupole spacing. Sufficient calculations have been made to show that a quench heater geometry can be devised to protect this magnet up to a field of 8.8 T.

2.5.2 Cable Quench Temperature

During a quench, the superconducting cable switches to the electrically resistive state, and the cable temperature rises due to ohmic heating. This temperature rise can be calculated using the heat diffusion equation, if the thermal and electrical parameters of the cable constituents, including helium, are known as a function of temperature. For the purposes of quench protection, we are primarily interested in the case of high current density that occurs when the magnet operates near its short sample limit. For typical superconducting cable operating near the short sample limit in accelerator magnets, the temperature change is approximately adiabatic, i.e., the loss of energy per cable segment due to heat propagation through the segment boundaries is small relative to the ohmic heating. In this case, the heat diffusion equation reduces to the following simplified form:

$$A^2 \int \frac{cdT}{\rho} = \int I^2 dt \tag{2.7}$$

The right term of the equation represents the square of the cable current (I) integrated over time (t). When this term is evaluated in units of $10^6 A^2 s$, it is the jargon term expressed as Miits. The left term of the equation is

a function of cable temperature (T). The cable resistivity (ρ) and the cable specific heat (c) are effective values averaged over the cable sectional area (A).

The cable temperature as a function of quench Miits has been calculated using eq. (2.7). The results are plotted in Fig. 2.10. for three magnetic fields to show the effect of magnetoresistance. A copper resistivity ratio of 55, a value obtained from recent Tevatron low β cable measurements, was assumed in the calculation. The cable area was obtained by summing the areas of the individual cable strands. The results of Fig. 2.10 also include a small correction for the heat capacity of the cable electrical insulation.

The quench protection system needs to limit the peak quench temperature to approximately 500 K or less. The average temperature of the magnet after a quench is an order of magnitude less. The onset of cable damage for cables with Kapton insulation is approximately 800 K if the cable is allowed to cool immediately. The highest magnetic field in the HFD occurs at the cable next to the collar keys. At a bore field of 8.8 T, this cable experiences an average field of 8.46 T. In order to limit the quench temperature to 500 K for a quench at this location, the total Miitage must be limited to 13.6 Miits.

2.5.3 Heater Considerations

The quench Miitage accumulated in a heater protected magnet at the spontaneous quench origin can be divided into three parts: The Miitage accumulated prior to quench detection; the Miitage accumulated during the delay

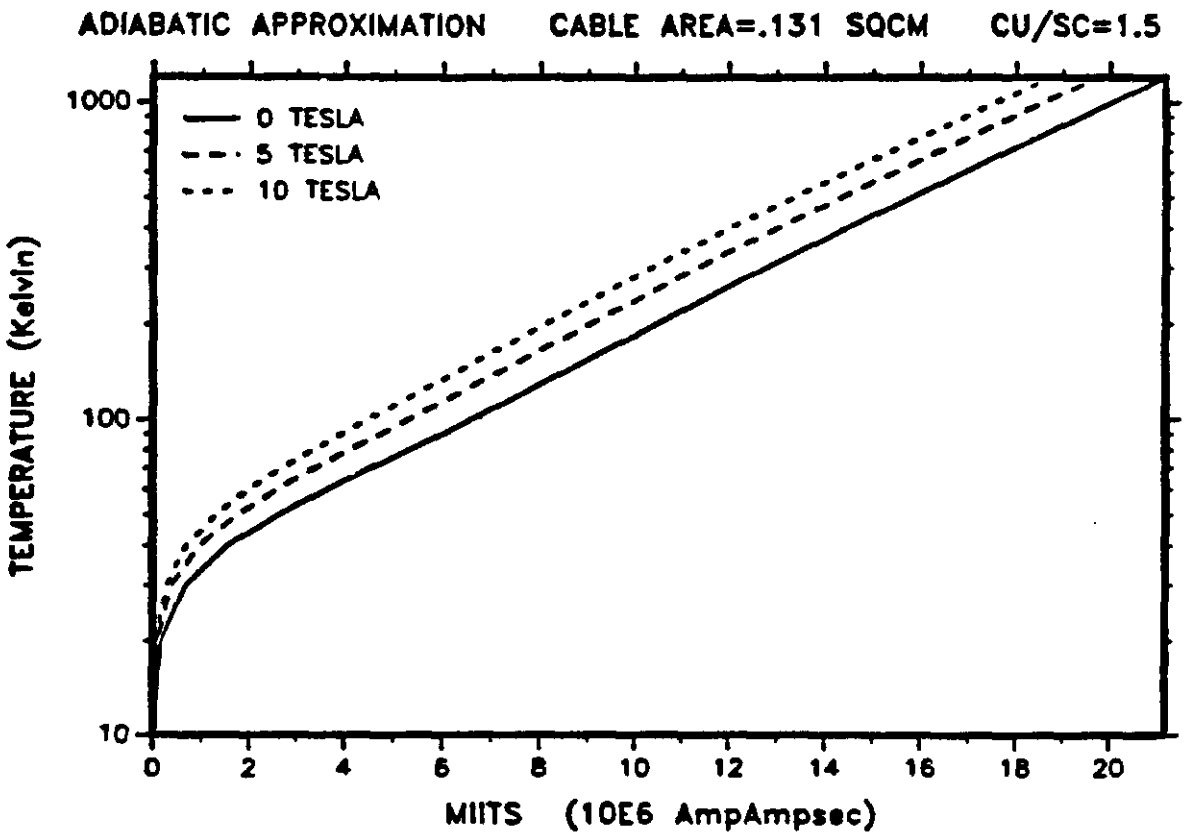

Figure 2.10: Cable temperature vs cable Miits

between the start of heater current and the onset of the heater produced quench; and the Miitage that accumulates during the current decay of the magnet.

The spontaneous quench resistance is normally small relative to the quench resistance caused by the heaters and will be ignored in the current decay analysis. However, the spontaneous quench resistance determines the initial quench resistance voltage which along with the quench detection threshold, determine the quench detection delay. With the HFD operating at 8.8 T, its cable current density is identical to the peak current density of the Tevatron D0 low β two-shell quadrupoles [7]. The low β magnet spontaneous quench voltage reached 1.0 V in 17.12 ms. The HFD spontaneous quench voltage growth rate with the bore field at 8.8 T is expected to be similar. In this report, it is assumed that the filtered quench voltage will reach a 0.25 V quench detection level within 32 ms.

A possible heater geometry is shown in Fig. 2.11 . The heaters consist of .001 in. thick stainless steel strips, one per magnet quadrant, that are centered within the .020 in. thick Kapton insulation that separates the outer coils from the containment collar. Each strip can be energized separately or in series/parallel to optimize the heater power supplies. Spot heaters are also possible. They minimize the required heater power supply energy but have a longer effective heater quench delay as most of the magnet resistance is due to quench propagation after the coil spots have quenched. A third possibility

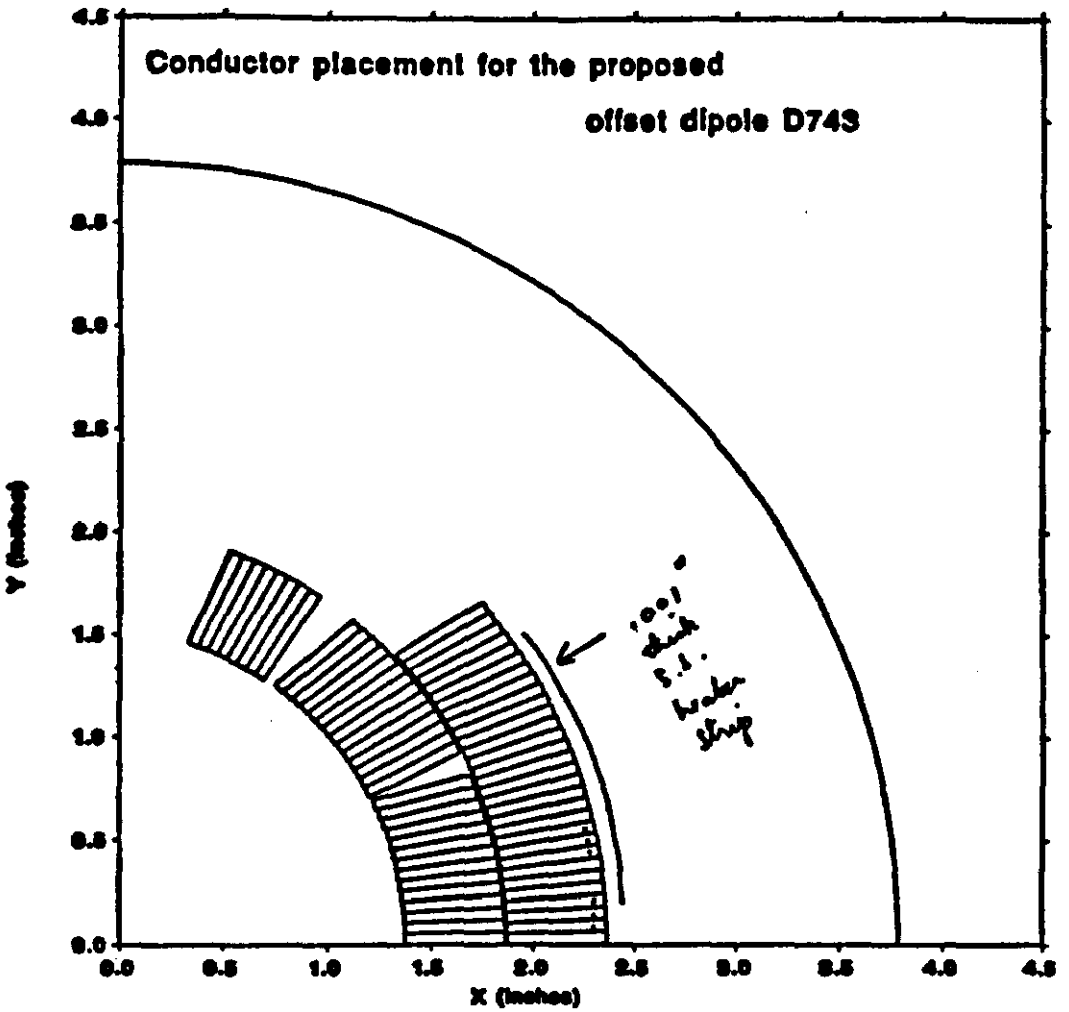

Figure 2.11: Conductor placement for the proposed offset dipole D743

is to place the heater strips within the insulation that separates the inner and outer coils. This has the advantage of simultaneously quenching the inner and outer coils which results in a more uniform resistive, inductive voltage cancellation during the quench current decay as well as quenching more wires, thereby decreasing the time for the magnet current decay. The final heater geometry design should include the lattice and heater power supply efficiency as a constraint.

A version of the Tevatron heater power supply can be used to power the quench heaters. This power supply consists of capacitors that are discharged into the heaters. The Tevatron supply uses a 6.6 mF capacitor bank which is charged to 450 V for a stored energy of 668 J. The supply voltage is limited by the ability of available electrolytic capacitors but the supply energy is readily adjusted by adding or subtracting capacitors. The stainless steel strips require an initial current density of approximately 12 kA/cm^2 to quench the magnet within 35 ms. The heater power supply stored energy must also be sufficient to quench the magnet at the accelerator injection current.

The current decay and the accumulated Miitage during current decay for an 8 kA quench as a function of the number of magnet wires quenched by the heaters is shown in Fig. 2.12 and Fig. 2.13. The calculation assumes that the heaters are continuous (no spots) and that they are imbedded between the outer coil and the containment collar. Time starts at the instant when the heaters have quenched the wires. The miitage accumulated after the heaters

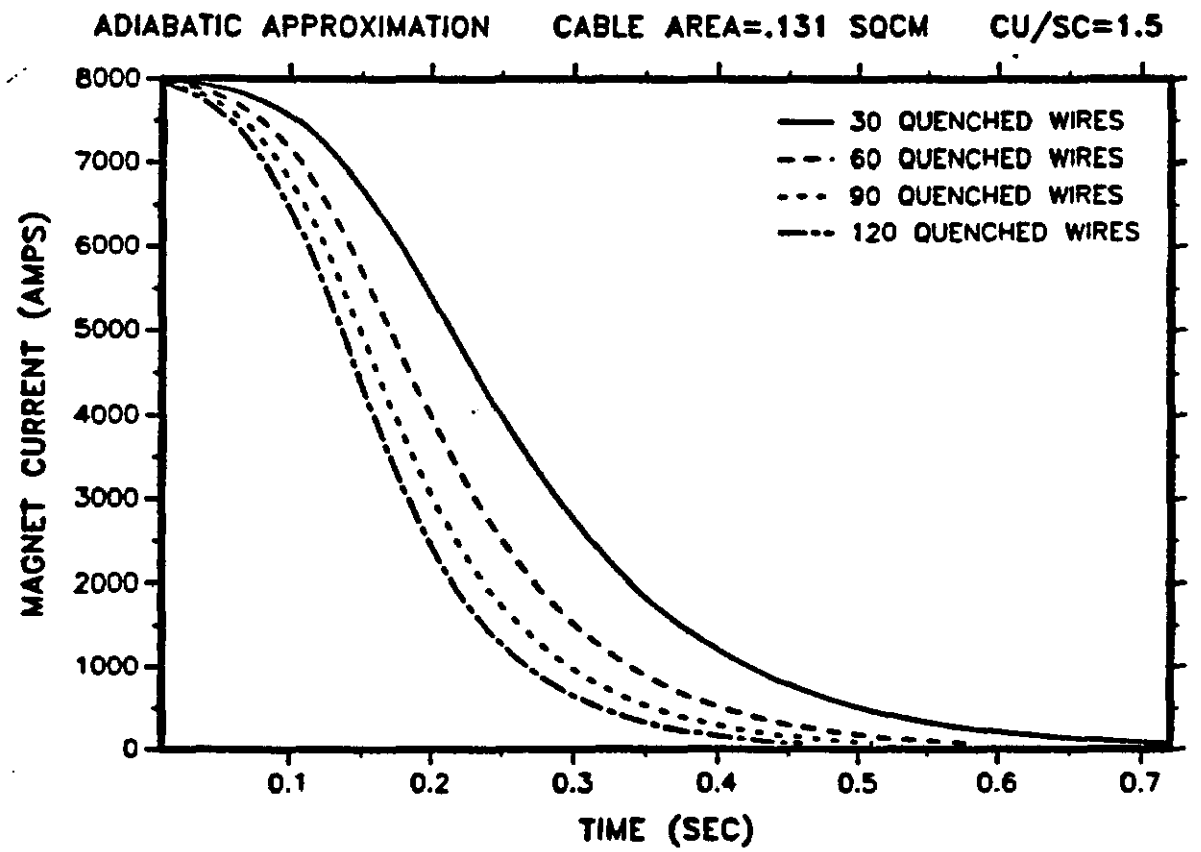

Figure 2.12: Heater induced magnet current decay

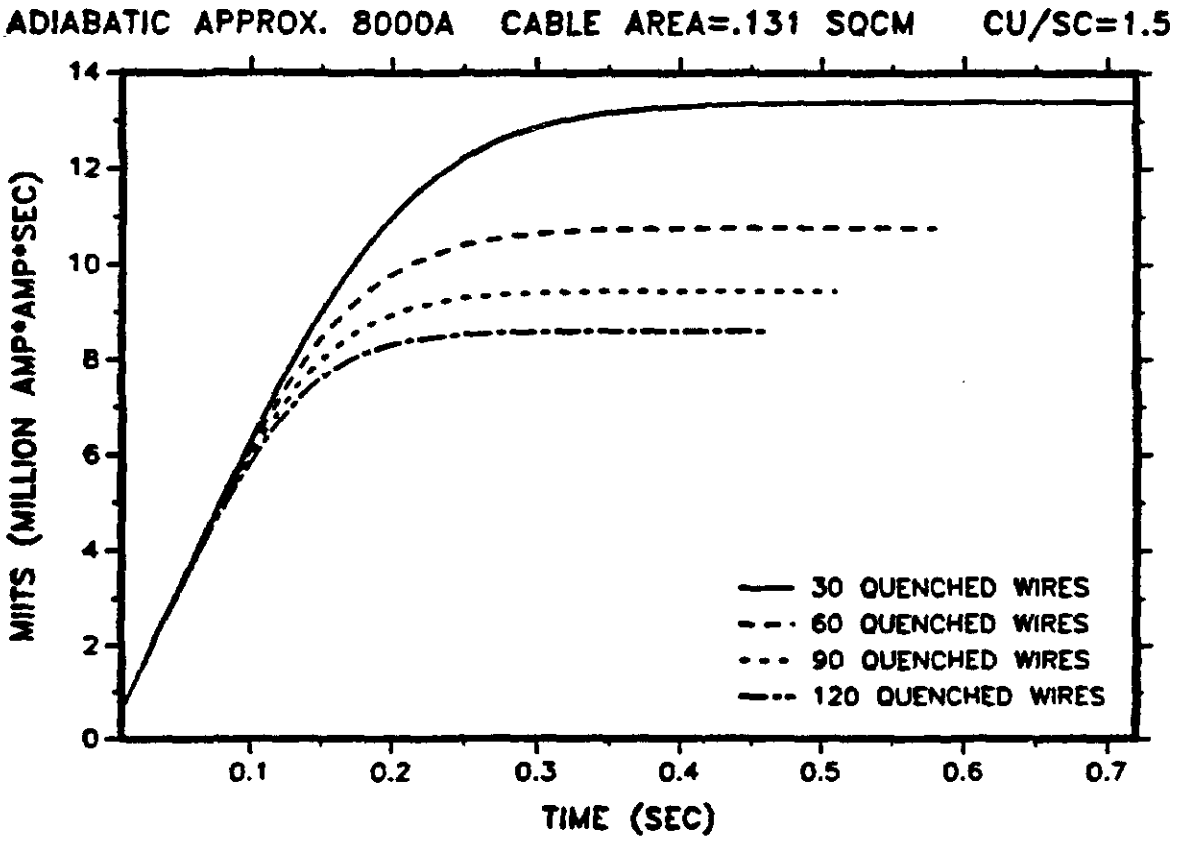

Figure 2.13: Heater induced quench Miits

have quenched the coil can be reduced by increasing the area of the heaters in order to quench more wires.

The HFD design has 120 wires (60 turns) in the outer coil. If each of the 4 heater strips covers 20 wires, sufficiently large gaps for voltage isolation remain between heaters and a total of 80 wires will be quenched by the heaters. The magnet's current decay, the magnet's voltage, and the miitage accumulated during the current decay has been calculated for several currents with 80 wires quenched with heaters. The results are shown in Figs 2.14,2.15,2.16. At 8 kA, the inductive voltage per meter of magnet length is 420 V. Long magnets must have adequate resistive/inductive voltage cancellation to prevent voltage breakdown. The accumulated miitage during current decay from 7.81 kA (8.8 T bore field) is 9.6 Miits. The spontaneous quench experiences an additional 4.1 Miits during quench detection and heater quench delay for a total of 13.7 Miits (approximately 500 K).

2.6 Yoke Design

2.6.1 Iron Effects

The iron yoke, in addition to holding the coils rigidly in place acts to give a substantial field enhancement. The iron contribution to the field can be analytically computed for a finite or infinite permeability μ. The problem becomes analytically intractable when μ itself becomes a function of field, i.e $\mu(H)$, leading to a nonlinear problem. Numerical methods, such as POIS-

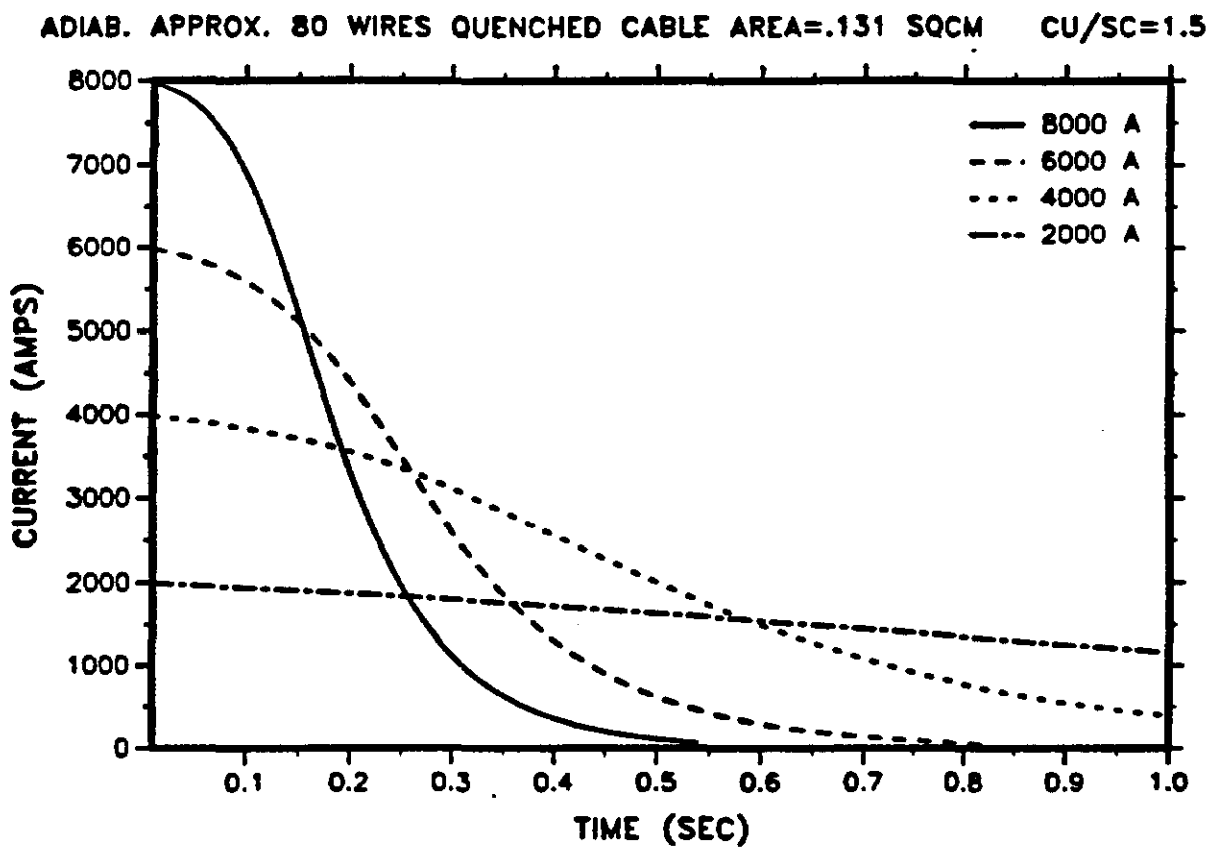

Figure 2.14: Heater induced current decay

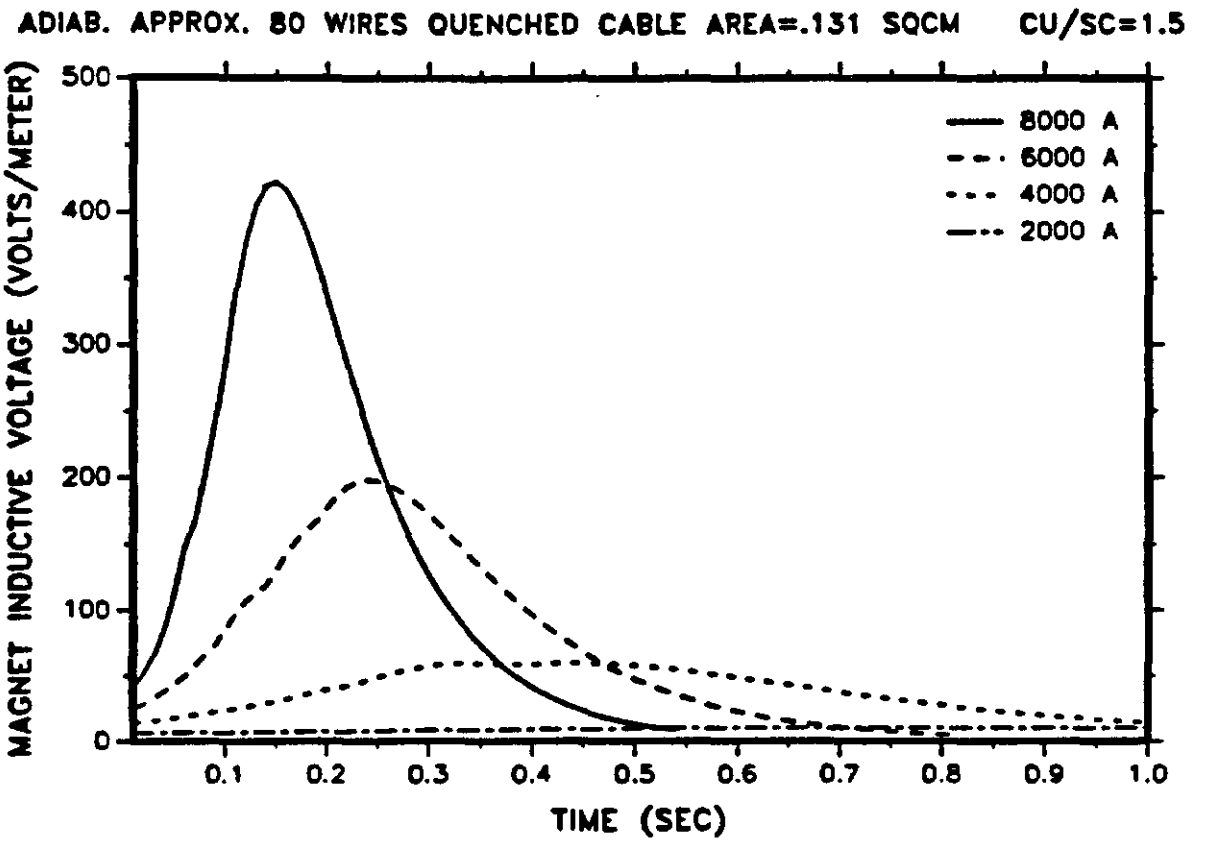

Figure 2.15: Heater induced inductive voltage

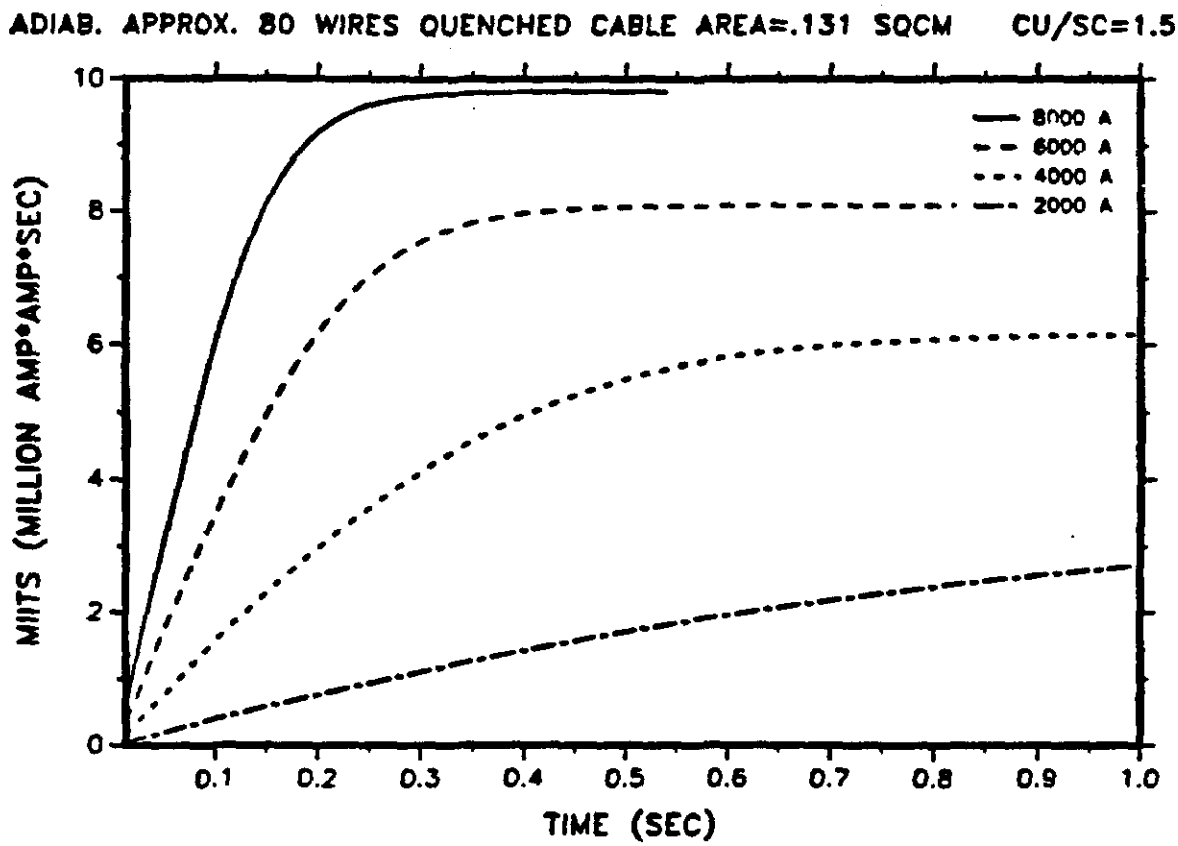

Figure 2.16: Heater induced quench Miits

SON, have been widely used to solve such problems. A major concern at high fields is iron saturation and its effects on multipoles, mainly sextupole. Factors that contribute to such effects had to be first analyzed before a yoke design is suggested. Below is a discussion of these different effects.

Infinite μ Case

This is the simplest case to solve analytically. Given a current element dI in a region surrounded by a cylindrically shaped infinite μ iron, as shown in Fig 2.17, the problem is solved by the method of images. The complex field element produced at a point $z = z_o$ is given by

$$dB^* = \frac{\mu_o}{2\pi} dI \left\{ \frac{1}{z - z_o} + \frac{1}{\frac{R^2}{z^*} - z_o} \right\} \tag{2.8}$$

where $z = \rho e^{j\phi}$ from Fig 2.17. For a distributed current dI is replaced by JdS and integrated over the total coil area S. Here J is the current density, and R is the inner radius of the iron yoke. The iron contribution is therefore seen in the second term of eq (2.8). If the complex field can be expanded into Taylor series, then B^* can be written as

$$B^* = \sum_{n=0}^{\infty} c_n z^n \tag{2.9}$$

where c_n are called the multipole coefficients. Here, c_n can be thought of as the summation of two terms $c_n = a_n + b_n$ due to the coil and the iron respectively. A typical iron contribution for a 6.6T dipole field is around 1.5T.

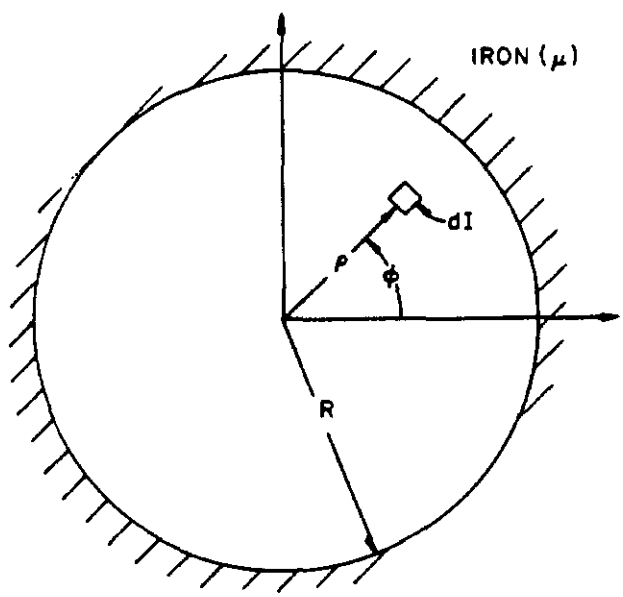

Figure 2.17: Current element within a circular iron boundary

Finite μ Effects

Here also the problem can be solved analytically by replacing the iron of permeability μ by an image current distribution. In polar coordinates, these multipole coefficients are given by

$$c_n = -\frac{\mu_o}{2\pi}\iint \frac{J}{\rho^n}\left[1 + \frac{\mu - 1}{\mu + 1}\frac{\rho^{2n}}{R^{2n}}\right] e^{in\phi} dS \tag{2.10}$$

where $dS = \rho d\rho d\phi$. The infinite μ results can be derived by letting $\mu \to \infty$. Again both the coil and the iron contributions are easily separated in eq (2.10).

2.6.2 Saturation Effects

Halbach [4] has formulated analytically the effects of saturation on multipole coefficients for a circulary shaped iron. Because of the relation between B and H in the iron, there is now an azimuthal field component $H_\phi(\phi)$ along the inner surface of the iron. The solution to such a problem is formulated by Schwarz's integral [9]. For a dipole structure with a symmetry with respect to the x-axis, the multipoles coefficients introduced due to the azimuthal field are given by

$$d_{(2m+1)} = -\frac{4i}{\pi R^{2m}}\int_o^{\frac{\pi}{2}} \cos(2m+1)\phi H_\phi d\phi \tag{2.11}$$

These coefficients are to be added to the infinite μ solution. Equation (2.11) is a cosine Fourier transform of the azimuthal field H_ϕ. As m increases the value of eq (2.11) becomes negligible for two reasons. First, the denominator R

increases in power of $2m$. Secondly, as $\cos(2m+1)\phi$ becomes more oscillatory and H_ϕ being a much slower varying function, the value of the integral from $0 \rightarrow \frac{\pi}{2}$ decreases . Therefore the dominant terms will be the first few terms. From what we observed numerically the change occurs mainly in sextupole and becomes less significant for decapole. Solution to eq (2.11) requires the knowldege of H_ϕ in a nonlinear iron which is not possible to obtain analytically. However such a distribution can be deduced from the numerical code POISSON.

2.6.3 The Sextupole due to Saturation

Our main concern at high fields ($\sim 8.8T$) is the effect of iron saturation. Such an effect, as mentioned earlier, will result in a change in multipole coefficients, mainly the sextupole. These changes can have serious effects on the field quality in the aperture and consequently on the particle stability. A convenient unit of measurement of the multipole coefficients is in $10^{-4}B_o$ units, that is, one part in 10,000 of the main dipole field. For a 6.6T dipole these coefficient changes were limited to about one unit at 1 in. Although saturation will result in a change in sextupole magnitude, the latter is not a quantitative measure of how much the iron is saturated. It is possible to have a very small sextupole at high field value, such as 8.8T, where the iron is highly saturated. A good measure of iron saturation is still the amplification factor defined as $\frac{B(\mu=finite)}{B(\mu=\infty)} - 1$.

In this design, our approach is not to avoid saturation, an impossible task

at high fields, but to control the manner in which the iron is saturated. For this, an understanding of how the iron saturates is necessary. The goal is to limit the sextupole change to less than two units for a dipole field ranging from 0T to 8.5T. This change in sextupole is very much dependent on the design requirements for the iron like the size and location of the support key, the size and location of the coolant channel and most importantly the inner shape and radius of the iron.

From eq (2.11) one can easily write the sextupole change as

$$d_3 = -\frac{4i}{\pi R^2}\int_0^{\frac{\pi}{2}} \cos(3\phi)H_\phi(\phi)d\phi \tag{2.12}$$

Two observations should be made here. Using the electromagnetic equivalence principle, the effect of iron saturation on the field in the aperture can be modeled by a single shell placed at the inner surface of the iron and having a current distribution given by $\vec{J} = \hat{n} \times \vec{H}$. This is pictured in Figure 2.18. It is obvious from eq. (2.12) that in order to avoid generation of sextupole fields, $H_\phi(\phi)$ should be proportional to $\cos(\phi)$. Such a result can also be predicted from the equivalence principle. The second observation concerns the form of integral (2.11). For a dipole with a circular iron geometry, one can convince oneself, by looking at Fig 2.19 that $H_\phi(\phi)$ is always either positive or negative as ϕ varies from 0 to $\frac{\pi}{2}$. Therefore the product function $\cos(3\phi)H_\phi(\phi)$ will have two zero crossings at $\phi = \frac{\pi}{6}, \frac{\pi}{2}$. Hence the integral (2.12) is the sum of two contributions, a positive one and a negative one. Depending on the distribution of H_ϕ, the two contributions can balance out, leading to a small

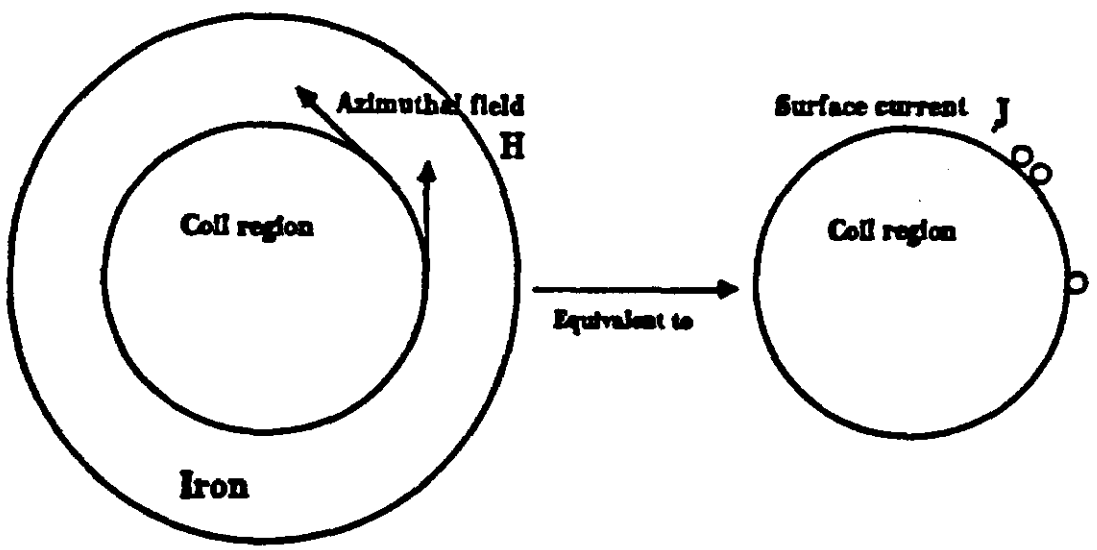

Figure 2.18: Equivalence of a Saturated Iron and a Surface Coil

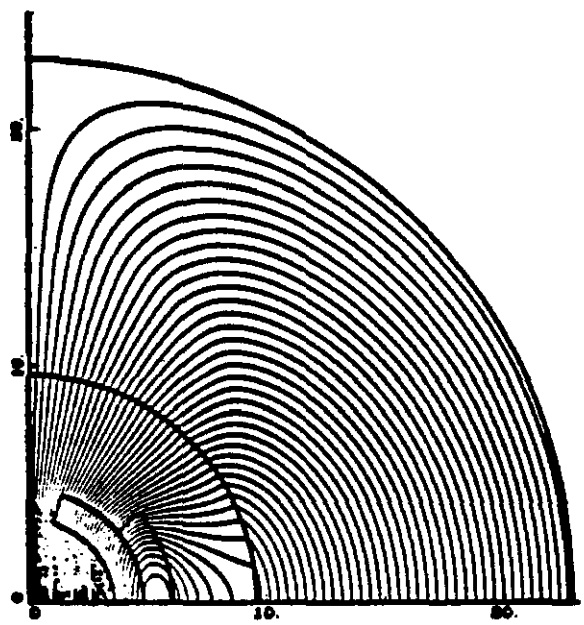

Figure 2.19: Field lines in a dipole magnet

sextupole value. These two contributions can be attributed to the top and medium plane saturation of the iron. We shall in the next sections investigate the effect of a different yoke design that can lead to a good balancing of these two contributions, in other words, a more even saturation of the inner surface.

2.6.4 Effects of Inner and Outer Diameters

By varying the inner radius of the iron, the way the iron saturate will change. It has been observed from the numerical simulations that given an inner radius, the sextupole variation versus dipole field can have one of two shapes. The first and most common shape is where the sextupole magnitude reaches a maximum positive value and then decreases. This behavior is attributed to the saturation of the top plane in the immediate vicinity of the coil causing the increase in sextupole. Saturation on either side of the coil will cause the sextupole magnitude to decrease. Tollestrup [15] had similar observations. It is important to note that such a behavior is very much dependent on the inner radius value. For a relatively large inner radius value, the notion of immediate vicinity becomes less significant. This results in a reduction in the peak value until a point is reached where any increase in inner radius will lead to the second shape of a monotically decreasing sextupole versus dipole field. Figure 2.20 illustrates this behavior for different inner radii. An increase in inner radius drives the sextupole more negatively and a decrease in inner radius drives it more positively. Therefore the negative contribution can be

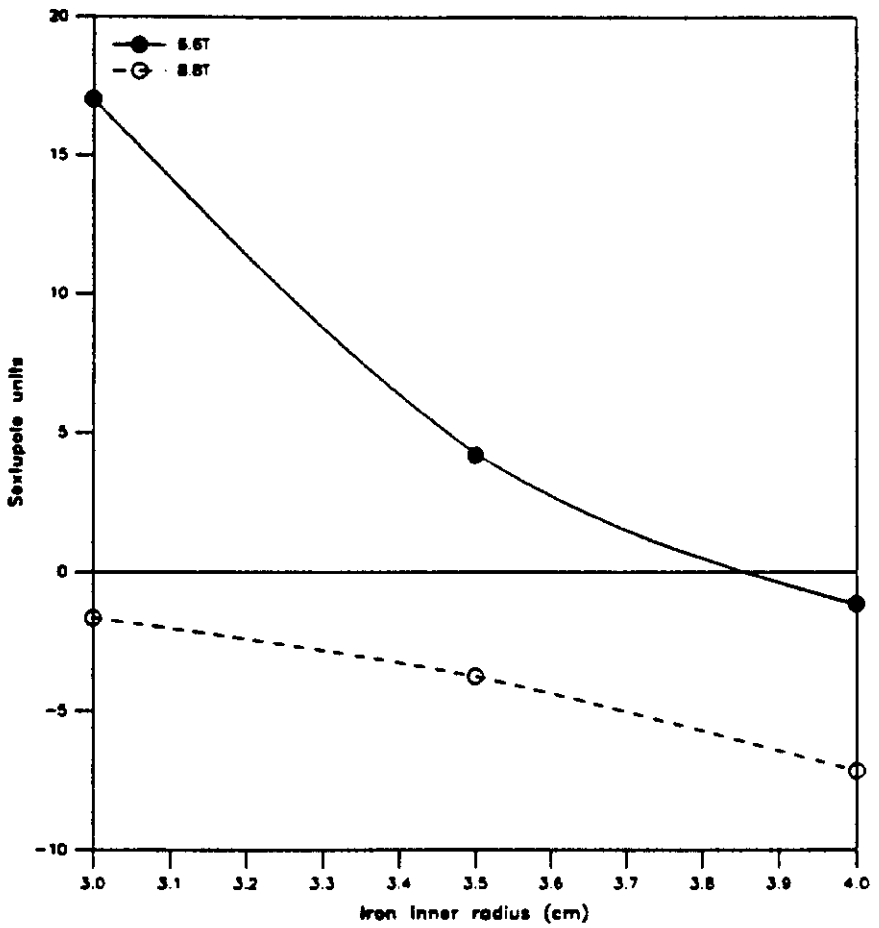

Figure 2.20: Sextupole variations for different inner radii of the yoke at two different excitations, J=4.44kA/turn and J=6.10kA/turn. Here, R_{coil}^{inner} = 1.5", R_{coil}^{outer} = 2.3", R_{iron}^{outer} = 8.66", Inner turns/Outer turns = 39/33

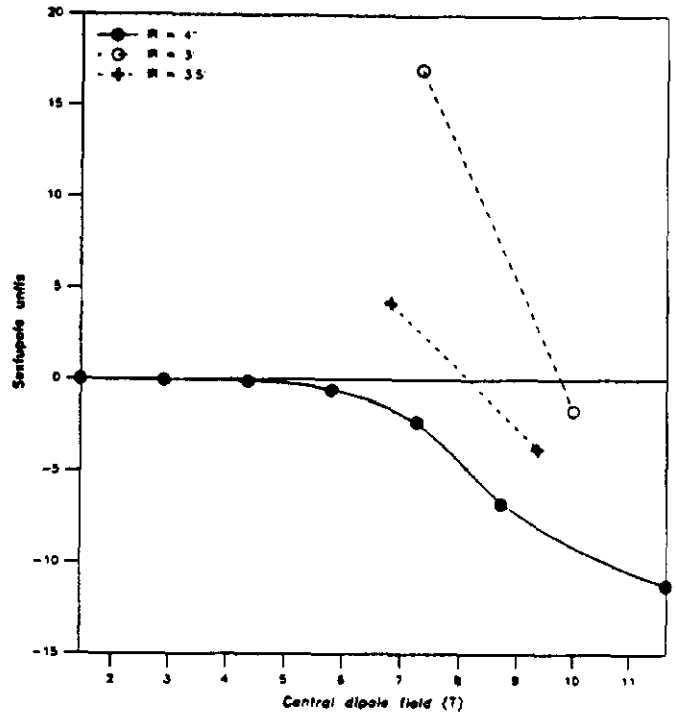

Figure 2.21: Change in sextupole vs dipole field at three different inner radii

attributed to the medium plane saturation and the positive contribution to the top pole saturation. It is interesting to note that for an inner radius of 4", the sextupole value at both low and high fields is negative. Further analysis shows this is true at all excitations. This is demonstrated in Fig 2.21. As the inner radius increases the zero crossing of the sextupole curve disappears and the curve becomes a monotically decreasing function. Based on these two types of behavior, we then have two options in our yoke design. Either select a radius such that the sextupole value over a given field range does not exceed a positive limit value or have a monotically decreasing value

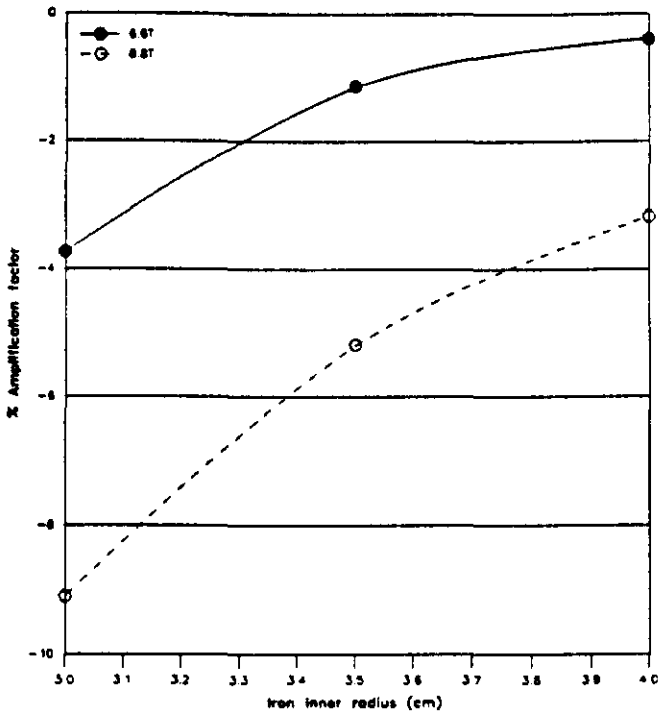

Figure 2.22: Amplification factor for different inner radius of the yoke

that will not reach a critical value at a desired high field point. From Figure 2.21, it is desirable to have an inner radius between 3.5" and 4".

Increasing the iron inner radius will decrease the iron saturation and therefore result in a better amplification factor. This is seen in Figure 2.22. The opposite is true if we decrease the inner radius. Although a 3.5"-4" inner radius range seems to limit the AF to less than 4% for 6.6T fields, this is not true at 8.8T. To have a better amplification factor at both fields, we need to reduce our inner radius range instead to

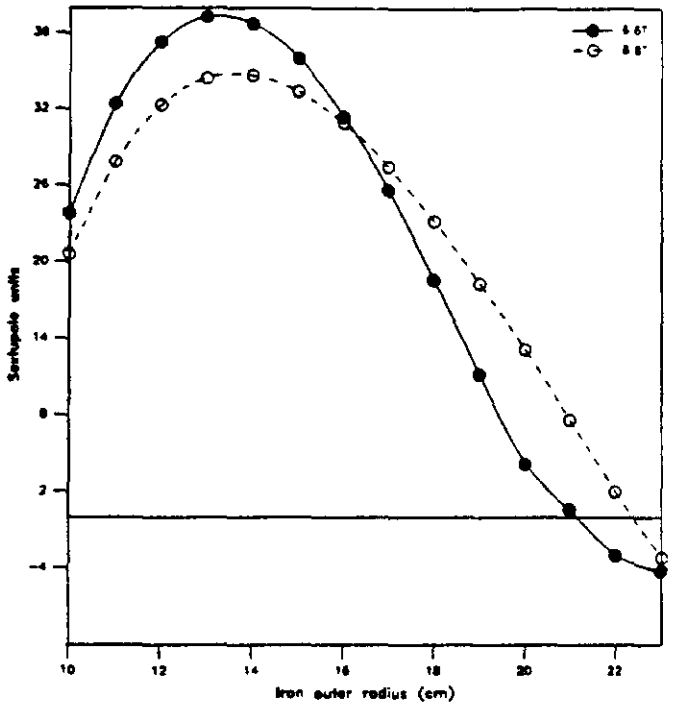

Figure 2.23: Sextupole change vs iron outer radius at two different excitations, J=4.36kA/turn and J=5.76kA/turn. Here, R_{iron}^{inner} = 3.54"

$$\boxed{3.7" < \text{Inner radius} < 4"}$$

The effect of the outer radius on sextupole is less predictable. As seen in Fig. 2.23 by reducing the thickness of the iron we will significantly increase the sextupole component. The effect of the outer radius on the dipole field quality is measured by the amplification factor. By increasing the thickness of the iron (more iron) a smaller amplification factor (stronger dipole field) is obtained up to a point beyond which any increase in radius will have little effect on the field and the outer radius act then like infinite. This behavior is

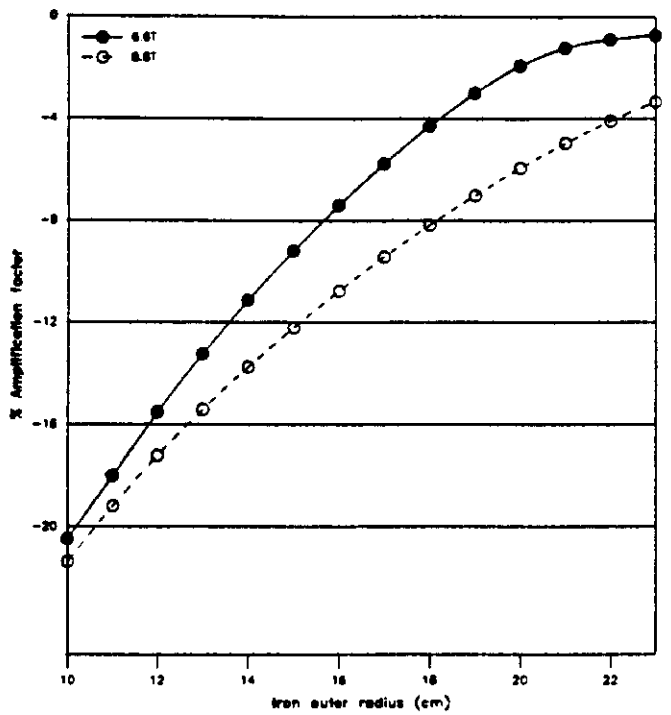

Figure 2.24: Amplification factor for different outer radii of the iron

illustrated in Figure 2.24 for both field regions 6.6T and 8.8T . The opposite is true if we reduce the thickness of the iron.

Another important parameter in the yoke design is the fringe field. Looking at the midplane cross section along the horizontal axis, it is possible to plot the field value in air in the immediate vicinity of the iron. Such a plot is shown in Fig 2.25. For an outer radius of 8.66", the fringe field is $\sim$ 1 Kgauss. Based on the three Figures 2.23, 2.24, 2.25 it is desired to have an outer radius greater than 8.66 in.

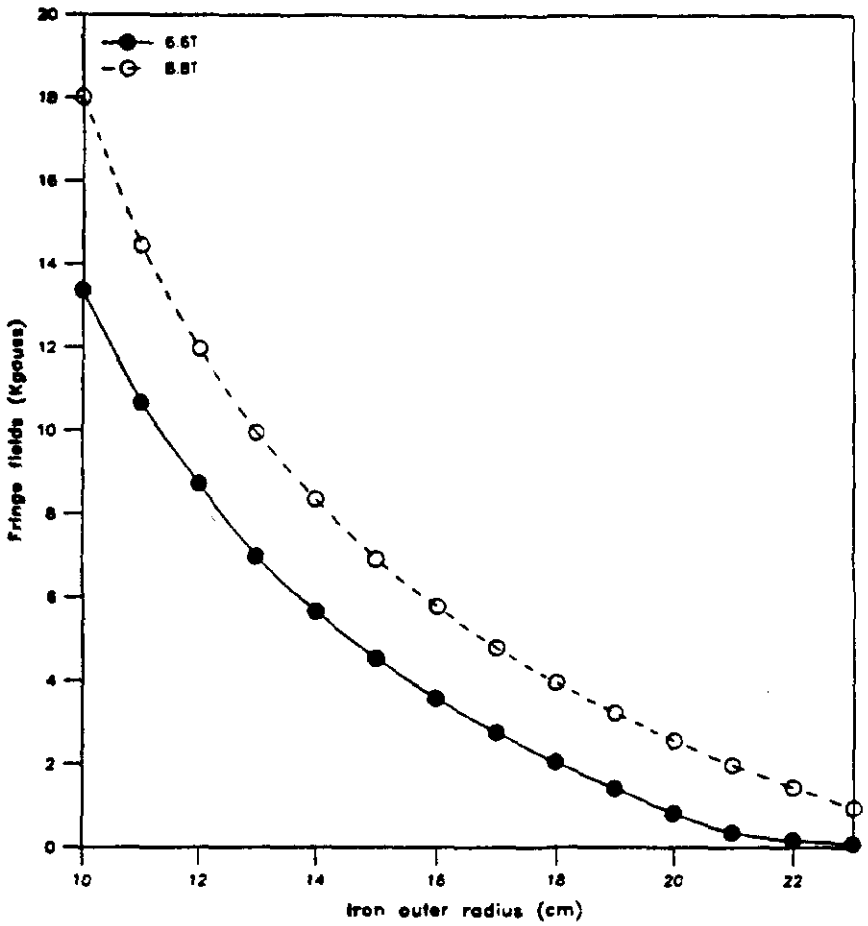

Figure 2.25: Fringe fields versus iron outer radius

Iron outer radius > 8.66 in

To summarize, the inner radius of the iron should be preferrably selected in the range of 3.7 – 4 in. The outer radius should have a minimum radius of 8.66". For this set of data the amplification factor is still in an acceptable range of less than 4%.

2.6.5 Elliptical Cross-Sections

Work in this area have considered elliptical cross section to reduce the iron saturation effect on multipoles [8]. However, to our knowledge, no magnet with an elliptical cross section has yet been built. The effects of an elliptical cross section on sextupole mainly and the amplification factor can be explained in the following manner. By bringing the pole in the vicinity of the coil closer, more saturation is induced locally relative to the midplane. This will further increase the positive contribution of integral 2.12 and lead to a higher peak in the sextupole distribution versus central dipole field. The surface being closer to the central gap will result in a bigger amplification factor. On the other hand, by pushing the pole away from the coil, less saturation in the immediate vicinity of the coil occurs, resulting in a reduction in the sextupole peak. This case will lead to a decrease in amplification factor. Illustrative examples are shown in Figures 2.26 and 2.27. Figure 2.26 shows the increase in the sextupole peak for a closer flat inner top pole. The effect of an outer top flat pole, seen in Fig 2.27, is less significant.

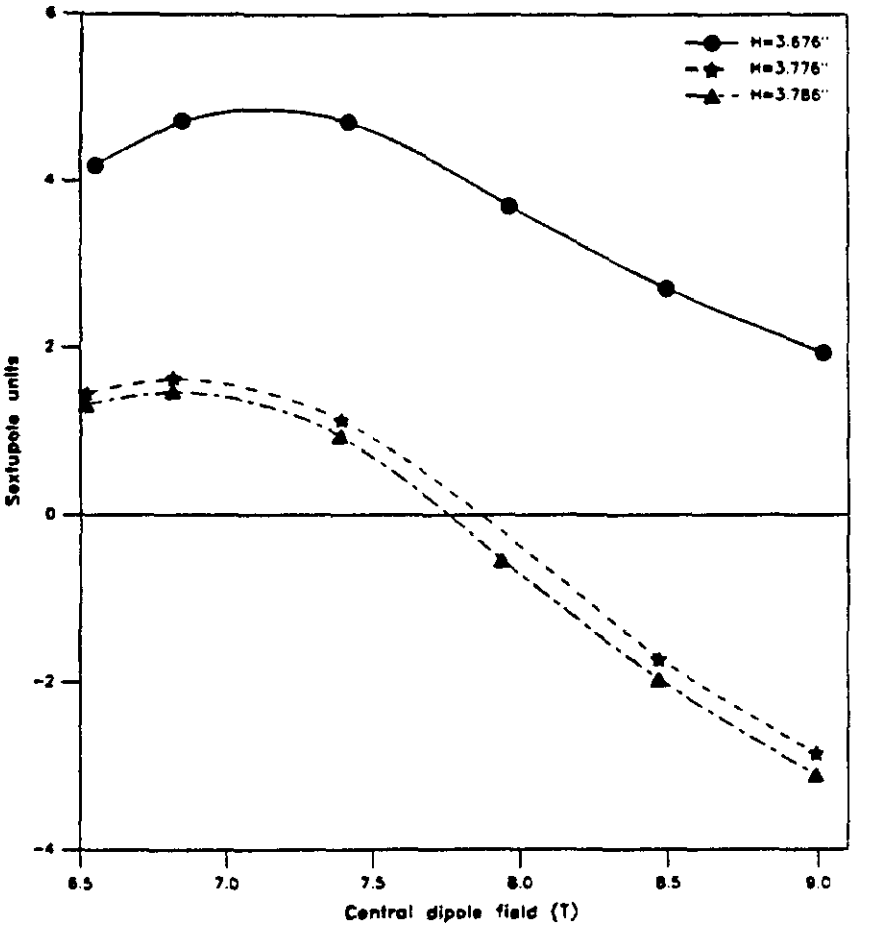

Figure 2.26: Effects of an inner flat top pole of height H on sextupole. Here, $R_{iron}^{inner} = 4$ in and $R_{iron}^{outer} = 8.66$ in

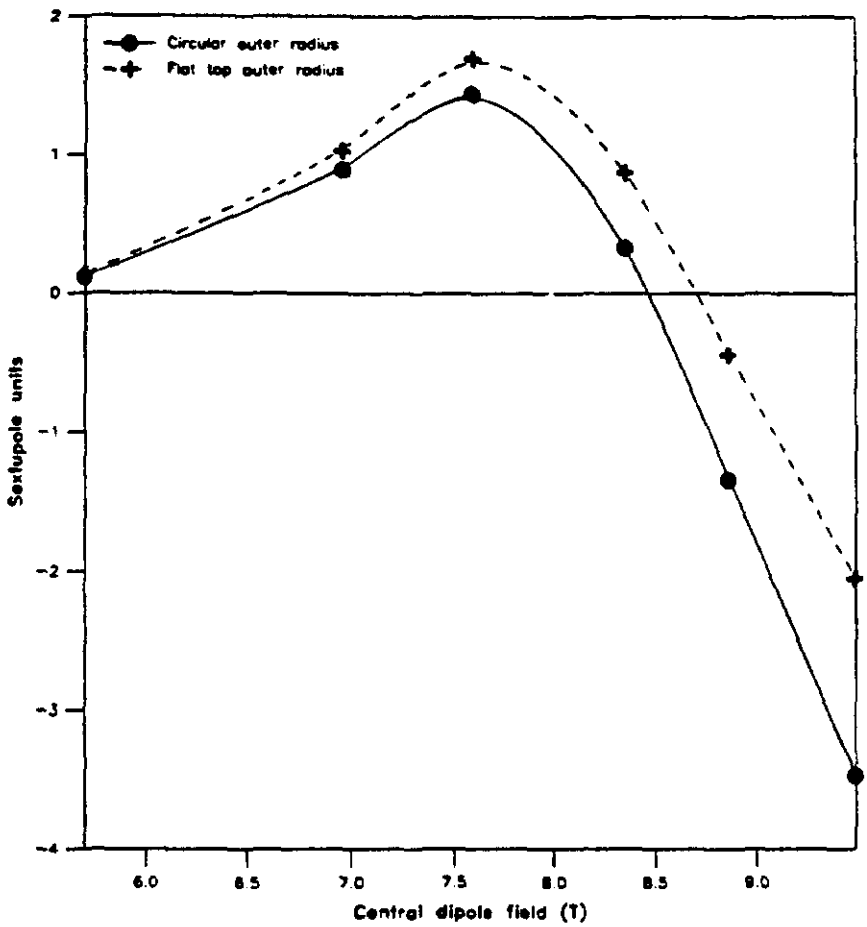

Figure 2.27: Effects of an outer flat top pole on sextupole. Here, R_{iron}^{inner} = 3.789", R_{iron}^{outer} = 9.055in, outer H = 6.505 in

The elliptical shape provide us with a strong tool to shift the sextupole distribution curve either up or down and therefore achieve an acceptable distribution curve. Other shapes can result in similar behavior but are relatively more complicated.

Elliptical inner iron surface

2.6.6 Effect of Iron Ellipticity on Conductor Placement

The code used to optimize the wedge angles for the infinite μ case assumes a circular inner surface. A modification of the inner surface will disturb the field distribution along its surface and result in a change of the poles coefficients. One would therefore need to correct for such changes by readjusting the wedge angles. For an elliptical surface the analytical solution with infinite μ may be possible if one uses conformal mappings. Such an analysis is not straightforward. Another alternative is to use POISSON to study the amount of correction needed in the wedge angles. It is found that an adjustment of $+0.78^o$ in the small wedge angle and of -2.87^o in the large wedge angle of the inner coil is enough to correct for the change in poles magnitudes due to the change of a circular inner surface to an elliptical surface.

2.6.7 Effects of Keys and Holes

Final assembly of the magnet requires the use of alignment keys and slots. The iron will also have in it passages for cooling pipes. It is therefore impor-

tant to know what effect these keys and holes will have on the field quality and sextupole coefficient.

The effect of such holes is negligible if properly located. Looking at the field lines inside the iron in Figure 2.18, we should expect almost no effect for a hole placed along the y-axis beyond $y = 19$ cm. A second smaller hole might be placed at $y = 14$ cm. Its effect on multipoles were found to be negligible.

Keys have more direct effect since they disrupt the inner surface shape. Such effects are described in Fig 2.28. . The effect of the keys is to introduce an extra 0.5-1 unit of sextupole depending on its location, whether at the vertical pole or horizontal pole .

2.6.8 Centered or Offset Coils

The calculations in section 2.1 have shown that an offset coil can lead to a better field uniformity along the mid-plane symmetry axis. However an offset coil is closer to the top pole than a centered one. Based on our previous discussions this should lead to an increase in sextupole. Figure 2.29 demonstrates this behavior by comparing the sextupole for both the centered and offset coils.

2.6.9 Suggested Design

The presently suggested yoke laminations is shown in Fig 2.30. The iron inner surface is slightly elliptical. The outer top surface is flat. The sextupole curve

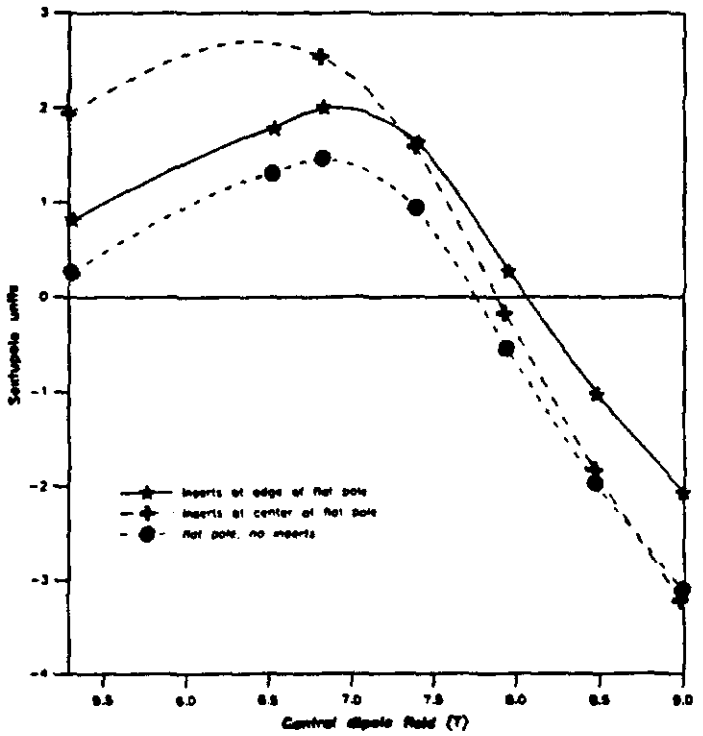

Figure 2.28: Effects of keyed inserts on sextupole at two different locations. Here, $R_{iron}^{inner} = 4$ in, $R_{iron}^{outer} = 8.66$ in

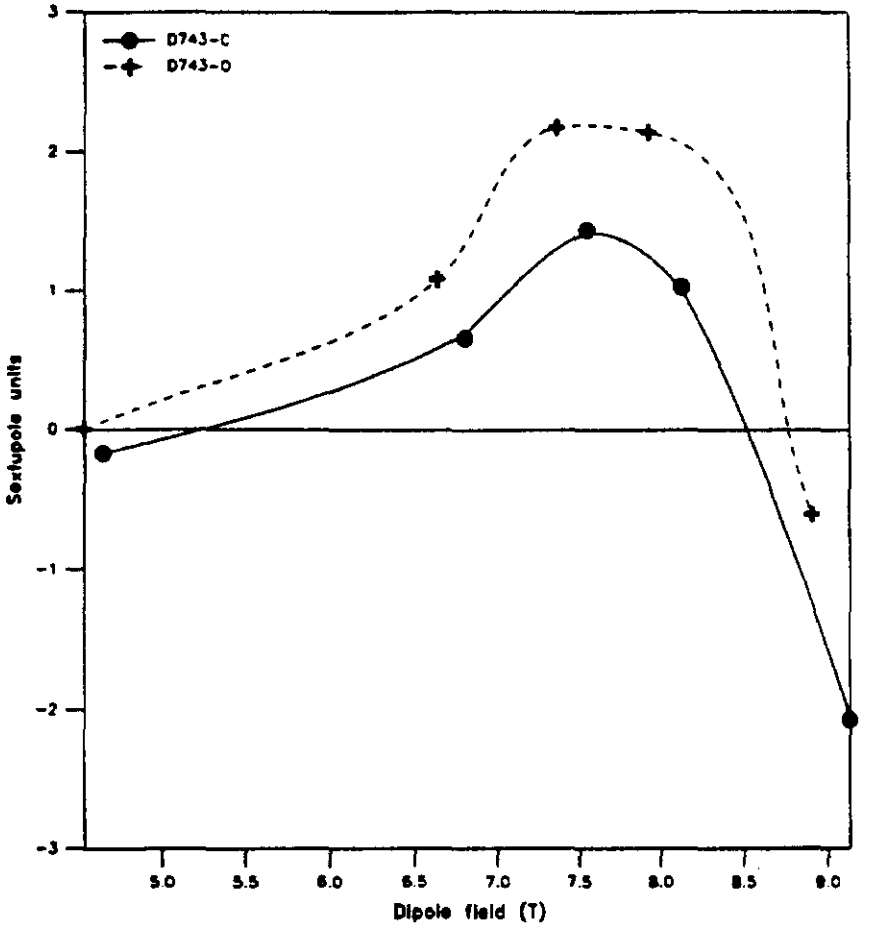

Figure 2.29: Effect of an offset coil on sextupole. Here, $R_{coil}^{inner} = 3.5in$, $R_{coil}^{outer} = 6in$, $R_{iron}^{inner} = 3.789in$, $R_{iron}^{outer} = 9.05$in, and offset=-0.414 in

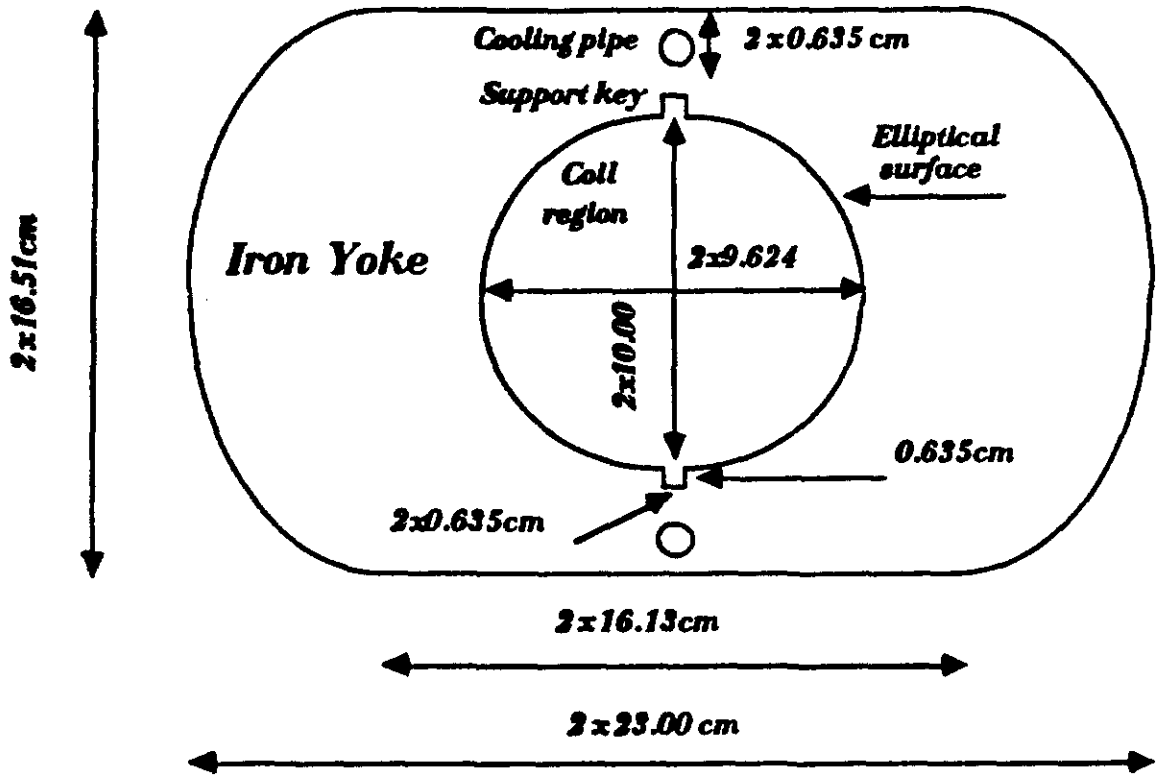

Figure 2.30: Yoke laminations

for such a configuration is shown in Fig 2.31. Also shown, for comparison, are the circular inner surface and the elliptical with a circular outer top pole.

The relatively high value of sextupole is considerably reduced by shaping the iron slightly elliptical. The result, shown by the elliptical iron symbol, is a reduction in peak sextupole from 3.3 units to 1.2 units. The amount of sextupole is now limited to $\sim$ 1 unit at 1 in for a field range up to 8.2T. The flat part in the outer radius has the effect of shifting the sextupole curve slightly up, leading to a more balanced distribution. This also has the advantage of cutting the amount of iron necessary and therefore reducing

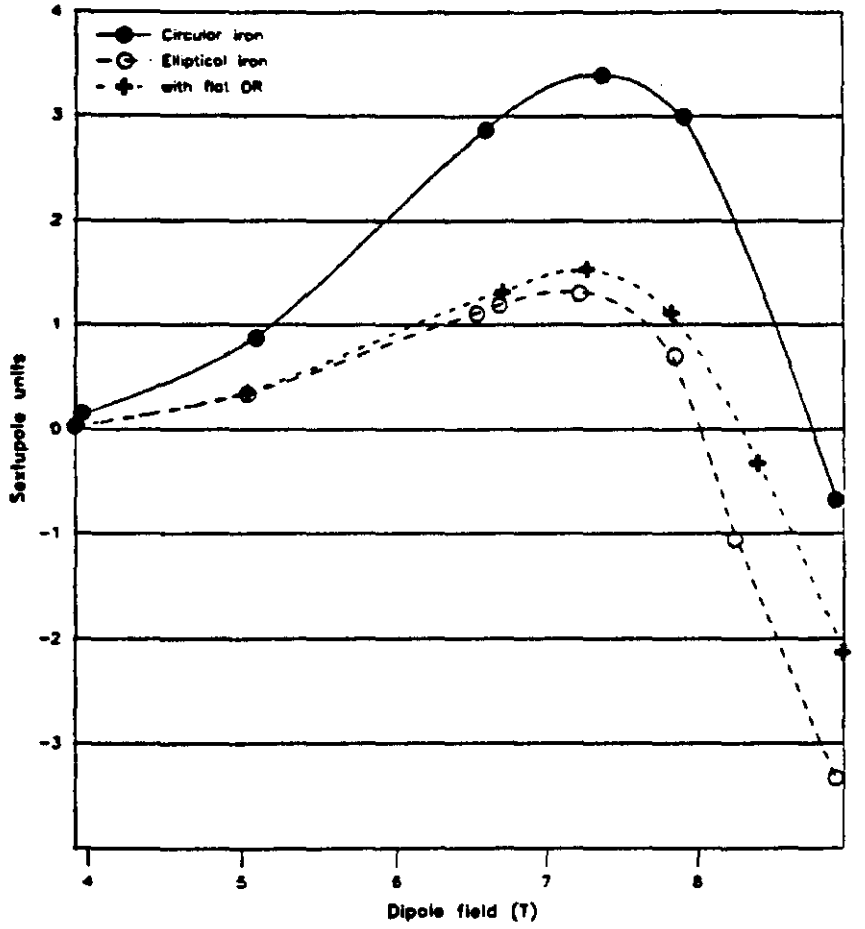

Figure 2.31: Sextupole change for a) the suggested elliptical yoke design b) similar design but with circular iron and c) the final elliptical design with a flat cut top pole

Central field (T)	6.6	8.8
Amplification factor (%)	0.49	2.98
Current per conductor (kA)	6.00	8.00
Saturation sextupole (units) at 1"	1.31	-2.13
Saturation decapole (units) at 1"	-0.132	-0.143
Fringe fields at mid-plane (Kgauss)	0.102	1.12
Fringe fields at top pole (Kgauss)	10^{-5}	10^{-4}
Inductance per conductor (mH/mt)	10.073	9.782

Table 2.11: Dipole magnet parameters

Major axis (cm)	9.624
Minor axis (cm)	10.00
Outer radius (cm)	23.00
Flat outer height (cm)	16.51
Cooling pipe radius (cm)	0.635
Support key dimensions (cm^2)	1.27x0.635

Table 2.12: Iron yoke dimensions

costs. Characteristics of this high field dipole magnet relevant to this section are shown in Tables 2.11 and 2.12.

Chapter 3

Mechanical Properties

3.1 Beam Tube Design

The high field dipole design incorporates a novel beam tube assembly which provides for the dissipation of the anticipated 4.2 K heat loads during fixed target operation. The assembly allows for a redesigned flow loop, which shortens the thermal path between the heat sink and the primary heat source. The new cooling scheme achieves more uniform coil temperatures through continuous single phase - two phase counterflow heat exchange.

The assembly design was driven by both thermal and structural considerations. Thermally, the system provides the means to maintain the coil temperature variations to less than 100 mK, using the existing Fermilab satellite refrigerators. Structurally, the assembly must withstand quench pressures of up to 20 atmospheres in the single phase flow passage, and 5 atmospheres in the two phase volume. The two phase passage need also be designed so that the resulting pressure drop is less than or equal to the two phase pressure

drop currently seen in the Tevatron magnet strings.

The beam tube assembly (Fig. 3.1) consists of two concentric, constant thickness stainless steel tubes. The inner tube, 0.09375 inches thick, separates beam vacuum from two phase helium flow, located in the annular space of the two tubes. This provides for a beam space 1.6 inches high, and 2.2 inches wide. The two phase helium flows through an annulus 0.0625 inches wide at the midplane, and 0.5 inches wide at the poles. The outer tube, 0.0625 inches thick, separates the single phase flow in the collared coil region from the two phase return. The single phase helium then flows through a 0.0625 inch gap concentric to the inside diameter of the coil. A thin (0.003 inch) copper plating is applied to the exterior of the $1\phi/2\phi$ tube, to moderate any azimuthal temperature distribution in the wall. Mechanically, the inner tube is located with respect to the $1\phi/2\phi$ tube by axially intermittent spacers. These spacers also integrate the tubes structurally by distributing loads between the two. The $1\phi/2\phi$ tube (and thus the whole assembly) is located by contact with the collar packs in the pole region. This interference serves to limit the deflection of the tubes when pressurized, and maintain material stresses within acceptable limits.

3.1.1 Thermal Considerations

Thermally the beam tube provides the means to dissipate the higher heat loads of the high field dipole while maintaining the coil temperature variation to less than 100 mK. Since the quantity of helium refrigeration available to

Helium Flow	25 g/s @ 4.2 K
2ϕ Exit Liquid Quality	20 %
2ϕ Isothermal Heat Sink	474 W/string
-to Magnets	351 W/string
Magnet 4.2 K Heat Load	16 W/magnet
-Collared coil region	12 W
-Yoke region	4 W

Table 3.1: Thermal Design Considerations

each magnet string is fixed, and the temperature variation specification is the same as that imposed on the Tevatron system, the higher heat load of the high field dipole must be dissipated by a more efficient heat exchanger. The thermal design uses a flow loop similar to that existing in the Tevatron, but places the two phase return closer to the magnet coil, where the primary heat load is located.

The pertinent design for a high field dipole magnet string attached to a refrigerator while operating in fixed target mode are obtained from section 4.2 and are listed in Table 3.1. A typical string is assumed to consist of 16 magnets (4 groups of 3 dipoles, 1 quadropole).

Using a flow loop identical to the Tevatron, an energy balance calculation was performed to evaluate the temperature rise along a four magnet group (Figure 3.2). In this flow loop, the helium 1ϕ flow is split into two paths at each magnet. The inner flow surrounds the coil and advects the coil heat load from the magnet. The outer flow heat exchanges with the two phase return.

$\dot{m}_c$	ΔT_1	ΔT_2	ΔT_3	ΔT_4	ΔT_{gr}
25. g/s	0.16 K	0.14 K	0.13 K	0.11 K	0.54 K
20.	0.19	0.17	0.16	0.15	0.50
15.	0.25	0.23	0.21	0.20	0.50
10.	0.36	0.32	0.31	0.31	0.54

Table 3.2: Tevatron-style Energy Balance results

The single phase flows are manifolded at the end of each magnet, the continue to the next magnet after mixing. The analysis assumes no losses, complete mixing of the single phase flows between each magnet, and the single phase flow which exchanges with the two phase exits the heat exchanger at 4.2 K. The coil flow does not heat exchange with the two phase in the magnet. The single phase mass flow split was varied.

The model predicts (Table 3.2, Figure 3.3) that, for all coil flow rates, the temperature rise in any single magnet is greater than the design goal of 0.1 K. Figure 3.3 shows the coil flow temperature rise, while Table 3.2 lists the temperature rise across each magnet, and the total temperature rise along the four magnet group. The abrupt drop in temperature between magnets is due to the mixing of the coil flow with the outer, cooled flow.

Although the decreasing coil mass flow rates appear to bring the downstream magnets to a steady condition sooner, the individual temperature rise is still unacceptable. Clearly, the use of a Tevatron style flow loop to advect the heat from each magnet and cool the flows between magnets is not

$\dot{m}_c$	ΔT_1	ΔT_2	ΔT_3	ΔT_4	ΔT_{gr}
20. g/s	0.03 K	-0.06 K	-0.05 K	-0.05 K	0.05 K
15.	0.03	-0.06	-0.06	-0.06	0.06
10.	0.04	-0.05	-0.07	-0.07	0.07

Table 3.3: New Flow Loop Energy Balance Results (Stainless Steel)

practical for the higher heat loads proposed with the high field dipole.

The beam tube assembly allows an alternative flow loop (Figure 3.4) to be used. Three single phase flow paths exist through each magnet in this system. The inner flow, around the coil, collects the coil heat load while heat exchanging with the two phase return. The two outer flow paths collect the heat load from the outer regions of the collar and the yoke. These are recooled by mixing with the coil flow in the interconnect regions. The relocation of the two phase flow path places the heat sink closer to the primary heat source, the magnet coil.

The new flow system has been modeled in an identical manner to the old flow loop, except that a thermal resistance, representing the shell between the single phase and two phase flows, has been included (Figure 3.5). Results from this model (Table 3.3, Figure 3.6) show acceptable temperature differentials across the magnet group for coil flows greater than 10 g/s. The decrease in coil flow temperature along the magnet length is due to the heat exchange with the two phase return. The temperature rise at the ends of magnets 2 through 4 is due to the adiabatic mixing of cooled coil flow with

$\dot{m}_c$	ΔT_1	ΔT_2	ΔT_3	ΔT_4	ΔT_{gr}
20. g/s	0.12 K	0.08 K	0.05 K	0.04 K	0.34 K
15.	0.16	0.11	0.07	0.04	0.35
10.	0.22	0.15	0.11	0.07	0.37

Table 3.4: New Flow Loop Energy Balance Results (Stainless Steel with 0.003" Kapton)

the helium flow which has collected the outer coil and yoke AC losses.

It should be noted that the model is sensitive to the thermal resistance value used to model the single phase / two phase tube. The Tevatron dipole magnets incorporate a 0.006" thick ground wrap on kapton on the beam tube, to prevent coil to tube shorts. The addition of the equivalent of a 3 mil layer of kapton to the wall thermal resistance raises the $1\phi/2\phi$ wall thermal resistance by a factor of 20, and results in unacceptably high temperature rises (Figure 3.7, Table 3.4). The predicted effect of the kapton on the performance of the heat exchanger resulted in the removal of the ground wrap kapton covering the $1\phi/2\phi$ tube. In the high field dipole design, the base wrap of several mils of kapton on the conductor is used as the electrical insulator between the coil and metal tube. The absence of a ground wrap layer on the $1\phi/2\phi$ tube results in no degradation of the $1\phi/2\phi$ heat exchange.

A final thermal consideration is the azimuthal temperature profile. Near the return end of the two phase flow path, only 20 % or less of the 2ϕ helium is in liquid form. To moderate any temperature distribution which may arise,

a 3 mil copper plating has been added to the outside of the $1\phi/2\phi$ tube. Since the thermal conductivity of copper is over three orders of magnitude higher than that of stainless steel at cryogenic temperatures, the addition of the thin sheet reduces the thermal resistance of the $1\phi/2\phi$ tube by greater than 60 in the azimuthal direction. The copper plating is interrupted, either helically or circumferentially, every few inches to minimize eddy current effects induced by the collapse of the magnetic field during a quench.

3.1.2 Structural Considerations

With the relocation of the two phase helium return flow to the beam tube area for thermal reasons, the design of the beam tube assembly was constrained by two structural considerations. First, within the geometric limits of the collared coil assembly and the desired beam area, a two phase area must be provided so that the pressure drop is less than or equal to that in the present Tevatron flow loop. Secondly, the structure must be able to withstand the quench pressures of 20 atmospheres in the single phase region and 5 atmospheres in the two phase region.

The pressure drop in a two phase helium system can be scaled as proportional to

$$\Delta P \propto (WP, \dot{m}^2, A^{-3}) \tag{3.1}$$

where m is the mass flow rate, A is the cross sectional area, and WP is the wetted perimeter. Since the mass flow rates of the two systems are equal,

1ϕ Area	0.51 in^2 (2.82 in^2)
Wetted Perimeter	16.64 in (44.32 in)
Wetted Perimeter to 2ϕ	8.07 in (12.47 in)
2ϕ Area	1.50 in^2 (1.89 in^2)
Wetted Perimeter	15.36 in (18.07 in)

Table 3.5: Beam Tube Assembly Cross Section Flow Areas

the ratio of the two is simply

$$\frac{\Delta P_{HFD}}{\Delta P_{TEV}} = \frac{WP_{HFD}}{WP_{TEV}} \frac{A^3_{Tev}}{A^3_{HFD}} \tag{3.2}$$

Table 3.5 lists the flow areas and wetted perimeters for the beam tube assembly, with Tevatron values included in parantheses for comparison. The single phase values are included for completeness.

Substituting from the table into the pressure scaling relationship,

$$\frac{\Delta P_{HFD}}{\Delta P_{Tev}} = 0.85 \tag{3.3}$$

the beam tube assembly assembly has a two phase pressure drop lower than the present Tevatron flow system.

The final structural criteria for the beam tube assembly is the ability to withstand quenches pressures. Tevatron experience has shown quench pressures of up to 20 atmoshpers are possible in the single phase passage, and up to 5 atmospheres in the two phase. A two dimensional finite element analysis of the beam tube assembly shows that the assembly safely withstands the quench conditions. Maximum Von Mises stresses are less than 11ksi, well

below the 30ksi yield stress of stainless steel.

3.2 Collar Design

The collar design of the high field dipole follows recent cold iron magnet conventions closely. The collars (Fig. 3.6) are aluminum (7075-T6), 3.724" OD, with the front and back collars joined by semi-perfs. The locking mechanism is provided by 8 keys, located symmetrically two per quadrant. Unlike other designs, the high field dipole collars have a stainless steel skin. The skin, 0.0625" thick, limits the subatmospheric helium volume, but is not a structural member.

Collar design is driven by several factors, the most important of which is the retention of coil preload after removal from the collaring press and during magnet cooldown. The collar size is limited by the impact on the iron volume which increases geometrically as the collar outside radius increases. In the design of this collar, effects which were focused on were the effect of collar width of preload deflection, and the sizing and quantity of keys for limiting the preload stresses in the collar to the elastic range.

3.2.1 Effect of Collar Width

To determine the sensitivity of collar preload deflection as function of coil outside radius, an idealized collar was created. The model (Fig. 3.7) simulates a hoop, with inner dimension specified by the coil geometry and outer

dimension variable. By symmetry, only a quarter of the collar need by modeled. Preload forces, equivalent to inner coil preload of 20ksi and outer-coil preload of 10ksi, were applied directly to the collar as nodal forces. Results (Fig. 3.8) show the collars becoming more stiff for increasing radii, as expected. However, the sensitivity of the deflection decreases markedly as the outer radius increases beyond 3.5 inches.

Since the collar size directly effects the yoke geometry, as small a radii as possible is needed. For the high field dipole, a collar radius of 3.724 inches was selected. With a 0.065 skin, this places the iron inner radius at 3.789".

3.2.2 Keying Mechanisms

With the collar dimensions sized, a keying mechanism needs to be designed to make the actual collar approach the ideal case as nearly as possible. The keys provide the locking mechanism which prevents the collars from springing apart when the collaring process is over. Furthermore, they must be sized so that the deflection of the collared coil is minimized, while the maximum bending stresses in the collar remain below the elastic limit of the collar material.

The 8 keys of the high field dipole collar (Fig. 3.9) are 0.2 inches wide, with the 4 keys nearest the horizontal midplane 0.375 inches deep, with the remaining 4 keys are 0.25 inches deep. The keys are all of stainless steel.

The finite element model used for the analysis consists of "front" and "back" collars, (Fig. 3.10) which by symmetry provide a complete model

of the collar lamination packs. This method was originally described by Chapman and Wands. Preload forces associated with 20ksi and 10ksi inner and outer preloads were applied directly to the nodes on inner surface of the coil cavity in the collars. Key elements were created, of various size and number, to simulate the keying schemes of interest.

First, as is the SSC collar, a single key per quad was modeled. Results (Fig. 3.11) show the key limiting the vertical deflection of the collar to 12 mils. However, a local maximum Von Mises stress of 95.7ksi is predicted in the collar at the midpoint at the key way, 37% larger than the elastic limit of the aluminum.

To distribute the stresses more evenly, a second key was added to each quadrant, both keys being 0.25" deep. The vertical deflection is reduced to 11.1 mil, and the maximum Von Mises collar stress lowered to 77.6ksi, at the midpoint the upper key. The midplane key is hidden, or shielded by the action of the upper key. Increasing the depth of the midplane key to 0.375 inches reduces (Fig. 3.12) the vertical deflection to 10.6mil, and reduces the maximum stress to 70.2ksi by distributing the locking action of the keys more uniformly.

As a proof of principle, a 3rd key per quadrant was added, 0.125" deep, above the other two. The deflection decreased slightly, to 10.4 mil, while the maximum stress drops to 63.9ksi. However due to difficulties with the assembly of collars and keys, the final design relies on two keys, of depth 0.25

and 0.375 inches, to limit the collar preload deflection while distributing the loads and maintaining the maximum collar stress to 70ksi.

3.3 Yoke Design

The Phase III dipole is a cold iron magnet. Cold iron has several advantages over its warm iron counterparts. First, it provides the maximum field enhancement due to the close proximity of the iron and collared coil assembly. Second, there are no forces imposed on the suspension system resulting from the coil and iron centerlines not being coincident. The disadvantage of cold iron lies principally in the fact that it represents a significant load on the refrigeration system during cooldown.

The iron yoke employed in this design is vertically split which means that the collar preload stress is restrained by the iron laminations. The Lorentz forces are resisted by the cold mass containment skin. The advantage to a vertically split yoke is that a parting plane gap represents no perturbation to the magnetic field.

Cooling is not by direct flooding of the iron with liquid, but rather through conduction via two 1/2 inch diameter tubes in contact with the laminations near the top and bottom of the yoke stack. This scheme will require longer cooldown times, but serves to greatly reduce 1.8K liquid volume. Even a tightly packed yoke stack has approximately a 3% void fraction which would represent a liquid inventory of 27.6 liters. Two 1/2 inch tubes represent 1.7

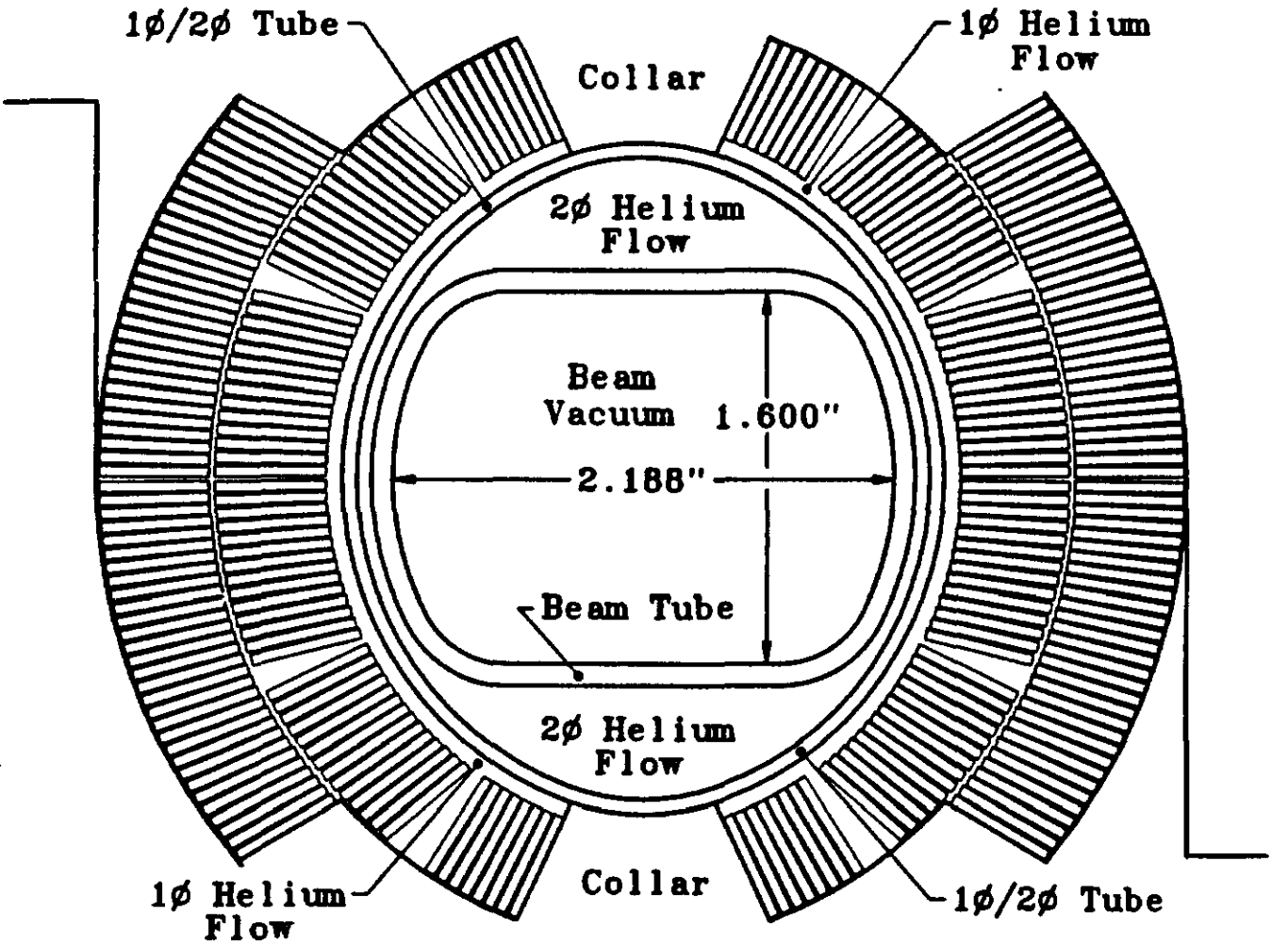

Figure 3.1: Beam Tube Design

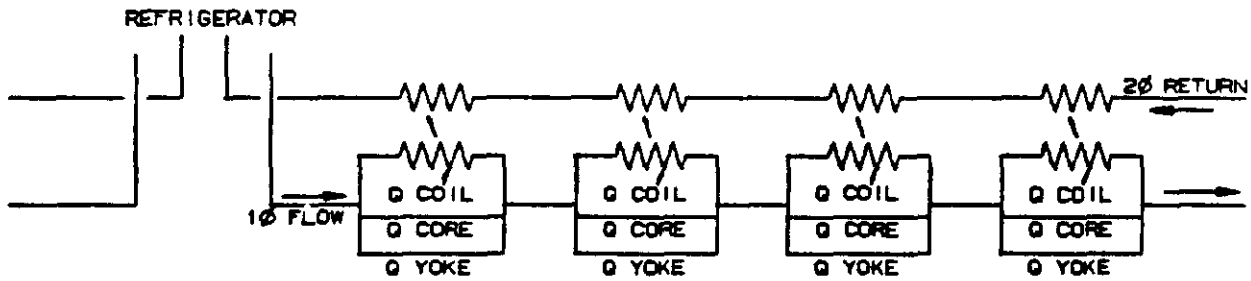

Figure 3.2: Four magnet group

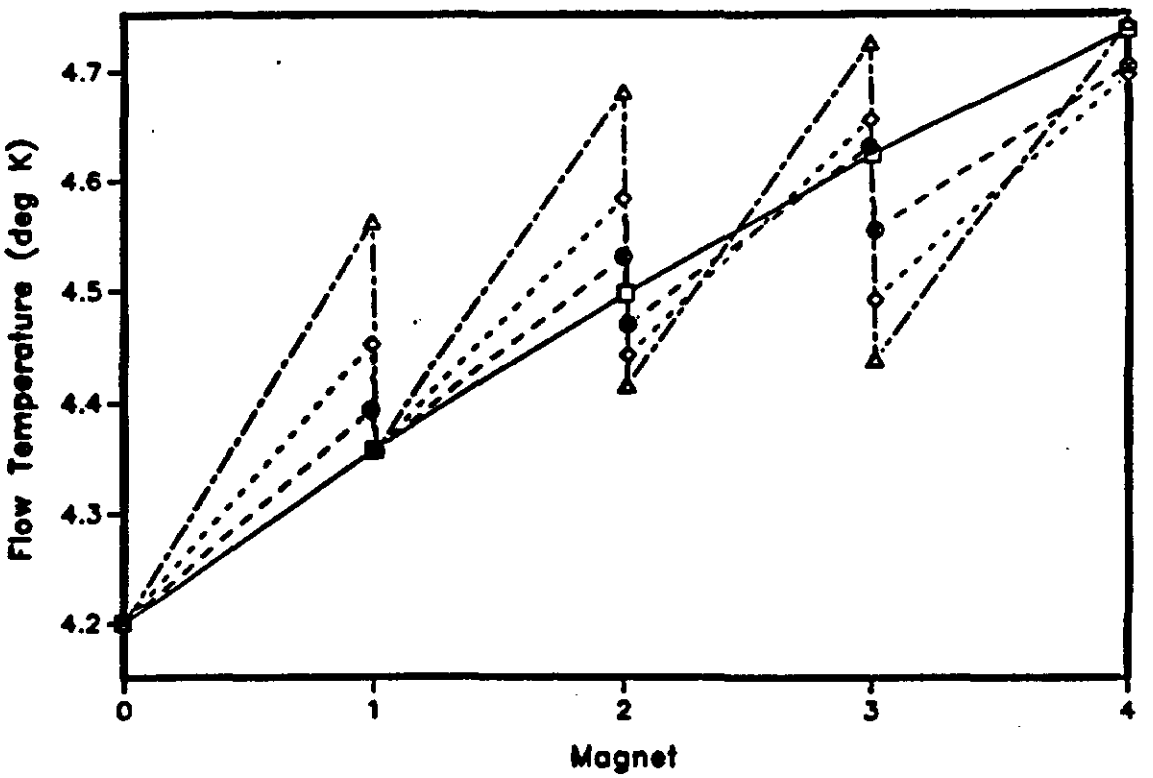

Figure 3.3: Helium Coil Flow Temperature Rise

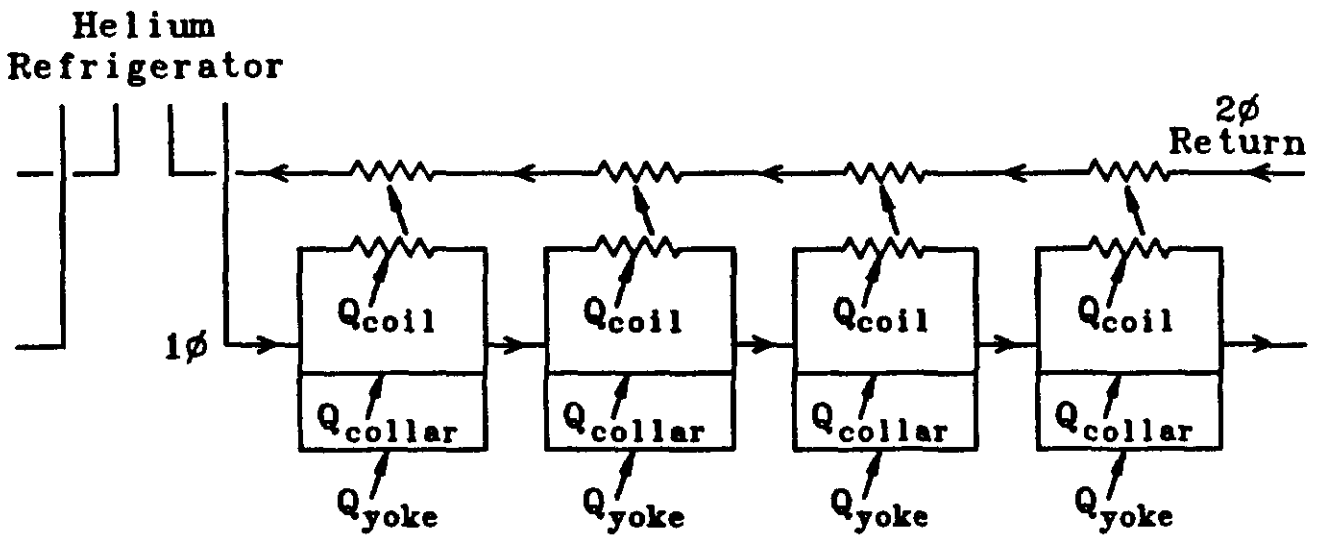

Figure 3.4: Beam tube Assembly

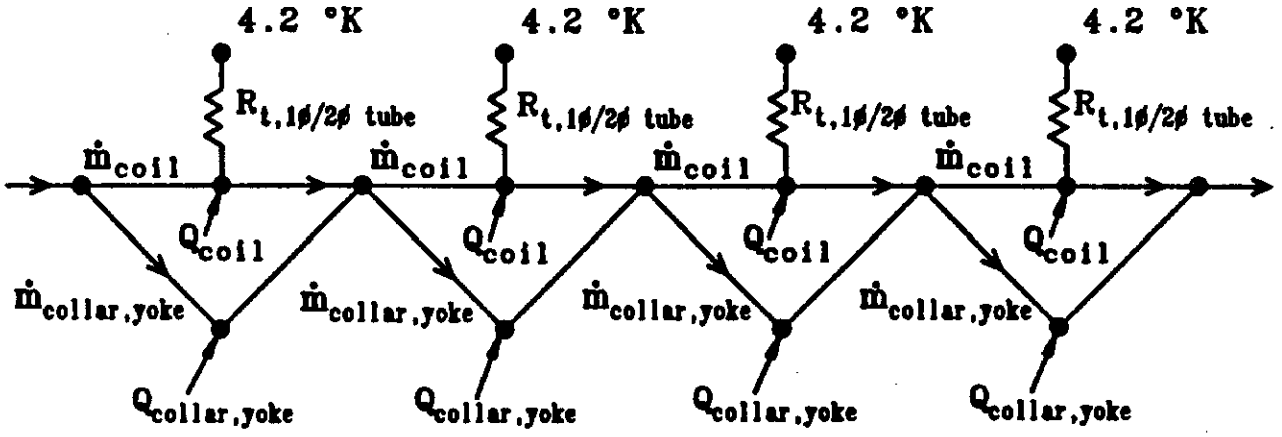

Figure 3.5: Single Phase and Two Phase Flows

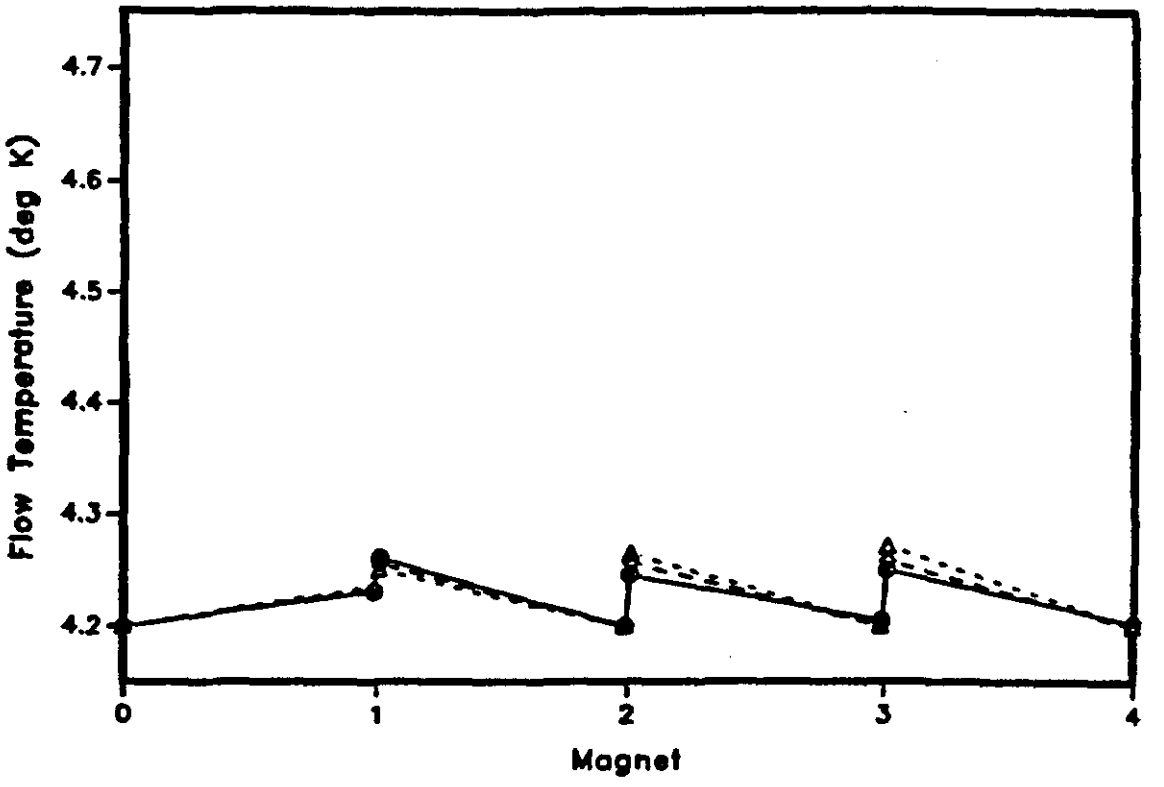

Figure 3.6: Coil Helium Flow Temperature Rise

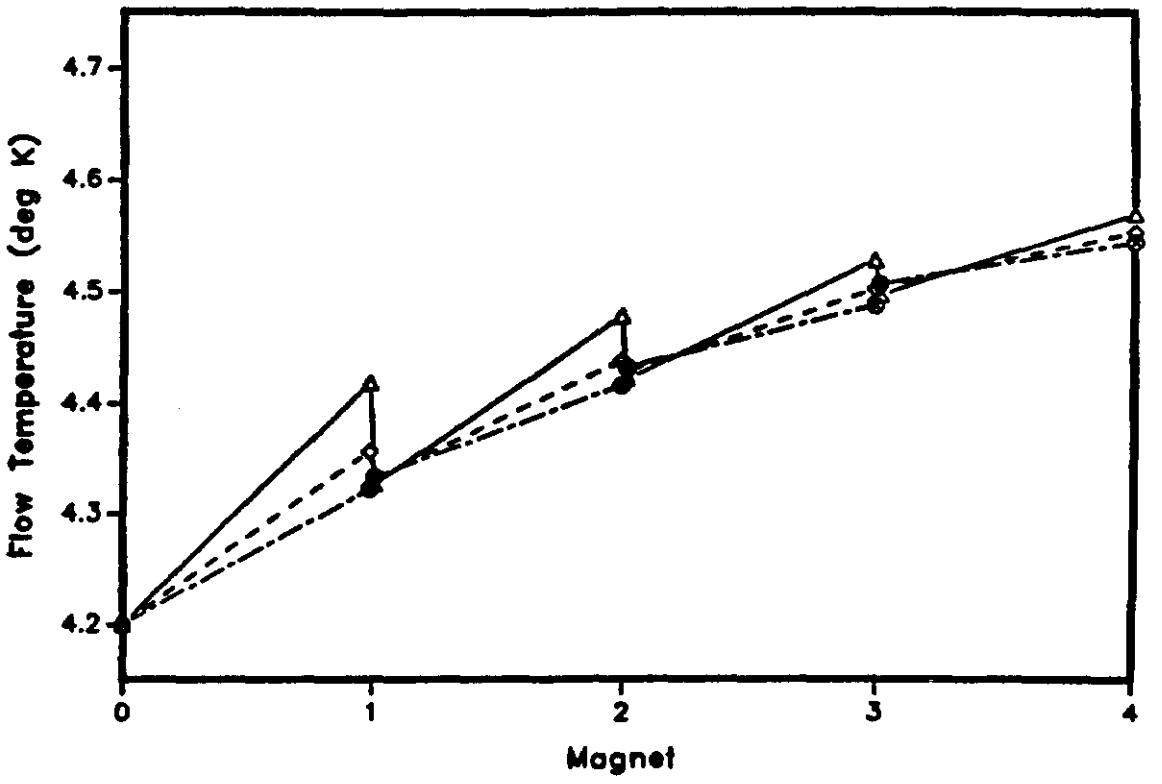

Figure 3.7: Coil Helium Flow Temperature Rise

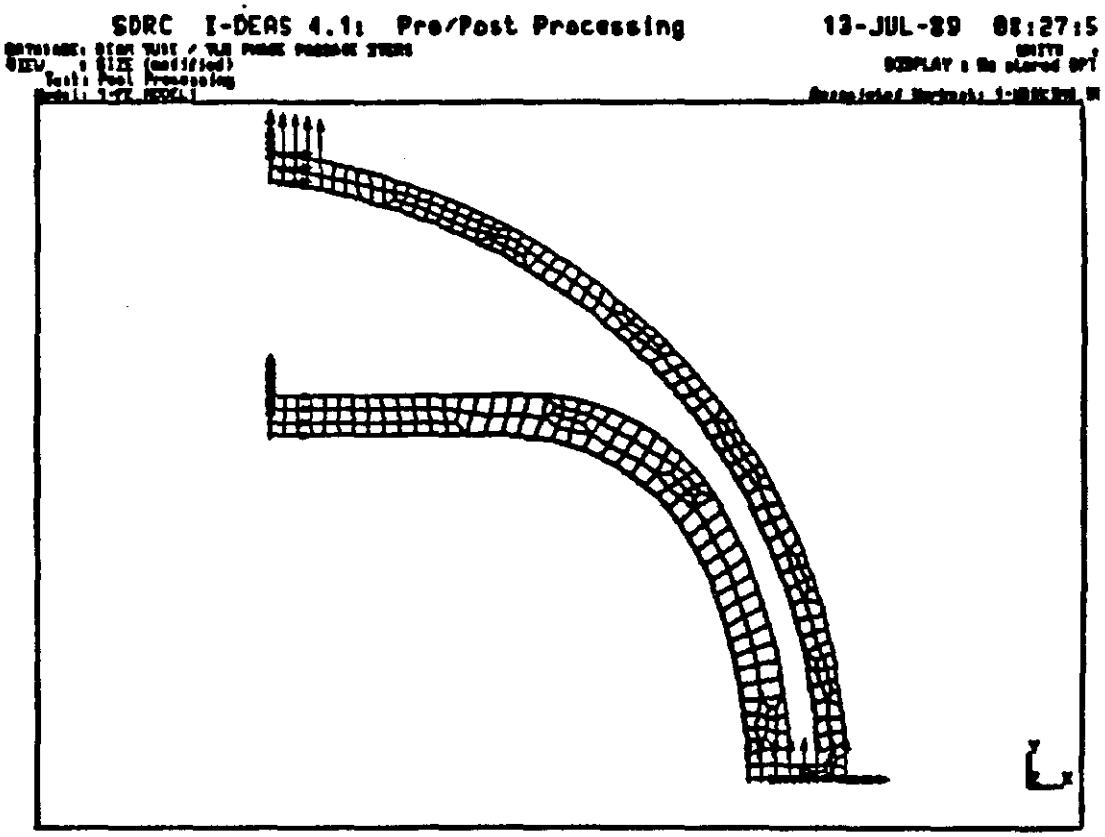

Figure 3.8: Beam Tube / Two Phase Passage

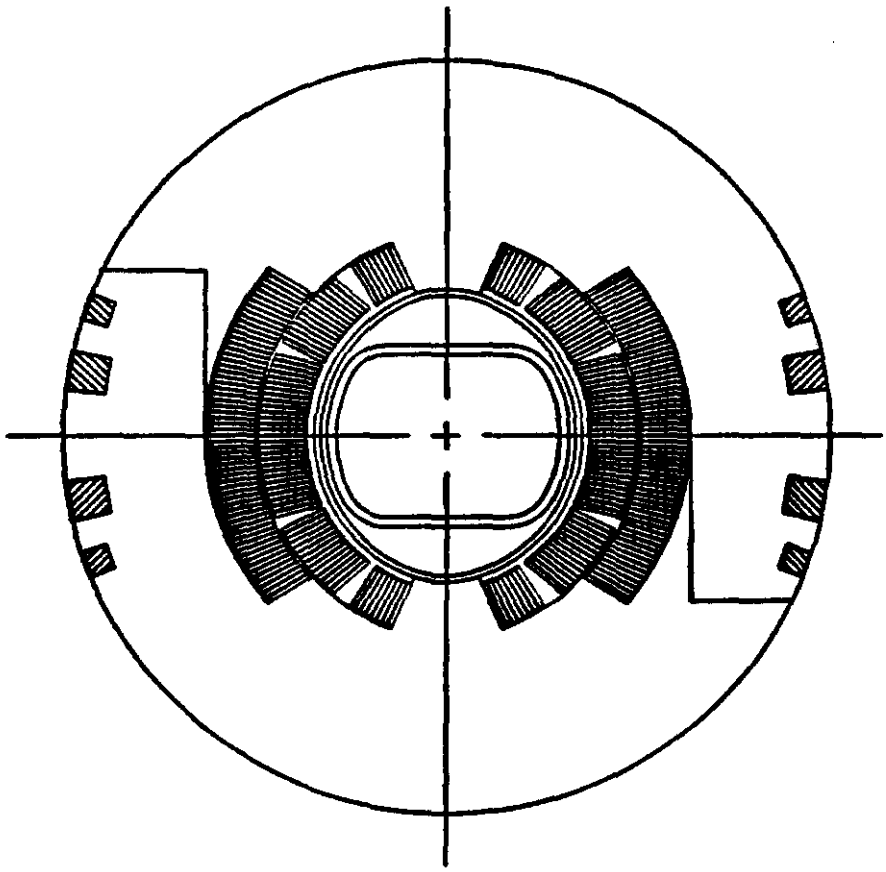

Figure 3.9: High field Dipole

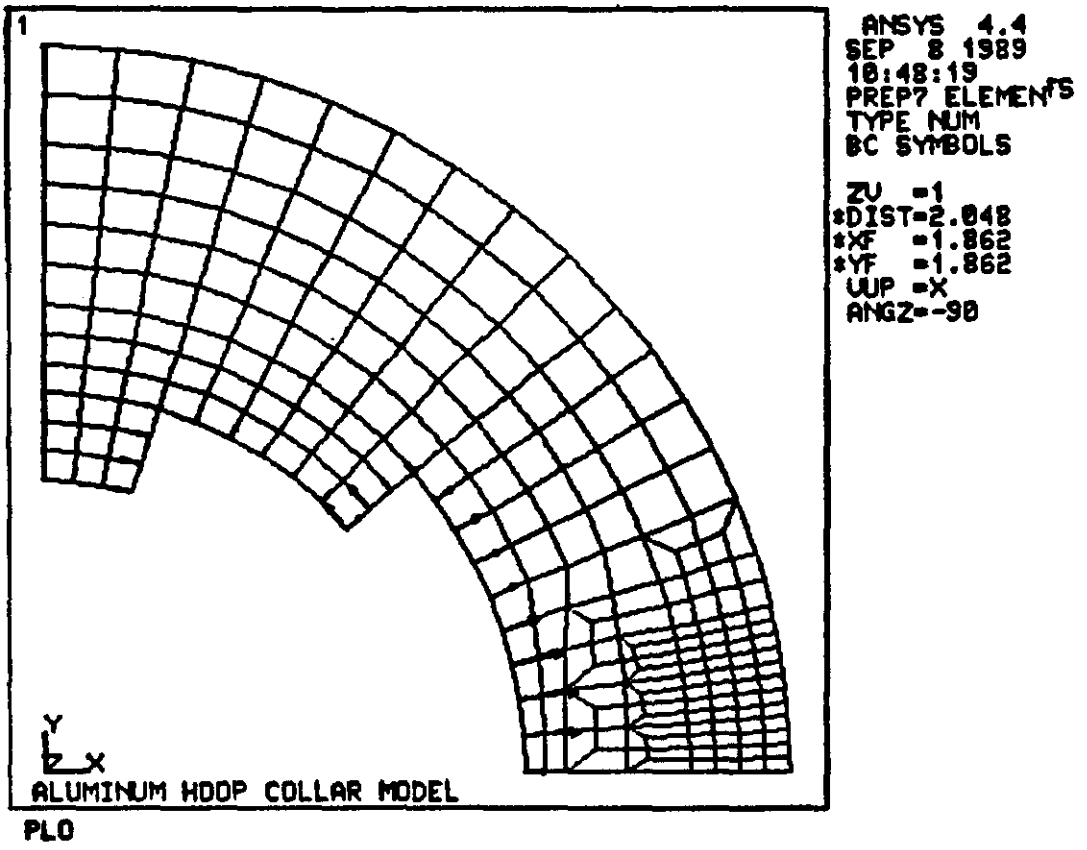

Figure 3.10: Aluminium Hoop Collar Model

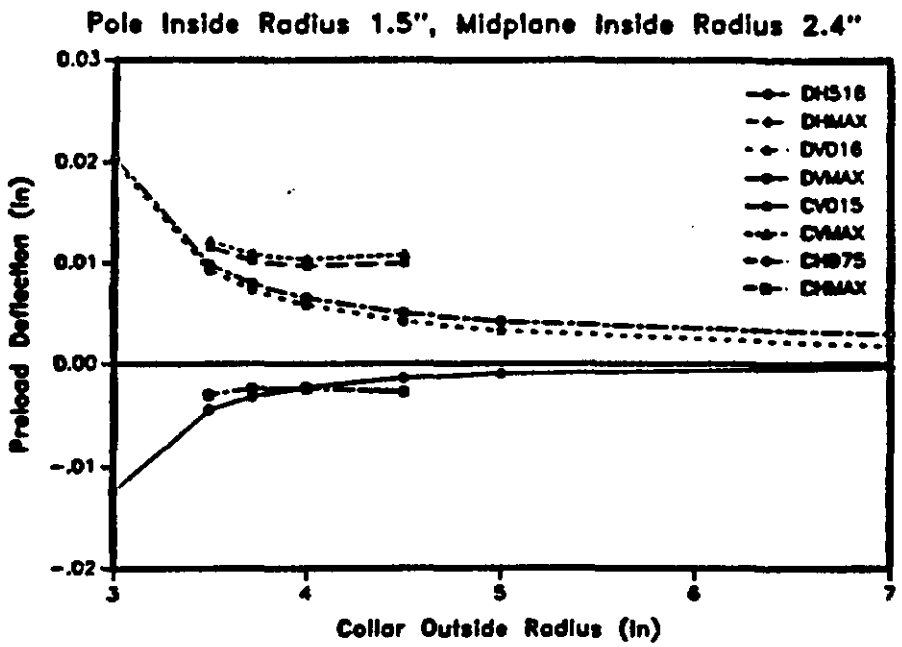

Figure 3.11: Collar deflection

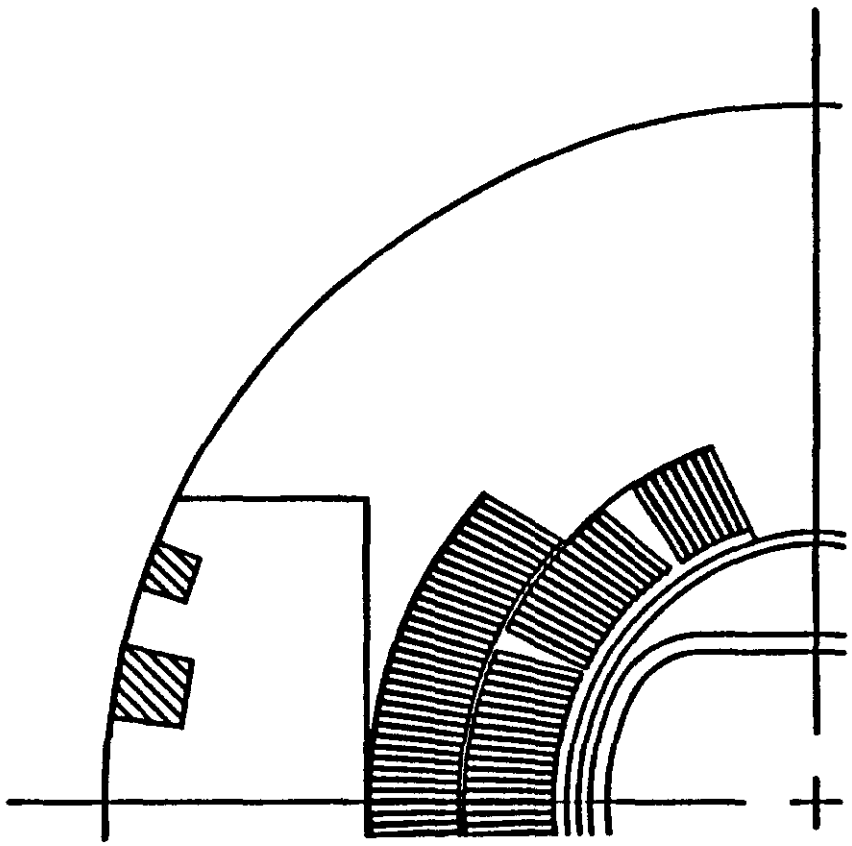

Figure 3.12: Dipole Collars

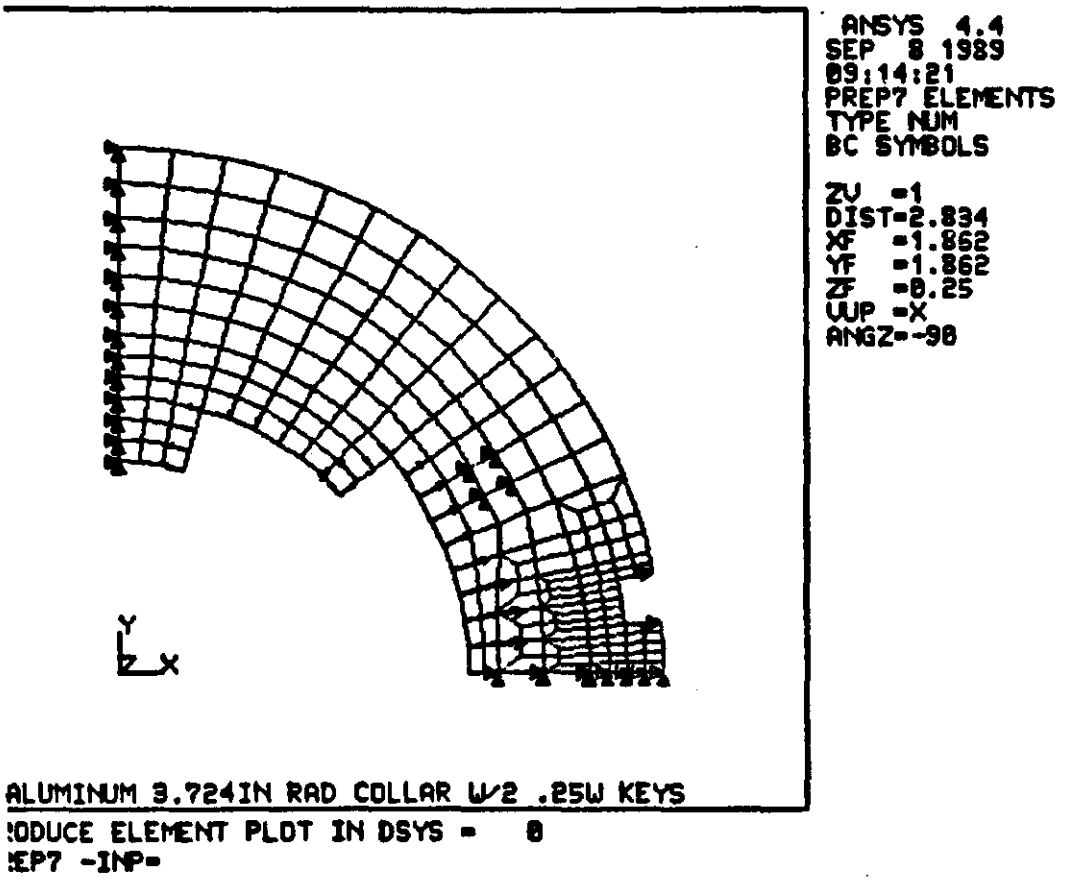

:ODUCE ELEMENT PLOT IN DSYS = 0
:EP7 -INP=

Figure 3.13: Front Collars

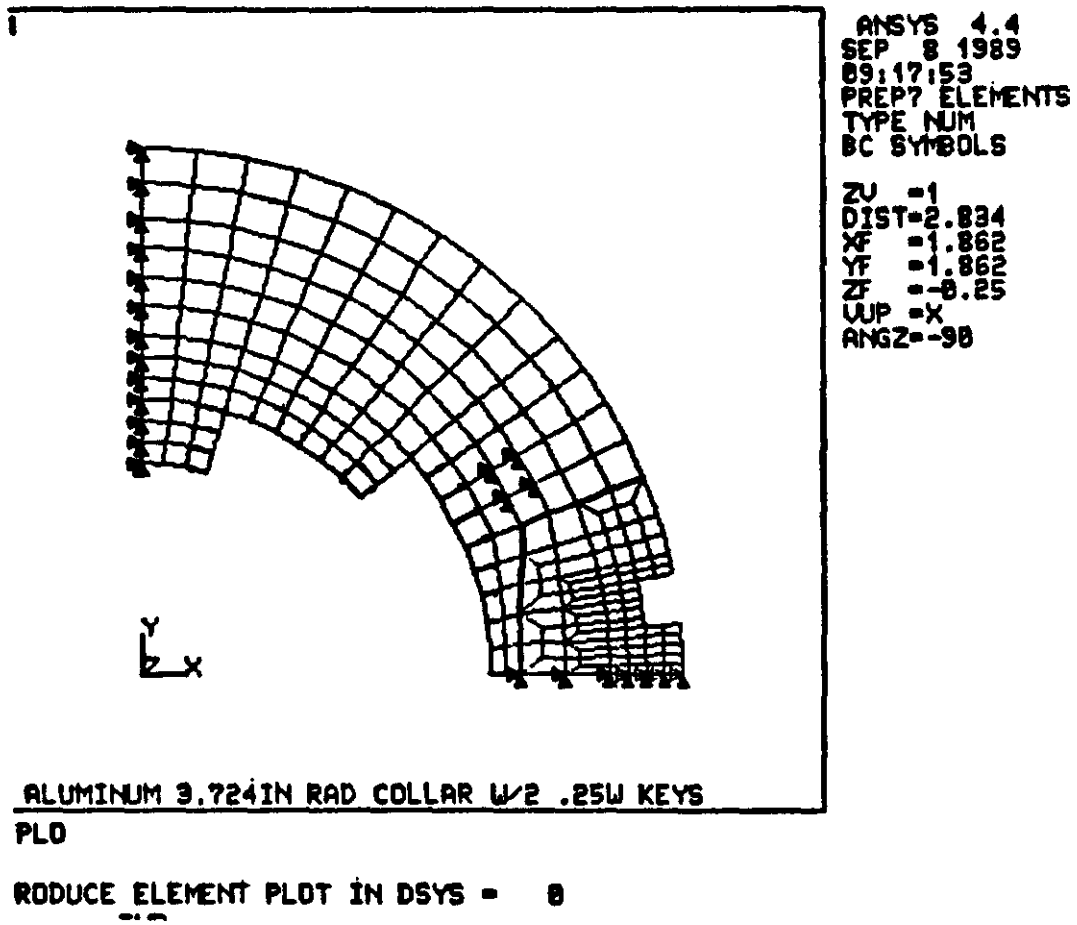

PLO

RODUCE ELEMENT PLOT IN DSYS = 0

Figure 3.14: Back Collars

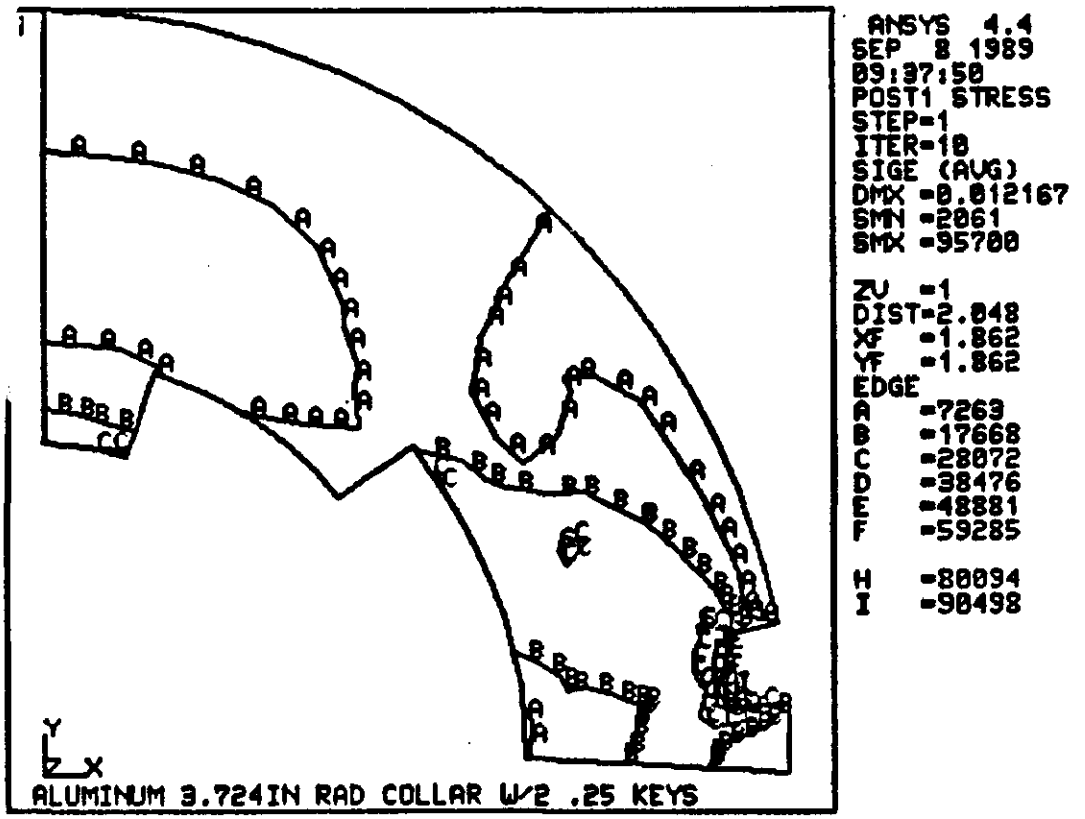

PLST,SIGE

PRODUCE STRESS PLOT, LABEL= SIGE KAVG= 0

Figure 3.15: Stress Plot W/2.25 Keys

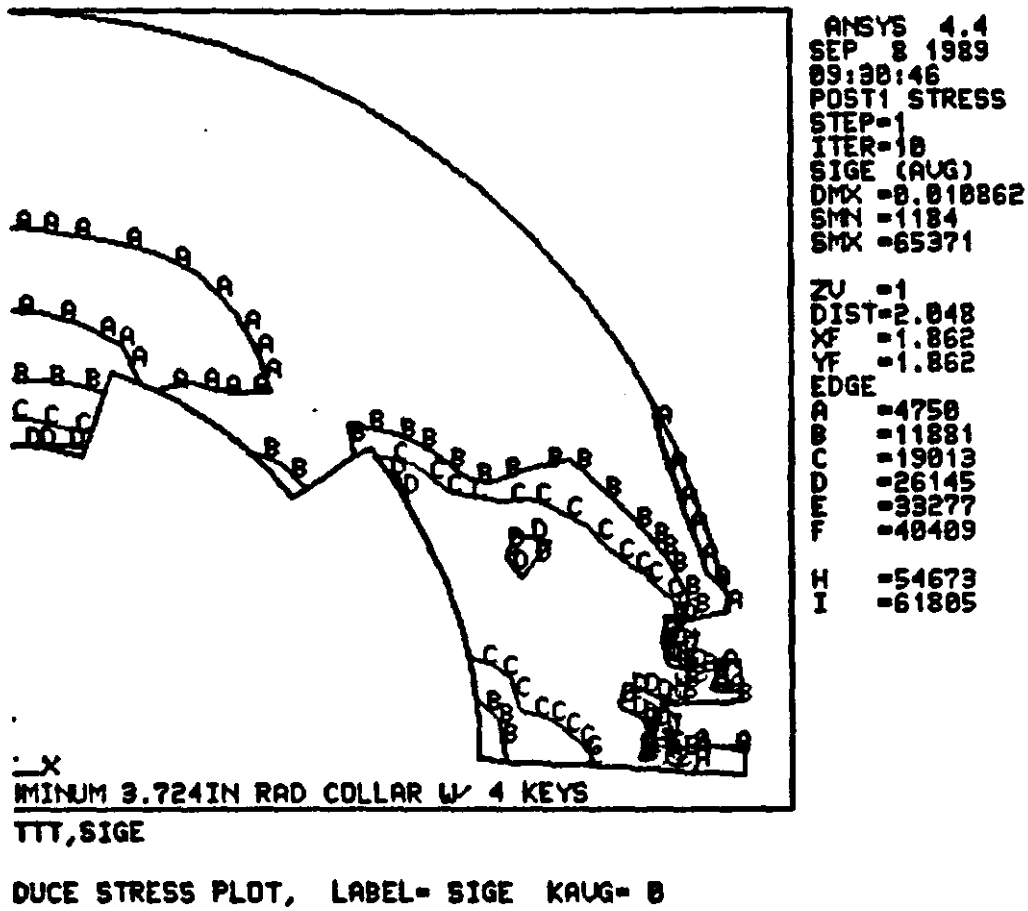

Figure 3.16: Stress Plot W/4 Keys

liters.

3.4 COLD MASS SUSPENSION SYSTEM

3.4.1 Introduction

The suspension system in a superconducting magnet performs two functions. First it resists structural loads imposed on the cold mass assembly ensuring stable operation over the course of the magnet's operating life. Second it serves to insulate the cold mass from heat conducted from the environment.

The evolution and selection of the suspension system for cold iron superconducting magnets has been well documented over the course of the past several years [10, 11]. The purpose of this chapter is not to reiterate the selection process, but rather to give a detailed accounting of the current design, the analysis used in predicting its performance, and the selection of suspension component materials.

Figure 3.17 illustrates the major components of the suspension system. The magnet assembly is supported vertically and laterally at two places along its length. Supports are positioned to minimize the overall cold mass deflection and are spaced 185 inches apart. To accommodate axial shrinkage during cooldown, the magnet assembly is free to slide axially at one of the supports. The other serves as the anchor position. To distribute any imposed axial load to each support, a tie bar is used to connect the tops of the two posts. That is, any vertical or lateral load applied to the magnet assembly is transmitted

directly to the supports. An axial load is transmitted to the anchor post and in turn to the remaining support through the tie bar.

Table 3.6 provides a summary of the structural design criteria for the suspension system.

3.4.2 Support Post Design and Analysis

Figure 3.18 illustrates a cross section through a typical re-entrant support post. Each post assembly consists of inner and outer composite tubes connected by an intermediate stainless steel transition tube. Stainless steel and aluminum discs and rings serve to join the tubes and act as tie points to other cryostat components. The goal of the support post design was to select a geometry and set of materials which resulted in an assembly that satisfied the structural constraints referenced by Table 3.6 while minimizing the conductive heat loads.

3.4.3 Structural Analysis

The primary structural loads and directions are shown in Figure 3.19. F_a denotes an axial load applied to the top of the support post through the anchor attachment point. Axial refers to the long axis of the dipole assembly. F_l and F_v denote lateral and vertical loads respectively and are applied to the post through the cold mass cradle. The lines of action for both pass through the cold mass centerline. Shipping, handling, and seismic loads potentially act in all three directions. Quench loads act as an additional axial load. The

Shipping and handling loads:	vertical	2.0 G
	lateral	1.0 G
	axial	1.5 G
Seismic load guidelines:	Nuclear Regulatory Guide 1.61	
	vertical and horizontal spectra scaled by 0.3	
Maximum axial quench load:		15000 lb

Table 3.6: SSC Dipole Structural and Thermal Load Summary

weight of the cold mass acts as an additional vertical load. Calculations and tests have shown that the bending loads resulting from the axial and lateral loads produce the highest stresses in the post assembly. Of particular interest are the membrane and shear stresses in the two composite tubes.

Using the notation in Figures 3.19 and 3.20 the maximum stresses in tubes 1 (outer) and 2 (inner) due to F_l, F_a, and F_v are

$$\sigma_{il} = \frac{F_1(L_i)d_i}{2I_i} \tag{3.4}$$

$$\sigma_{ia} = \frac{F_a(L_i - L_3)d_i}{2I_i} \tag{3.5}$$

$$\sigma_{iv} = \frac{F_v}{A_i} \tag{3.6}$$

$$\tau_{il} = \frac{2F_l}{A_i} \tag{3.7}$$

$$\tau_{ia} = \frac{2F_a}{A_i} \tag{3.8}$$

where σ_{il}, σ_{ia}, σ_{iv} = bending stresses resulting from lateral, axial,and vertical loads in tube i, τ_{il}, τ_{ia} = shear stresses resulting from lateral and axial loads in tube i L_i = L_1 *or* L_2. The σ_i's are the stresses acting along the

axis of each tube. The τ_i's are the shear stresses acting through the respective cross sections. For thin walled tubes there are three values for limiting stresses induced by F_l, F_a, *and* F_v. They are the ultimate tensile stress, ultimate shear stress, and the stress which causes elastic instability in the tube wall (local buckling). The ultimate tensile and shear stresses are specified to the tube manufacturer and are used to determine the fiber and resin types and the fiber orientation. The stress which causes elastic instability is determined by the composite material properties and the tube geometry. For the tube in these supports, elastic instability will occur whenever [12]

$$\sigma_{ci} > \frac{2E_i t_i}{(1.5)\sqrt{3}\sqrt{(1-\mu_i)}d_i^2} \tag{3.9}$$

where σ_{ci} = bending stress at the onset of elastic instablility in tube i

E_i= Young's modulus of tube i

t_i= tube thickness of tube i

n_i= Poisson's ratio of tube i

d_i= diameter of tube i

The overall height and diameter of the support post and the ratios of the various thermal path lengths are determined in large part by the cryostat configuration and the conductive heat load constraints. The design optimization of the complete assembly essentially consists of determining the composite tube materials and wall thicknesses. Equations (3.4) through (3.8) are set equal to the ultimate tensile and shear strengths and to the elastic stability

constraint represented by equation (3.9) to determine the optimum value for the wall thickness. Note that although the wall thickness does not appear explicit in any of equations (3.4) through (3.8), it is implicit in the expressions for A and I.

As an example, consider the case of some lateral load, F_l acting on a post assembly. Using equations (3.4), (3.8), and (3.9) the optimum geometry would satisfy the more stringent of the following three criteria.

$$\sigma_{il} = \sigma_{ui} \tag{3.10}$$

$$\tau_{il} = \tau_{ui} \tag{3.11}$$

$$\sigma_{il} = \sigma_{ci} \tag{3.12}$$

where σ_{il}, τ_{il}, σ_{ci} = stresses defined above, σ_{ui} = ultimate tensile strength for tube i, τ_{ui}= ultimate shear strength for tube i.

In order to satisfy all of the various load cases, a computer program was written to calculate the tube thicknesses required to satisfy the structural requirements given a set of input criteria. The input consists of the structural loads, material properties, and fixed geometric parameters. The output consists of the tube thicknesses which just satisfy the tensile, shear, and critical stresses above, the resulting stresses, and the resulting thermal performance.

Table 3.8 contains an output listing from the optimization program for a 1g lateral load applied at the cold mass centerline. Using this set of input parameters, the resulting thicknesses are 0.177 inches for the outer tube and 0.191 inches for the inner. Both tubes are sized based on the ultimate tensile

strength (SigU). The resulting maximum stresses are 20000 psi in the outer tube and 30000 psi in the inner. Note that these are exactly equal to the material ultimates (SigU1 and SigU2) when the ultimates are derated by the safety factor (SF) indicating that the solution represents an optimum condition.

Thermal Analysis

In addition to understanding the structural performance of the support posts it is critical that an accurate prediction of the conductive heat load be made to each thermal station. Figure 3.21 illustrates a thermal model of a typical reentrant support post. Q80, Q20, and Q4.5 represent the heat loads to the 80, 20, and 4.5K intercepts respectively and are given by

$$Q_{1.8} = \frac{A_c}{L_c}\int_{1.8}^{T_i} k_i dT \tag{3.13}$$

$$Q_{4.5} = \frac{A_i}{L_2}\int_{4.5}^{80} k_o dT - Q_{1.8} \tag{3.14}$$

$$Q_{80} = \frac{A_o}{L_1}\int_{80}^{300} k_o dT - Q_{4.5} - Q_{1.8} \tag{3.15}$$

where A_o, A_i = outer and inner tube cross sectional areas

A_c = equivalent cold mass cradle cross sectional area

L_1 = 300K to 80K path length

L_2 = 80K to 4.5K path length

L_c = equivalent cold mass cradle length

k_o, k_i = outer and inner tube thermal conductivities

T_t = temperature at the top of the support post and is found from the steady state solution to

$$\frac{A_i}{L_3}\int_{T_t}^{4.5} k_i dT = \frac{A_c}{L_c}\int_{1.8}^{T_t} k_c dT \tag{3.16}$$

where k_c = cold mass cradle thermal conductivity L_3 = 4.5K intercept to top of support post length.

Given a support post geometry and the thermal conductivity integrals for the composite tubes and cold mass cradle, equations (3.13) through (3.16) can be solved for the steady state heat loads and the temperature at the top of the post assembly. Again referring to Table 3.8, the resulting heat loads to 80K, 4.5K, and 1.8K are 7.7, 1.25, 0.01 W respectively. The equilibrium temperature at the top of the post is 4.96K.

Shrink Fit Joints

Connections between composite tubes and metallic end fittings have historically been made using some form of mechanical fastener or chemical bond. Mechanical fasteners typically introduce unwanted stress concentrations at the joint. Chemical bonds, e.g. epoxy joints, are susceptible to failures caused by differential thermal expansion of the joint components. To avoid these complications and to ensure long term reliability, the composite to metal joints in both the support posts and anchor tie bars are effected by shrink fitting the composite tube between an inner metal disc and an outer metal ring. A typical joint configuration is shown in Figure 3.22.

Each of the joints in the support posts resists both axial loads and overturning moments. An axial load is one which tries to pull the joint apart. An overturning moment is one which tries to twist it apart. Using the nomenclature in Figure 3.22 the forces and moments required to cause the joint to fail are given by

$$F_i = P_i(2\pi b t \mu_i) \tag{3.17}$$

$$F_o = P_o(2\pi c t \mu_o) \tag{3.18}$$

$$M_i = 4P_i\mu_i b^2 t \tag{3.19}$$

$$M_o = 4P_o\mu_o c^2 t \tag{3.20}$$

where F_i, F_o = applied forces which induce slippage of the inner and outer interfaces respectively, M_i, M_o = applied moments which induce slippage of the inner and outer interfaces respectively, μ_i, μ_o = coefficient of friction at the inner and outer interfaces respectively, P_i, P_o = inner and outer interface pressures respectively and are given by

$$P_i = \frac{P_o(k_4 + k_5) - \delta_o}{k_6} \tag{3.21}$$

$$P_o = \frac{\delta_i k_6 + \delta_o(k_1 + k_2)}{(k_4 + k_5)(k_1 + k_2) - k_3 k_6} \tag{3.22}$$

where δ_i, δ_o = inner and outer interface radial interference fits respectively k_1, k_6 = constant parameters determined by the joint geometry and material properties and are given by

$$k_1 = \frac{b}{E_1}\left[\frac{b^2 + a^2}{b^2 - a^2}\right] - \mu_1 \tag{3.23}$$

$$k_2 = \frac{b}{E_2}\left[\frac{c^2+b^2}{c^2-b^2}\right] + \mu_2 \tag{3.24}$$

$$k_3 = \frac{b}{E_3}\left[\frac{2c^2}{c^2-b^2}\right] \tag{3.25}$$

$$k_4 = \frac{c}{E_3}\left[\frac{d^2+c^2}{d^2-c^2}\right] + \mu_3 \tag{3.26}$$

$$k_5 = \frac{c}{E_2}\left[\frac{c^2+b^2}{c^2-b^2}\right] - \mu_2 \tag{3.27}$$

$$k_6 = \frac{c}{E_2}\left[\frac{2b^2}{c^2-b^2}\right] \tag{3.28}$$

where E_1, E_2, E_3= Young's modulus for the disc, tube, and ring respectively, μ_1, μ_2, μ_3= Poisson's ratio for the disc, tube, and ring respectively.

As with the structural and thermal analysis referenced above, a computer program was written which calculates the required radial interferences at the inner and outer interfaces required to produce a joint that satisfies either a maximum input axial force or overturning moment.

Table 3.9 contains a listing of the analysis results for a typical shrink fit joint. This particular case is for the joint at the 300K end of the support post. The input overturning moment (MRes) for this example was 115000 in-lb which is the moment due to a lg lateral load on a support. The force to slip (FSlip) was input as zero. The program calculates the interference fit that satisfies the more stringent of these two parameters. The resulting radial interference is 0.009 inches. The lowermost portion of this listing contains the resulting radial and circumferential stresses (SigR and SigC) in the disc, tube, and ring.

Material Selections

References have been made throughout the preceding sections to some of the unique material property issues encountered in this design process. Of particular interest are the composite materials used in the support post and anchor tie bar tubes. Until recently the primary structural composite materials found in superconducting magnets were glass reinforced composites in an epoxy matrix. Familiar names are G-10, G-10CR, G-11, and G-11CR. These continue to be excellent choices. They are readily available, have well characterized structural and thermal properties, are relatively strong, have low thermal conductivity, and are inexpensive.

Recent years have brought developments in new fibers for use in composites, some of which offer advantages in terms of strength, some in terms of thermal conductivity, some in both. It is well known, for example that graphite composites can offer greater strength and stiffness than their glass counterparts. Less known is their low thermal conductivity, particularly at low temperature. At room temperature the thermal conductivity of G-11CR is four times less than that of the GRP, however, at approximately 40K the curves cross indicating that at low temperature the GRP may in fact provide greater resistance to conductive heat flow [14].

The reentrant design of the support post gave us the option of taking advantage of this behavior. For the outer tube, operating between 300K and 80K, the thermal performance of G-11CR makes it superior to GRP. For the

	FRP Outer GRP Inner	FRP Outer FRP Inner
t, outer (inches)	0.177	0.177
t, inner (inches)	0.191	0.302
Q to 80K (W)	7.7	7.3
Q to 4.5K (W)	1.25	1.62
Q to 1.8K (W)	0.01	0.01

Table 3.7: Comparison of Two Structurally Optimized Support Posts

inner tube, operating between 80K and 1.8K, GRP is better.

Table 3.7 contains the results of the structural optimization described previously and illustrates that the choice of GRP for the inner tube does in fact produce an assembly with lower 4.5K heat load than an assembly which uses G-11CR (FRP) for both tubes.

3.4.4 Anchor System

The support posts used in SSC cryostats share vertical and lateral loads induced by shipping, handling, and seismic loads. Thermal contraction of the cold mass assembly during warmup and cooldown necessitates axial sliding between the cold mass and the non-anchor Rpost. The anchor post is attached rigidly to the cold mass assembly to ensure correct axial position within the vacuum vessel. Given no other restraint, this means that this post would see the entire axial component of any load. A single post is incapable of handling these loads alone. Utilizing a 'strong' post at the anchor would

impose intolerable heat loads on the cryogenic system.

Ideally one would like an anchor system with negligible thermal impact on the cryogenic system and which introduced no perturbations into other cryostat components. Recognizing that the bending strength of both supports could be combined to effectively act as a single axial restraint, we have chosen to connect the top ring of each post to that of its neighbor with an axial tie bar.

The degree to which an axial load is shared by the two supports is determined by the ratio of the axial tie bar stiffness to the bending stiffness of the support posts. The greater that ratio, the more uniform the load distribution. For support and anchor tie bar components appropriate for use in the Phase III dipole, 60% of an axial load is transmitted to the anchor post and the remaining 40% to the fixed post.

3.5 Cryostat Design

The cryostat for the Phase III dipole has its origin in SSC main ring dipole. Using Figure 3.23, the cryostat consists of a vacuum vessel, 80K and 4.5K shields, cold assembly, multilayer insulation (MLI), and suspension assembly. Unlike it's SSC counterpart, which operates at 4.5K only, the Phase III dipole is designed to operate at 4.5K in fixed target mode and 1.8K in collider mode. This dual mode operation and a different cryogenic system accounts for most of the differences in the piping schemes between the two cryostat systems.

The vacuum vessel is a 25 inch diameter, 1/4 inch thick, carbon steel pipe. It is fabricated from three lengths of pipe joined at stiffening rings located at the support post locations. The stiffening rings are required to transmit internally generated loads from the support posts to ground.

The two shells radially inward from the inner surface of the vacuum vessel are thermal radiation shields. They serve as heat sinks to minimize radiative heat transfer to the collared coil assembly. The 80K shield intercepts heat radiating from the 300K surface of the vacuum vessel at LN2 temperature. The 4.5K shield intercepts heat radiating from the inner surface of the 80K shield. Both shields are aluminum shells welded to their respective cooling tubes. The 4.5K shield has 3/8 inches of the same material. The 4.5K shield is actively cooled during collider mode only when the collared coil is operating at 1.8K. In fixed target mode, the 4.5K shield is allowed to float, i.e., it is not actively cooled. Both shields are covered with MLI in order to minimize radiative heat transfer to their surfaces. The 80K shield is covered with 3/4 inches of alternating layers of reflective mylar and a nylon spacer material.

The cold mass assembly consists of the collared coil assembly, iron yoke, and containment skin. The iron yoke is truncated at the top and bottom to reduce the supported weight and to provide space for suspension system components. Unlike it's SSC counterpart, the cold mass containment is not a pressurized vessel. Rather, the iron is cooled by conduction through two 1/2 inch diameter cooling tubes swaged into the iron laminations. This

minimizes the liquid volume at 1.8K and eliminates the need to provide strength enough in the skin to contain the quench pressures generated in the collared coil assembly. The inner diameter of the iron yoke is separated from the collared coil assembly by a 1/16 inch stainless steel skin. The Phase III dipole requires a sagitta, or curve in the cold mass assembly of approximately 9 mm. This is effected by cutting a curve into the top and bottom cold mass containment plates and forming the outer skins to conform to that curve.

The thermal radiation shields and cold mass assembly are supported by the suspension system. Refer to the preceding section for a complete description of the supports and axial anchor assembly.

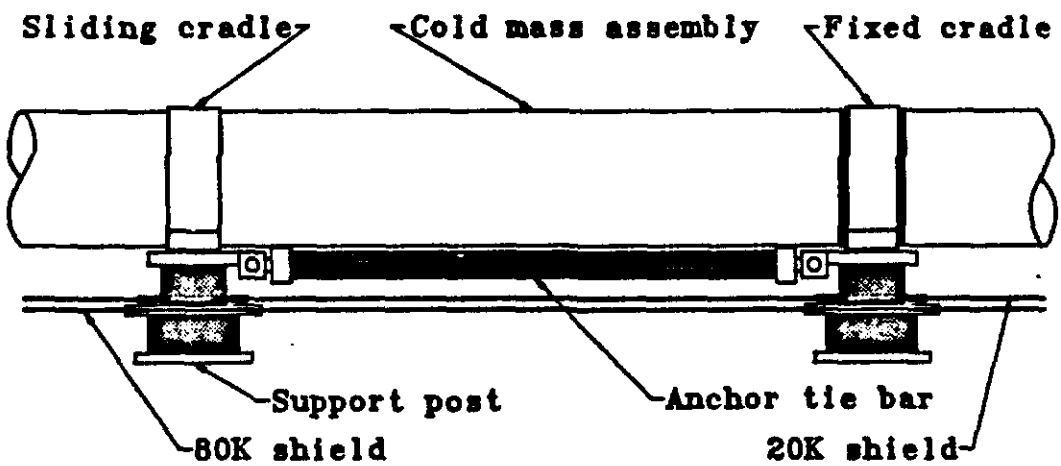

Figure 3.17: Suspension System Components

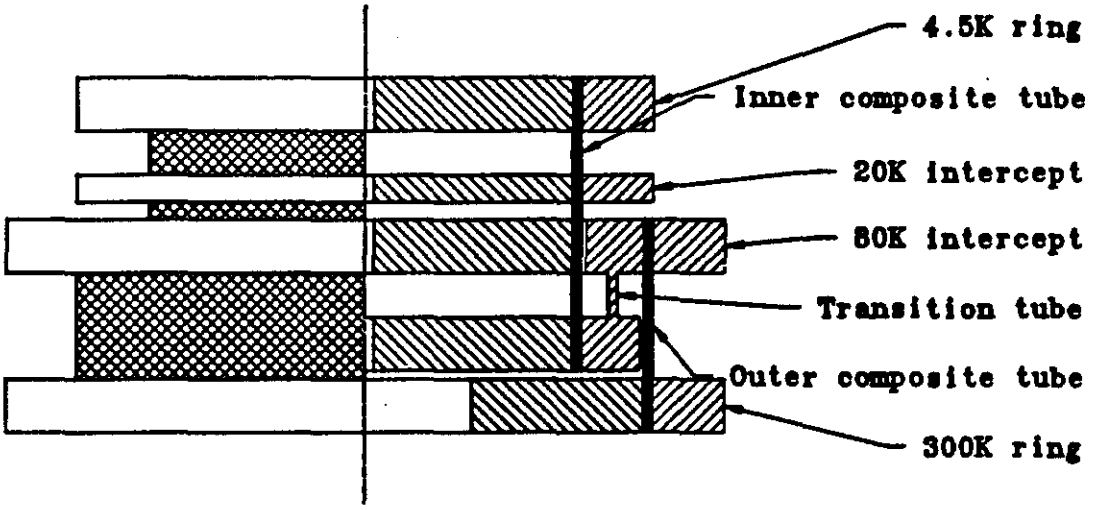

Figure 3.18: Support Post Cross Section

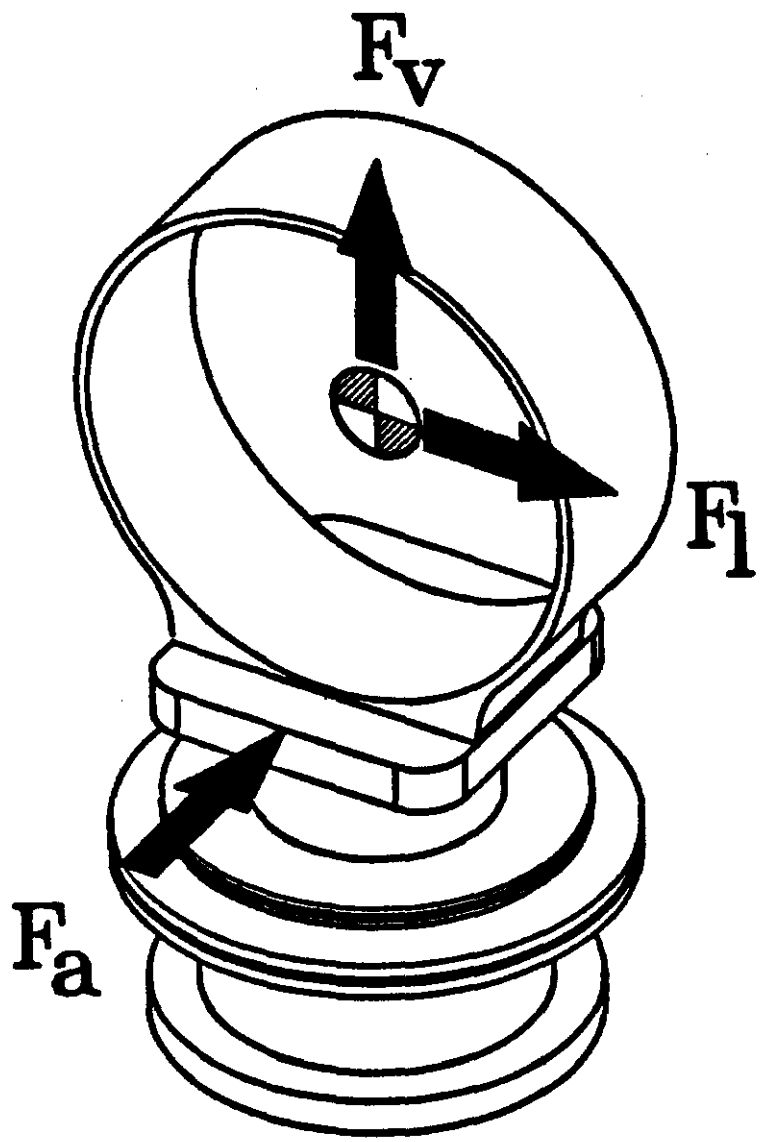

Figure 3.19: Structural Load and Direction Notation

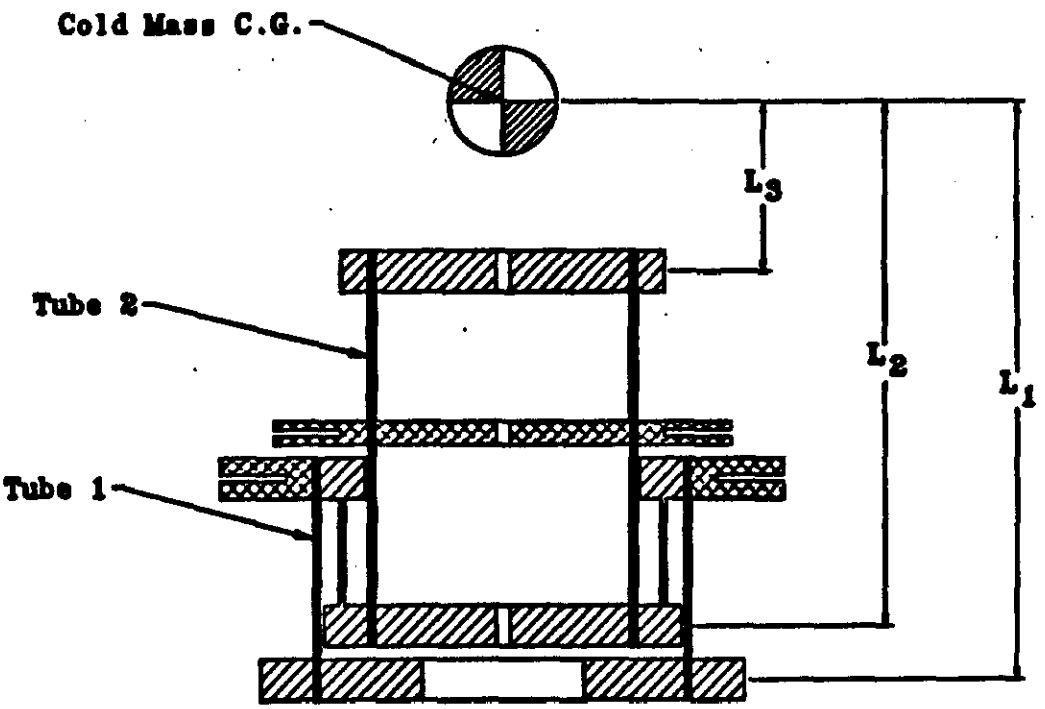

Figure 3.20: Structural Analysis Notation

```
*****************************************
*****  Post Optimization...Input  *****
*****************************************

Note..........: Phase III Dipole Suspension
Fg........(lb):   12500.0
Fq........(lb):       .0
W.........(lb):  -12500.0
SF............:      2.0
E1.......(psi):   .40E+07
V1............:      .200
G1.......(psi):   .38E+06
E2.......(psi):   .10E+08
V2............:      .200
G2.......(psi):   .38E+06
SigU1....(psi):   40000.0
TauU1....(psi):   20000.0
SigU2....(psi):   60000.0
TauU1....(psi):   30000.0
L1........(in):    11.375
L2........(in):    10.375
L3........(in):     7.375
D1........(in):     8.000
D2........(in):     6.000
TWarm......(K):   300.000
TShld1.....(K):    80.000
TShld2.....(K):     5.000
TCold......(K):     1.800
LThrm1....(in):     1.500
LThrm2....(in):     1.500
LThrm3....(in):      .625
LThrm4....(in):      .500
ASlide...(in2):      .010
OuterMtl......:        2  G-11 (WARP)
InnerMtl......:        3  CARBON FIBER COMPOSITE (UNIAXIAL)
SlideMtl......:        1  304 STAINLESS STEEL

*****************************************
*****  Resulting Tube Thicknesses  *****
*****************************************

T1 (when sized for SigU)....(in):     .1766
   (when sized for SigEI)...(in):     .1331
   (when sized for TauMx)...(in):     .1007

T2 (when sized for SigU)....(in):     .1911
   (when sized for SigEI)...(in):     .0914
   (when sized for TauMx)...(in):     .0898
```

```
*********************************
*****  Resulting Stresses  *****
*********************************

Sig1 (when sized for SigU)....(psi):   20000.0
     (when sized for SigEI)...(psi):   26143.3
     (when sized for TauMx)...(psi):   34162.7

Sig2 (when sized for SigU)....(psi):   30000.0
     (when sized for SigEI)...(psi):   59873.5
     (when sized for TauMx)...(psi):   60950.3

Tau1 (when sized for SigU)....(psi):    5760.3
     (when sized for SigEI)...(psi):    7599.9
     (when sized for TauMx)...(psi):   10000.0

Tau2 (when sized for SigU)....(psi):    7187.3
     (when sized for SigEI)...(psi):   14727.7
     (when sized for TauMx)...(psi):   15000.0

*********************************************
*****  Resulting Thermal Performance  *****
*********************************************

T at top (when sized for SigU).........(K):    4.9602
         (when sized for SigEI)........(K):    4.9203
         (when sized for TauMx)........(K):    4.9188

Q to Cold end (when sized for SigU)....(W):     .0003
              (when sized for SigEI)...(W):     .0003
              (when sized for TauMx)...(W):     .0003

Q to Shield 2 (when sized for SigU)....(W):    1.2533
              (when sized for SigEI)...(W):     .6098
              (when sized for TauMx)...(W):     .5987

Q to Shield 1 (when sized for SigU)....(W):    7.6918
              (when sized for SigEI)...(W):    6.1700
              (when sized for TauMx)...(W):    4.5536
```

Table 3.8: Summary of Structural Analysis Results

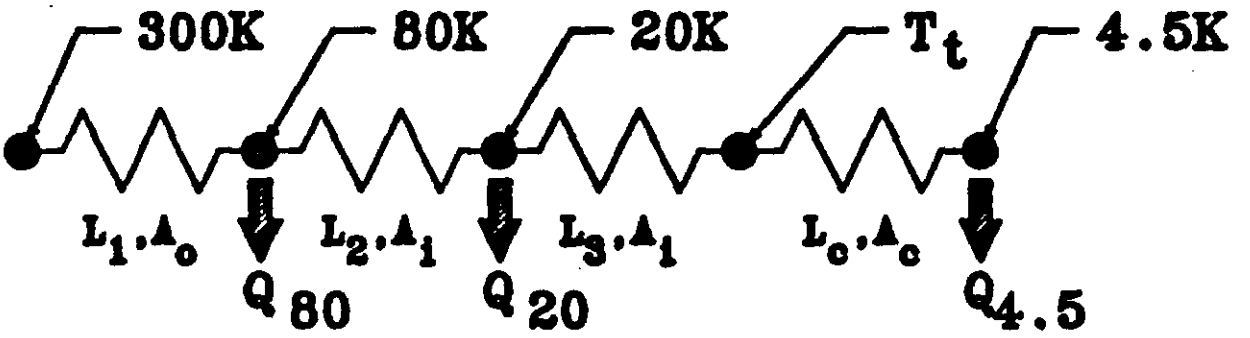

Figure 3.21: Thermal Analysis Notation

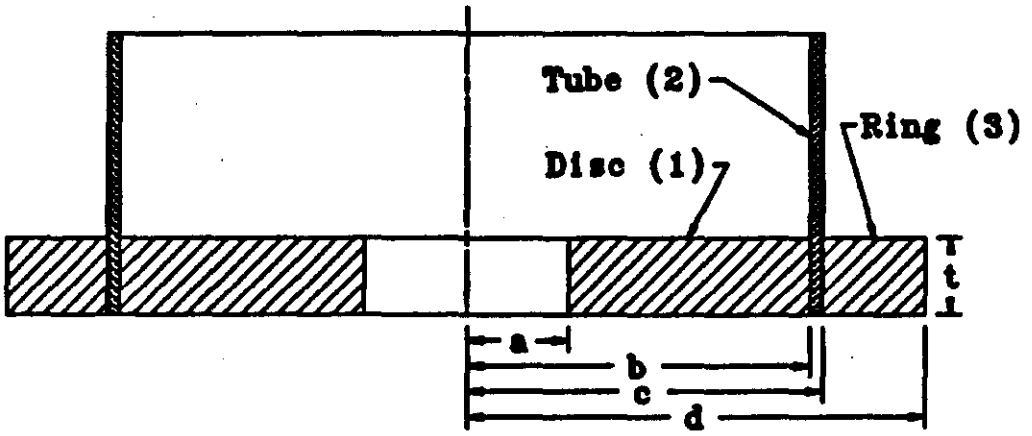

Figure 3.22: Shrink Fit Joint Notation

```
*****************************************
*****  Shrink Fit Analysis...Input  *****
*****************************************

Note..............................:  Phase III 300K Joint
Dimension, A................(in):    1.5000
           B................(in):    3.8230
           C................(in):    4.0000
           D................(in):    5.0000
           T................(in):     .7500
Material property, E1......(psi):   .28E+08
                   V1...........:     .3330
                   E2......(psi):   .10E+07
                   V2...........:     .2000
                   E3......(psi):   .28E+08
                   V3...........:     .3330
Friction coefficient, Mu........:     .3000
Force to slip, FSlip........(lb):       .0
Resisting Moment, MRes...(in-lb):  115000.0

*********************************************
*****  Shrink Fit Analysis...Results  *****
*********************************************

Interference reqd at inner interface...(in):     .0413
                     outer interface...(in):    -.0328

Total radial interference reqd.........(in):     .0086

Contact pressure at inner interface...(psi):    8742.7
                    outer interface...(psi):    7986.1

Actual force to slip...................(lb):   47251.3
       resisting moment.............(in-lb):  115000.0

                                 Ri        Rm        Ro
                              ========  ========  ========
Inner disc...SigR...(psi):        .0   -7051.2   -8742.7
             SigC...(psi):  -20667.1  -13615.9  -11924.4

Tube.........SigR...(psi):   -8742.7   -8351.6   -7986.1
             SigC...(psi):    8742.7    8351.6    7986.1

Outer ring...SigR...(psi):   -7986.1   -3330.3       .0
             SigC...(psi):   36381.2   31725.3   28395.1
```

Table 3.9: Summary of Shrink Fit Analysis

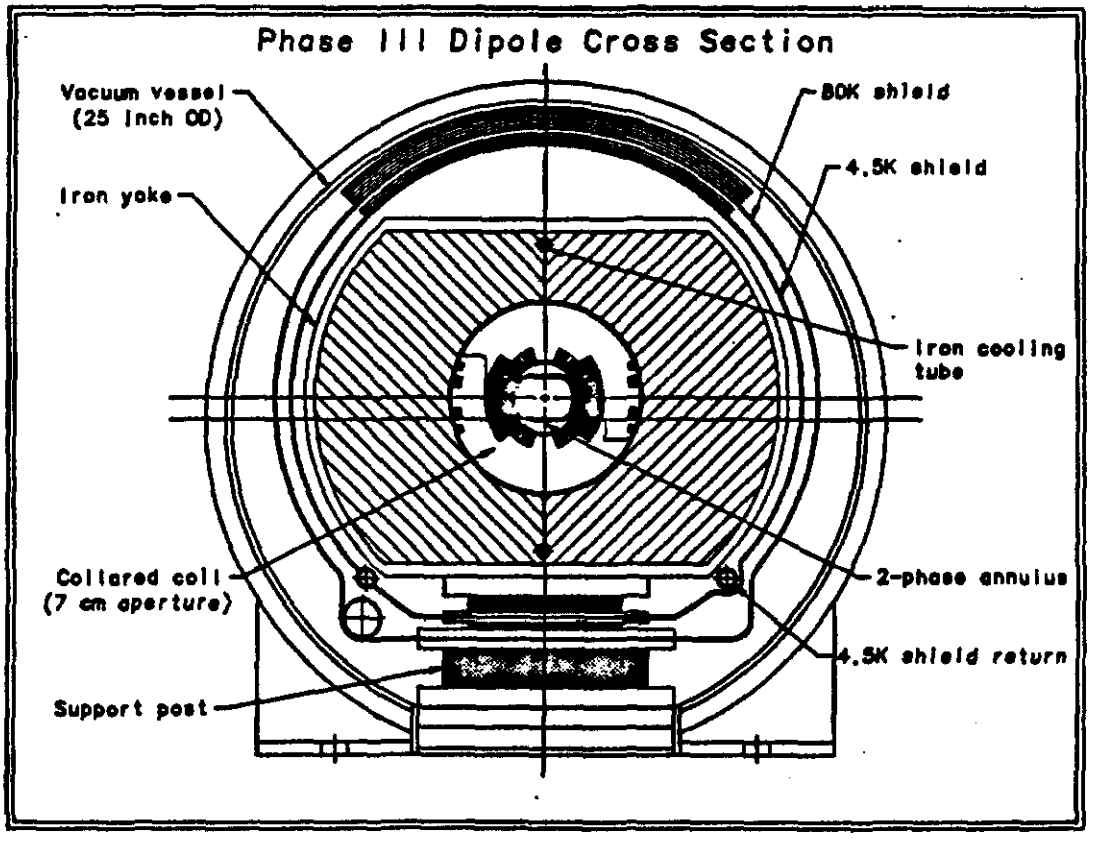

Figure 3.23: Phase III Dipole cross Section

Chapter 4

Cryogenic Properties

4.1 Tevatron Cryogenic System

Refrigeration for the existing Tevatron is supplied by a hybrid system consisting of a Central Helium Liquefier (CHL) connected to 24 satellite refrigerators by a 7 km LHe, LN2 transfer line. This system provides redundancy by relying more heavily on one system should a problem develop in the other. Also, large inventories of liquid helium stored at the CHL dewar system are available for fast magnet quench recovery or cooldown following magnet repair. Capacities of the refrigerator system, including the Central Nitrogen Reliquefier (CNL), are shown in Table 4.1.

Each Satellite refrigerator cools two 125m long magnet string in the existing Tevatron. The superconducting magnets are of the warm iron type. Since it is desirable from a magnet field view point to have the iron as close as possible to the superconducting coils, warm iron magnets typically have a high static heat load to 4.6K.

CHL	4000 liters/hour	@ 3 atm, 4.6K
CHL #2	5400 liters/hr	@ 3 atm, 4.6K
CNL	4600 liters/hour	@ 4 atm, 82K
Satellite	966 watts	@ 4.6K

Table 4.1: Tevatron Refrigeration System Capacities

The superconducting coils are bathed in subcooled (single-phase) liquid helium. At the end of the 125m magnet string, the liquid helium is expanded through a Joule-Thomson valve where it becomes a colder mixture of gas and liquid (two-phase). This two-phase mixture counterflow heat exchanges with the collared coil assembly on its way back to the refrigerator. The static and dynamic losses (hysteresis and eddy current) of the 4.6K system is then absorbed by the latent heat in the liquid of the two-phase mixture. The advantage of a continuous two-phase cooling system is that it results in a uniform temperature in the coils through the magnet string.

For simplicity, it is assumed that the same 24 satellite refrigerators will be used in the new Tevatron. It may be desirable to achieve higher magnetic fields in a new Tevatron through lower temperature operation. Three distinct methods could be used to achieve lower temperature operation in the Tevatron cryogenic system.

In the higher temperature range (3.5 - 4.6K), cold compressors would be added between the refrigerator and the load. Figure 4.1 shows one possible cold compressor configuration. Although this particular configuration is not

the most efficient, it is the easiest to analyze. Figure 4.2 shows the refrigeration required by a satellite refrigerator for each cold watt as a function of temperature for a cold compressor efficiency of 60%.

In the lower temperature range (1.8 - 3.5K), two very different refrigeration stages could be added to the satellite; a warm vacuum pump based system and a magnetic refrigerator. At the low end (1.8K) it has been shown that either a vacuum pumped system or a magnetic refrigerator operates near 40% of carnot efficiency. Assuming a constant carnot efficiency of 40% results in the satellite watts per cold watt curve of Figure 4.3.

Figures 4.2 and 4.3 can be used to determine a satellite refrigerators capacity at a given temperature. For example, a possible collider mode would utilize 1.8K refrigeration as well as 4.5K refrigeration for shielding. The estimated heat load and capacities are given in Table 4.2

4.2 Fixed Target Operation

The 4.5K heat load of the new Tevatron will be dominated by AC losses in the coil (predominantly hysteresis in the conductor) as shown in section 2.5. Three options are possible to remove this heat to maintain a reasonable ΔT throughout the magnet string. They are:

1. Use a circulating pump to achieve high single-phase flowrates

Estimated Loads

4.5K shield load	200 watts
1.8K load with pump work	20 watts

Estimated Capacities

Stable satellite operation at 4.5K	850 watts
less 4.5K load	-200 watts
	650 watts

From Figure 4.3, it requires 6 watts at 4.5K per watt at 1.8K

1.8K capacity = 650 watts/6 = 117 watts
(which is considerably higher than the estimated 1.8K heat load)

Table 4.2: 1.8K Collider Heat Loads and Capacities

Advantages	- Good heat transfer
Disadvantages	- Pump reliability
	- Requires large single-phase passage
	- Pump work adds to heat load

2. Use recoolers in spool pieces

Advantages	- Simplifies magnet
Disadvantages	- High flows would still be required (pump)
	- Greatly complicates spool piece

3. Use continuous two-phase cooling

Advantages	- removes heat uniformly
Disadvantages	- Complicates magnet design
	- Potential time constant problems

Any of these options would be acceptable for a for a purely 4.5K machines. A lower temperature operation in collider mode prohibits the use of methods 1 and 2 due to large single-phase passage sizes (long cooldown times) and possible recooler valve leakage (liquefier load) respectively.

As a result, the new Tevatron will utilize the same continuous two- phase cooling scheme as the Tevatron. Cryogenically, the main difference in the new Tevatron is in the cold iron magnet design. A cold iron magnet allows for a thermally efficient suspension system design. As a result, a magnet string with a low static heat leak to 4.6K can be built.

Figure 4.4 shows the flow configuration for fixed target mode. Unlike the Tevatron, the new Tevatron heat load will be dominated by AC losses in the coil. As a result, it was desirable to locate the two- phase passage as close to the coil as possible. With the satellite refrigerator capacity and the existing magnet string length, it appears to be possible to locate the two-phase passage between the beam tube and the coil. This scheme will minimize the ΔT between the coil and the two-phase.

The selected two-phase geometry is shown in Figure 4.5. The passage was sized in such a way to have a pressure drop similar to the Tevatron (resulting in a 50 mK temperature difference along the string due to pressure drop). Manifolding of the passage at the ends of the magnet would have to be designed to avoid gas traps due to stratification.

This geometry appears to be ideal for removing AC losses in the coil. Static heat load would be intercepted by a small 4.5K flow ($\sim 1g/s$) which first passes through the cold iron and then the 4.5K shield and returns to the refrigerator at $\sim 20K$.

The cycle time used in fixed target operation will be limited by one of two constraints; satellite refrigerator capacity or heat transfer from the coil to the two-phase. A first pass look at heat transfer suggests that the satellite capacity will limit the cycle. The AC losses for a typical four cell pair of magnet strings has been estimated as $61{,}000/\tau$ watts; where τ is the cycle time in seconds. If we assume a stable maximum capacity for a satellite of 850 watts and a static heat load of 200 watts, then 650 watts are available for dynamic losses. This equates to a 94 second cycle.

For this design, the AC losses are over a factor of three times the static losses. (As a comparison, the Tevatron is a factor of about 3/4.) This larger swing in heat load will require a smarter controls system. The refrigerator will need to anticipate when a ramping condition is to begin. Conversely, refrigeration capacity will be reduced if the ramp is to be off for "extended"

periods of time.

4.3 Collider Operation

During collider physics, magnets are ramped to full field and remain there for many hours. This reduces the refrigeration load by "eliminating" dynamic losses, but increases the liquefier load necessary for vapor cooled power leads. Liquefier loads tend to not be seen by the satellite refrigerators, only by the central liquefier.

The reserve refrigeration capacity in collider mode can then be used to lower the temperature of the accelerator. A lower temperature refrigeration stage can be added to look like a 4.5K load as described in 4.1. Figures 4.2 and 4.3 can then be used to determine the capacity available at the lower temperature.

Figure 4.6 represents the flow path used in a lower temperature collider mode. A pump loop is used to circulate flow through the coils, returning in two tubes located in the cold iron. The static losses to the single-phase assembly and the pump work is removed in a subcooling dewar at the refrigerator. The two-phase circuit used in fixed target mode is evaculated in collider mode. A small shield flow ($\sim 1g/s$) is circulated through the shield and return line, returning to the refrigerator at $\sim 20K$.

The system shown in Figure 4.6 assumes a temperature below 3.5K. Above that temperature, a separate shield would not be used, and the flow

would resort back to the two-phase cooling system used in fixed target mode. An estimation of heat loads and refrigeration capacity for a 1.8K system is given in Table 4.2.

When designing a system for near 1.8K, several design problems arise.

1. One has to deal with superfluid helium (below 2.17K)

2. Cooldown times from 4.5K to 1.8K are completely dominated by helium heat capacity. Therefore, minimizing the volume of cold helium is important to have reasonable cooldown times. This means that passages cooling the iron must be enclosed tubes, thus eliminating the large void fraction of the iron laminations from adding to the volume. The use of large reserve refrigeration at 1.8K to reduce cooldown time is somewhat of a problem since conventional 1.8K systems (vacuum pump based) do not turn down. Thus, the operating costs would be based on a peak demand used only on quench recoveries.

3. Smaller single-phase passages to help on item 2, can be a problem for quench relieving as well as for heat transfer in fixed target mode.

4. The circulating pump adds nearly as much work to the helium as the static heat load.

An example 1.8K refrigeration system was chosen with the following characteristics (see Figure 4.7).

1. Pressurized superfluid at 3 atmospheres so that the 4.5K shield flow, which is at the same pressure, is supercritical and two- phase flow is avoided.

2. Forced flow of superfluid, as opposed to static superfluid.

3. Temperature rise of 0.1K in superfluid flowing through a magnet string, from 1.8K to 1.9K.

4. Flow forced by a circulating pump as opposed to compressor flow.

5. No superfluid recooling in the tunnel since there is no room for a cold low pressure transfer line in the tunnel.

6. Pumping on the low pressure helium bath by room-temperature vacuum pumps. (Cold compressors for 1.8K refrigeration have been developed, but only for systems of 100 Watts or more at 1.8K. Our heat load from magnets, circulating pump, and miscellaneous sources would total about 40 Watts per house. This is about the size of the 1.8K system at our Magnet Test Facility, which has successfully used warm vacuum pumps).

7. A heat exchanger to warm the low pressure vapor before it enters the pumps, precooling some high pressure helium.

8. Subcoolers at 4.5K and 1.8K with liquid inventory to buffer against upsets.

9. Use of the existing satellite refrigerator cold box and wet expander.

10. Operation of the system in "satellite mode", using a 4.5K helium from CHL as is presently done.

Although the system which is diagrammed in Figure 4.7 utilizes vacuum pumps to obtain a low pressure, low temperature bath which cools the pressurized superfluid, another possible technique is to operate an adiabatic demagnetization refrigerator ("magnetic refrigerator") between 1.8K and 4.5K. The advantage is that 1.8K is achieved without any subatmospheric helium circuits. The primary disadvantage is that magnetic refrigerators which operate in this temperature range have been only as large as a few Watts in capacity; we are looking for a factor of ten larger.

1.8K Hardware Development Required

1. Magnetic refrigerators. We have a contract with Astronautics Corporation of America for a preliminary design study. Present state-of-the-art is around a few watts capacity. We want an order of magnitude larger.

2. Circulating pump. There are papers in the literature describing successful tests of centrifugal pumps operating in superfluid. Since the pump work is in a major heat load in this system, we would want as high as efficiency as we could obtain. More testing and development would be required.

3. Other hardware for superfluid. With either vacuum pumping or magnetic refrigeration special hardware is required for handling superfluid. Every place there is a transition from superfluid to normal fluid, such as at a magnet relief valve or a cooldown line, requires a special check valve or some other restriction to reduce heat in-leak via the superfluid. Power lead feedthroughs and bayonets also require special designs. CEBAF, Tora Supra, and others may provide valuable information.

4. Refrigeration cycle simulation. Steady state, quench recovery, cooldown, failures which may result in reduced capacity, turn- down capabilities, control system design all need to be understood during design with the help of a computer simulation of this refrigeration system.

5. Optimize coil-cooling size. We want magnet reliefs only at "spool pieces" (hence large passage size), but want quick cooldown from 4.5K to 1.8K (hence minimal superfluid volume).

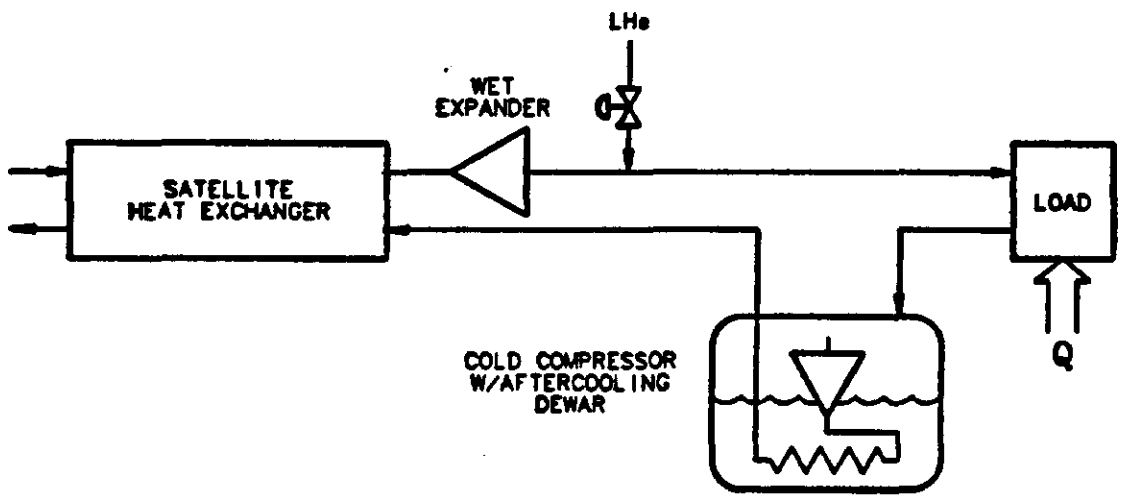

Figure 4.1: Tevatron Satellite Refrigerator with Cold Compressor

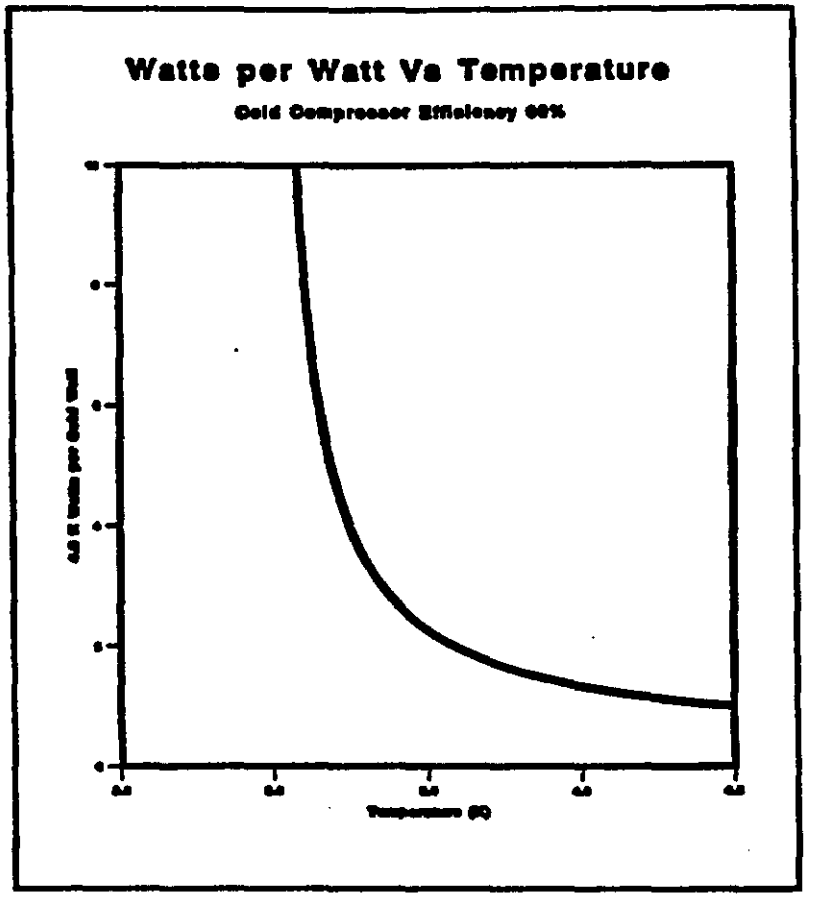

Figure 4.2: Satellite Performance 3.5 – 4.5K

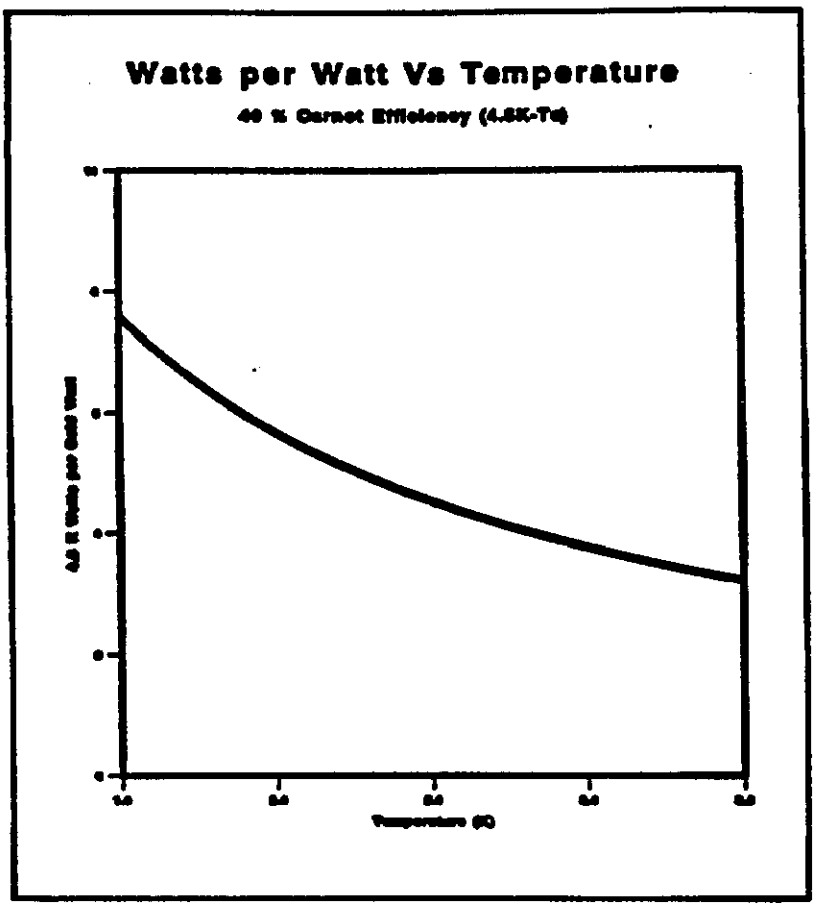

Figure 4.3: Satellite Performance 1.5 – 3.5K

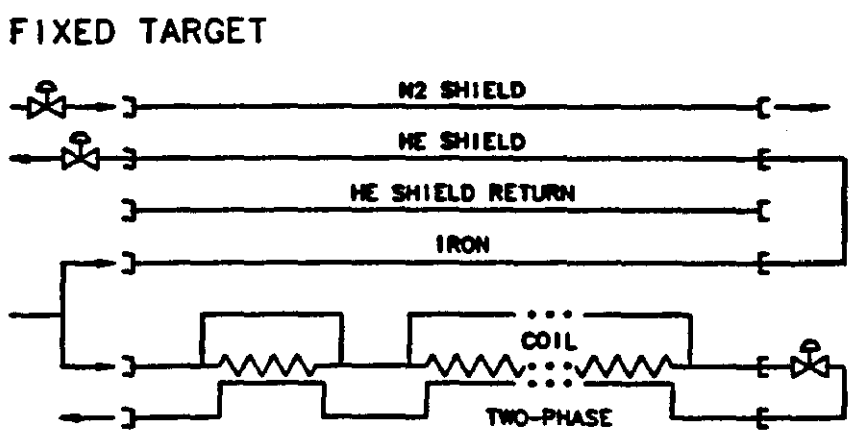

Figure 4.4: Fixed Target Mode Flow Schematic

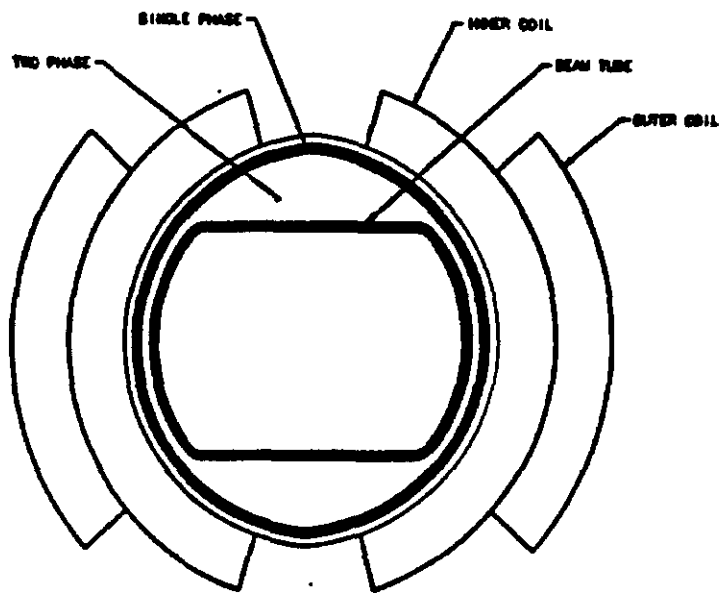

Figure 4.5: Two-Phase Passage Configuration

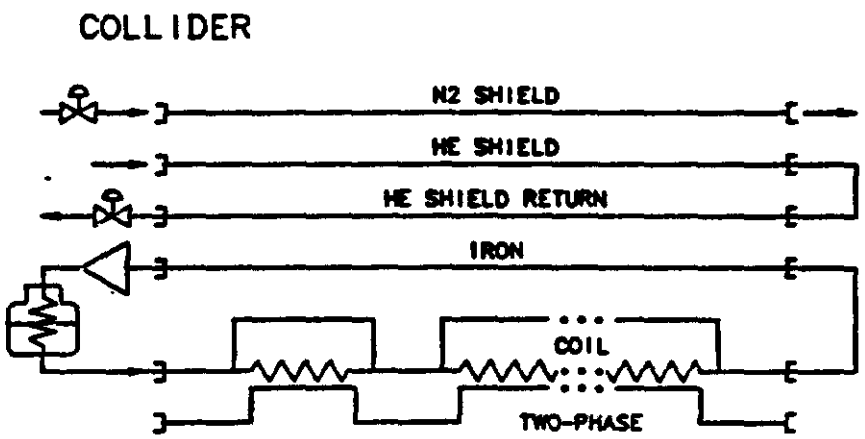

Figure 4.6: Collider Mode Flow Schematic

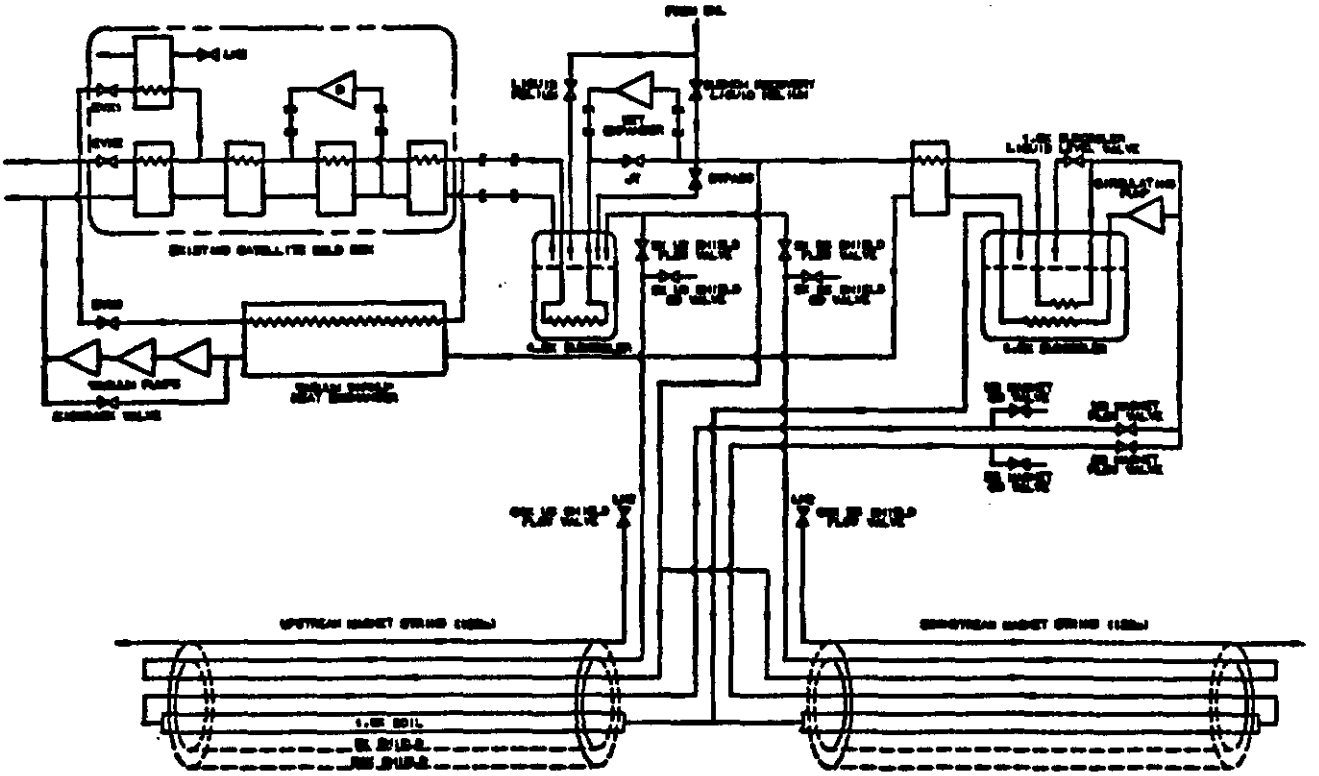

Figure 4.7: Satellite Refrigerator Configuration for 1.8K Accelerator Option

References

[1] T. Collins, Fermilab Internal Report, TN-1406.

[2] R. Flora, J. Saarivirta, G. Tool and D. Voy, *IEEE Trans. Nuc. Science*, NS–28, 3289, (1981).

[3] Hanft et al., *IEEE Trans. Nuc. Science*, NS–30, No. 4, 3381.

[4] K. Halbach, *Nuc. Inst. & Methods*, vol. 78, pp 185–198, 1970.

[5] A. Ishibashi, Industrial Symposium on the SSC, New Orleans, Feb. 1989.

[6] A. McInturff, private communication.

[7] A. McInturff et al., "The Fermilab Collider D0 Low β System", presented at European Particle Accel. Conf., Rome, Italy, June 7-11, 1988.

[8] G. Morgan, *IEEE Trans. Nuc. Science*, NS–32, no. 5, October 1985.

[9] A. I. Markushevich, Theory of Functions of a Complex Variable, Prentice-Hall, 1965.

[10] T. H. Nicol et al, A suspension system for superconducting super collider magnets, *Proceedings of the 11th International Cryogenic Engineering Conference,* Butterworths, Surrey, UK (1986).

[11] T. H. Nichol et al, SSC magnet cryostat suspension system design, *Advances in Cryogenic Engineering*, Vol. 33, Plenum Press, N.Y. (1988).

[12] R. J. Roark and W. C. Young, Formulas for Stress and Stain, 5th Edition, McGraw Hill, p. 428, N.Y. (1975).

[13] Fermilab Internal Report, to be published.

[14] M. Takeno et al, Thermal and mechanical properties of advanced composite materials at low temperatures, *Advances in Cryogenic Engineering*, Vol. 32, Plenum Press, N.Y. (1986).

[15] A. V. Tollestrup, Fermilab internal publication, UPC 86.

[16] A. V. Tollestrup, "Physics of High Energy Particle Accelerators", AIP Conf. Proc., No. 87, pp 800.